

AD-A213 433

**SUBMERGED ARC WELDING
CONSUMABLES
FOR
HSLA-100 STEEL**

by
DANIEL JOSEPH PETERS

B. S., MECHANICAL ENGINEERING, UNIVERSITY OF IDAHO (1980)

SUBMITTED TO THE DEPARTMENTS OF
MATERIALS SCIENCE AND ENGINEERING
AND OCEAN ENGINEERING IN PARTIAL
FULFILLMENT OF THE REQUIREMENTS FOR THE DEGREES OF

**NAVAL ENGINEER
and
MASTER OF SCIENCE in MATERIALS ENGINEERING
at the
MASSACHUSETTS INSTITUTE OF TECHNOLOGY**

June 1989

©Daniel Joseph Peters, 1989

The author hereby grants to MIT and to the United States Government permission to reproduce and distribute copies of this thesis document in whole or in part.

Signature of Author *Daniel J. Peters*
Department of Materials Science and Engineering
May 12, 1989

Certified By *Thomas W. Eagar*
Professor Thomas W. Eagar
Leaders for Manufacturing Professor of Materials Science
Department of Materials Science and Engineering

Certified By *B. Tibbitts*
Professor Barrick F. Tibbitts
Professor of Naval Construction and Engineering
Department of Ocean Engineering

Accepted By *Samuel M. Allen*
Professor Samuel M. Allen
Chairman, Department Graduate Committee
Department of Materials Science and Engineering

Accepted By *A. Douglas Carmichael*
Professor A. Douglas Carmichael
Chairman, Department Graduate Committee
Department of Ocean Engineering

DISTRIBUTION STATEMENT A

Approved for public release
Distribution Unlimited

89 10 10 144

DTIC
ELECTE
OCT 12 1989
S DCS D

SUBMERGED ARC WELDING CONSUMABLES FOR HSLA-100 STEEL

by

Daniel J. Peters

Submitted to the Departments of Materials Science and Engineering and Ocean Engineering on May 12, 1989 in partial fulfillment of the requirements for the degrees of Naval Engineer and Master of Science in Materials Engineering.

ABSTRACT

The development of a new class of high strength, low alloy steel with strength levels of 690 MPa (100 ksi) has made it necessary to formulate new welding consumables to take advantage of the potential benefits of this steel, HSLA-100. The possible benefits include welding without pre or post heating resulting in improved productivity. Optimizing the consumables for higher heat inputs will further improve productivity and reduce construction costs when using this steel.

This study investigates the effects of various levels of manganese and titanium (1.07 to 1.86 wt% and 0.012 to 0.025 wt%, respectively) in the weld metal when joining 13 mm (0.5 in) HSLA-100 plate using submerged arc welding methods. The alloying was accomplished by doping Oerlikon OP121TT flux with manganese and titanium oxides. 2.4 mm (3/32 in) Linde 120S wire was used in a series of six welds. The microstructure was characterized by optical and scanning electron microscopy, Auger electron spectroscopy, and quantitative metallography. Mechanical properties were quantified using all weld metal tensile tests and Charpy V-notch tests.

The optimum titanium content for the welds in this investigation was 0.012 wt%, the lowest level in this study. The range over which the titanium content varied was found to have little direct effect on the acicular ferrite fraction in the weld metal. The results indicated that the number of metallic oxide inclusions per unit volume and the inclusion size distribution were controlled by titanium bearing, faceted particles found within the spherical inclusions. Manganese also had little effect on the acicular ferrite fraction, but influenced the formation of martensite and retained austenite islands within the microstructure.

The martensite and retained austenite islands were clearly resolved via electrolytic etching and scanning electron microscopy. The fraction of this phase varied from 3.1% to 6.0% and was found to have a strong correlation with impact performance at low test temperatures. The fraction of martensite and retained austenite should be minimized in HSLA-100 weldments for optimum impact performance.

Thesis Supervisor:	Thomas W. Eagar
Title:	Leaders for Manufacturing Professor of Materials Engineering

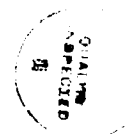
Table of Contents

Title Page	1
Abstract	2
List of Figures	5
List of Tables	7
Acknowledgements	8
CHAPTER 1	
<i>Introduction and Background</i>	9
1.1 Introduction	9
1.2 High-Strength Low-Alloy Steels	12
1.3 Weld Metal Alloying	14
1.3.1 Carbon	15
1.3.2 Manganese	21
1.3.3 Titanium	22
1.3.4 Oxygen	23
1.4 Inclusions	26
1.5 Flux	29
1.6 Summary	32
CHAPTER 2	
<i>Experimental Procedure</i>	34
2.1 Purpose and Scope	34
2.2 Experimental Procedure	35
2.2.1 Flux Preparation	35
2.2.2 Plate Preparation	38
2.2.3 Welding Procedure	40
2.3 Testing and Metallographic Examination	41
2.3.1 Chemical Analysis	43
2.3.2 Microhardness Testing	45
2.3.3 Optical Microscopy	45
2.3.4 Scanning Electron Microscopy	48
2.3.5 Tensile and Charpy Testing	50
2.4 Summary	51
CHAPTER 3	
<i>Results and Discussion</i>	52
3.1 Data Summary	52
3.2 Weld Metal Microstructures	56
3.2.1 Titanium Effects	61
3.2.2 Manganese Effects	73
3.2.3 Martensite and Retained Austenite	73
3.2.4 Other Effects	84
3.3 Mechanical Properties	88

CHAPTER 4

<i>Conclusions and Future Work</i>	99
4.1 Conclusions	99
4.2 Future Work	100
REFERENCES	101
APPENDIX A Confidence Limits for Chemical Testing	106
APPENDIX B Etchant Summary	107
APPENDIX C Diffusion Distances of C, Mn, and Si	108
APPENDIX D Charpy Curves	110

Accession For	
NTIS CRA&I	<input checked="" type="checkbox"/>
DTIC TAB	<input type="checkbox"/>
Unannounced	<input type="checkbox"/>
Justification	
By <i>per form 50</i>	
Distribution	
Availability Codes	
Dist	Avail and/or Special
A-1	



List of Figures

Schematic of the SAW process	11
HSLA-100 chemical composition and mechanical properties	13
Maximum hardness versus cracking parameter	17
Effect of Mn + Si content on volume fraction of M-A	19
Effect of M-A on FATT	19
Continuous cooling transformation diagram schematic	20
Effect of basicity index on weld metal oxygen content	25
Schematic of nucleation model	28
Required flux MnO content for given weld metal content	32
Weld metal compositional matrix	36
Weld joint geometry	39
Sketch of SAW equipment	40
Test plate sectioning for examination	42
Charpy specimen orientation	43
Sectioning for metallography specimens	44
Microscopy reference location	46
Macrophotograph of a representative weldment	56
Weldment A weld metal microstructure, 2% nital	58
Weldment B weld metal microstructure, 2% nital	58
Weldment C weld metal microstructure, 2% nital	59
Weldment D weld metal microstructure, 2% nital	59
Weldment E weld metal microstructure, 2% nital	60
Weldment F weld metal microstructure, 2% nital	60
Ti content versus acicular ferrite fraction	62
Ti content versus mean inclusion size	63
Ti content versus weld metal inclusion volume	64
Ti content versus number of weld metal inclusions	65
Example of faceted inclusion particle	67
Example of faceted inclusion particle	67
Inclusion particle Auger spectrum after one minute of ion sputtering	70
Inclusion particle Auger spectrum after five minutes of ion sputtering	71
Manganese versus weld metal acicular ferrite	72
Weld A weld metal M-A constituent, 2000X	74
Weld B weld metal M-A constituent, 2000X	74

Weld C weld metal M-A constituent, 2000X	75
Weld D weld metal M-A constituent, 2000X	75
Weld E weld metal M-A constituent, 2000X	76
Weld F weld metal M-A constituent, 2000X	76
Weld A weld metal M-A constituent, 5000X	77
Weld B weld metal M-A constituent, 5000X	77
Weld C weld metal M-A constituent, 5000X	78
Weld D weld metal M-A constituent, 5000X	78
Weld E weld metal M-A constituent, 5000X	79
Weld F weld metal M-A constituent, 5000X	79
Weld F weld metal M-A constituent, 10,000X	80
Weld A weld metal M-A constituent, 10,000X	80
Weld A weld metal M-A constituent, 25,000X	81
Weld F weld metal M-A constituent, 25,000X	81
P _{cm} versus M-A volume fraction	85
Boron content versus acicular ferrite fraction	86
Phosphorus content versus acicular ferrite fraction	87
M-A fraction versus transition temperature based on 50% shear	92
M-A fraction versus Charpy energy at 0 °F	93
M-A fraction versus Charpy energy at -60 °F	94
Charpy fracture surface	95
Charpy specimen sub crack around M-A particle	95
Charpy specimen M-A crack intitation site	96
Charpy specimen M-A crack intitation site	96
Temperature versus Charpy energy for weld A	111
Temperature versus Charpy energy for weld B	112
Temperature versus Charpy energy for weld C	113
Temperature versus Charpy energy for weld D	114
Temperature versus Charpy energy for weld E	115
Temperature versus Charpy energy for weld F	116
Temperature versus Charpy %shear for weld A	117
Temperature versus Charpy %shear for weld B	118
Temperature versus Charpy %shear for weld C	119
Temperature versus Charpy %shear for weld D	120
Temperature versus Charpy %shear for weld E	121
Temperature versus Charpy %shear for weld F	122

List of Tables

Oerlikon OP121TT flux composition	37
Proposed flux system MnO and TiO ₂ contents	37
HSLA-100 plate alloy content	38
Classification of microstructures in low C-low alloy steel	47
Weld metal alloy summary	53
Flux composition summary	54
Summary of quantative metallography data	55
Inclusion particle Auger element analysis	68
Inclusion SEM X-ray element analysis	69
Diffusivity of C, Mn, and Si	83
Chemical check analysis for boron and phosphorus	88
Mechanical property data summary	89
Mechanical property data summary continued	90

Acknowledgements

I must first thank Professor T. W. Eagar for his guidance and patience as thesis supervisor during my graduate studies at Massachusetts Institute of Technology. His friendship and encouragement have made three years at MIT much more than just a graduate education.

The support and friendship of the graduate students in the Joining group made the years at MIT memorable ones. I am especially thankful to Dr. Y. S. Kim, E. Kim, and R. Kapoor for answering my many questions.

I would like to acknowledge the U.S. Navy which sponsored my education at MIT and the research support from the Office of Naval Research, United States Department of the Navy (contract number N00014-88-K-0215).

David Taylor Research Center, U.S. Navy, provided the materials and conducted the mechanical properties testing for this research and I want to thank Mr. P. Holsberg, Mr. G. Franke, and Dr. T. Scoonover for their help and encouragement.

Finally, I want to express my deepest gratitude to my parents, who encouraged me as a youth, gave me room to grow, and made it possible for me to be where I am today.

CHAPTER 1

Introduction and Background

In chapter one a brief history of the development of submerged arc welding will be presented, followed by a discussion of the literature dealing with submerged arc consumables. This discussion will cover alloying, weld metal inclusions, and fluxes. Finally the scope of this thesis research will be described.

1.1 Introduction

Fusion welding as we know it today had its beginning at the end of the nineteenth century when heat sources of sufficient intensity became available on an industrial scale. These fusion techniques, which include gas welding, arc welding, and resistance welding, all came into existence at about the same time. By the turn of the century [1] oxyacetylene welding was a fully developed joining process for thin steel sections. Arc welding, by comparison, is more complex in character and developed more slowly. The best method of shielding the arc and how this shielding should be applied was a continuing problem.

In 1892 C. L. Coffin of Detroit [1] was awarded the first patent for an arc welding process using a metal electrode. This was the first recorded case of the metal melted from the electrode being carried across the arc to deposit filler metal in a joint.

Arc welding continued to develop as a joining process, although it was not until World War I that arc welding was used other than for repair and maintenance work [1]. The war brought a tremendous demand for production of metal products and arc welding was pressed into service. From that time to the present, welding

technology has enabled the economical construction of a wide range of products including pressure vessels, ships, bridges, and cars. Of the welding processes presently available, arc welding provides an excellent balance between speed and economy of manufacture. By comparison, oxyacetylene welding is extremely slow and limited to relatively thin sections. On the other hand, laser and electron beam welding which are rapid joining processes tend to be expensive and are limited in application due to the scope of the required equipment.

As the arc welding process progressed, improvements in shielding, electrodes, and technique have permitted the welding of increasingly higher strength steels. The quality of these welds in high strength steels may be characterized in many ways. One important measure is the fracture toughness of the deposited metal. The toughness of the weld metal becomes more important in high strength steels due to a lower tolerance for flaws.

A weld would be ideal if it were possible to exactly match the properties of the weld metal with those of the base metal. However, the welds in any large structure are essentially miniature castings in which it is impossible to duplicate the thermal and mechanical processing given to the base plate. With this restriction, the primary variables to improve the weld metal properties are the alloy content and the thermal cycle experienced during the welding process.

The high strength steel used in this study was developed for the U.S. Navy. It is therefore useful to undertake a broad examination of welding for construction of ships. Naval ship construction costs (hull, mechanical, and electrical) have increased in recent years with welding being the greatest cost driver involving the largest expenditure of manhours in a shipyard. As much as 20% of the expense of erecting a Naval ship may involve structural costs including that of materials and fabrication, and this fraction is even higher in commercial ship construction. The cost of materials may be \$0.50 to \$1.00 per pound with fabrication costs on the order

of \$4.00 per pound of structure. A graphic example of the man-hour investment is provided by considering that the welding department in a shipyard employs nearly twice the labor of any other trade.

These labor costs include preheating, weld repair, non-destructive testing, and post weld soaking. The costs for pre and post heating estimated to be on the order of \$0.50 per pound of structure only add to the costs of production. Ships are fabricated out of high strength steels which are joined by shielded metal arc, gas metal arc, and submerged arc welding.

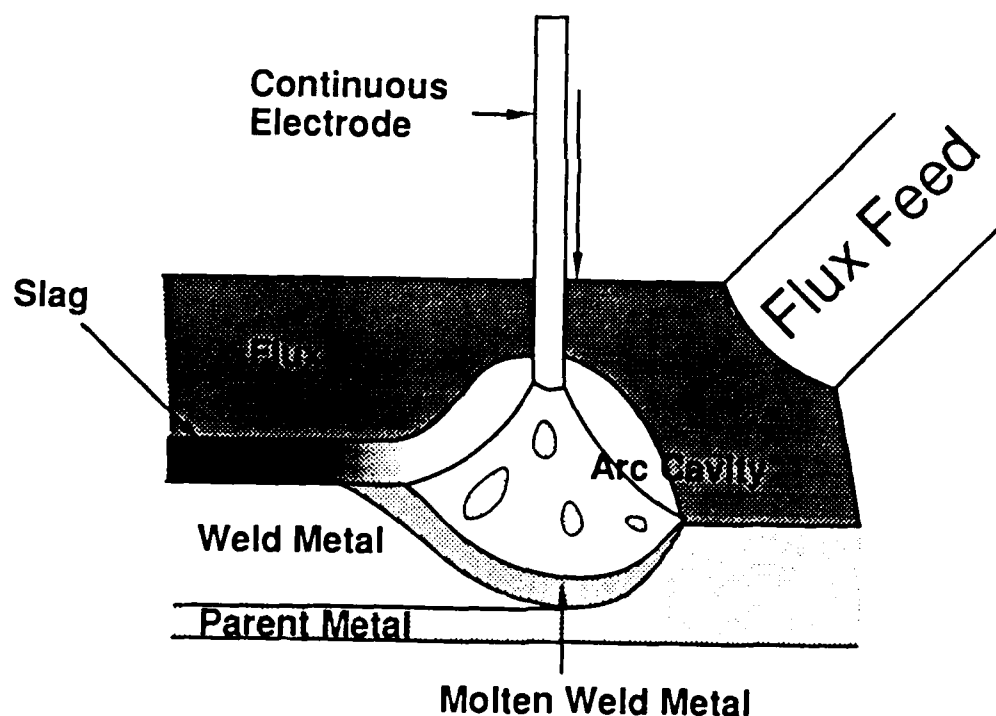


Figure 1. Schematic of the SAW process.

Of the above arc welding processes, submerged arc welding (SAW) is a very cost effective process with a deposition rate four to ten times as great as shielded metal arc welding when using high heat inputs. SAW is also favored in the shipyards since it produces no visible arc and few fumes so there is no interference with workers in the immediate vicinity. Extremely high currents (200 - 4000 A) can be used without spatter since the arc is completely shielded. Operator skill requirements are the lowest of the above mentioned joining processes since travel speed and wire feed rate are controlled by the welding machine.

Figure 1 is a schematic of the SAW process showing the application of the flux bed ahead of the arc cavity.

This joining process was developed independently in the U.S. and U.S.S.R. in the middle and late 1930's [2] and has remained an important welding process because of the previously mentioned advantages.

1.2 High-Strength Low-Alloy Steels

A wide variety of steels have been used in ship construction. The use of ever higher strength steels has required more stringent quality control which has greatly increased costs. The high-strength, low-alloy (HSLA) steels hold promise of being economical due to reduced fabrication costs. These steels are typically low carbon-manganese steels with small amounts of alloys added such as aluminum, titanium, niobium, or vanadium. Since these steels exhibit high strength and toughness, they are ideally suited for Naval shipbuilding.

In 1982 the U.S. Navy, through the Naval Sea Systems Command, instituted the Material Fabrication Improvement goals for 1983 to 1990. The prime goal was to "reduce shipbuilding costs through improvement of welding processes, materials, technologies, procedures, and techniques, while simultaneously improving overall quality." Research and development of an HSLA-100 system grew out of this effort to improve shipbuilding materials and joining techniques.

HSLA-100 is a precipitation hardened steel which does not exhibit the cracking problems associated with high carbon, high alloy steels. HSLA-100 steel utilizes copper for strength with nickel added to improve toughness. Since the steel is low in carbon, which improves the weldability, welds may be made without pre and post heating, thus improving the economy of manufacture.

Chemical Composition (wt%)
(maximum unless range indicated)

Carbon	0.06
Manganese	0.75 - 1.05
Phosphorus	0.015
Sulfur	0.006
Silicon	0.40
Nickel	3.35 - 3.65
Chromium	0.45 - 0.75
Molybdenum	0.55 - 0.66
Copper	1.45 - 1.75
Columbium	0.02 - 0.06
Aluminum	0.020 - 0.040
Nitrogen	0.015

Mechanical Properties

Yield Strength, 0.2% offset	690 - 827 MPa (100 - 120 ksi)
% Elongation	17%
Notch Toughness	38 J @ -18 ± 1.7 °C (28 ft-lb @ 0 ± 3 °F)
	20 J @ -84 ± 1.7 °C (15 ft-lb @ -120 ± 3 °F)

Table 1. HSLA-100 chemical composition and mechanical properties.

This steel was developed for the U.S. Navy through David Taylor Research Center. Table 1 shows the chemical composition and minimum mechanical properties of the steel in 12 mm (0.5 in) sections.

Initially, joining of HSLA-100 used a SAW flux and electrode system developed for HY-100 steels. This did not provide adequate mechanical properties in all cases, making it necessary to investigate new flux/electrode compositions. This investigation was directed toward the study of new flux compositions intended for applications without the use of preheat.

1.3 Weld Metal Alloying

The microstructure and properties of the weld metal are controlled by the chemical composition and the thermal cycle imposed during welding. Since high deposition rates in SAW require high heat input, the thermal cycle experienced by the deposit cannot be controlled with wide latitude. Hence only chemical composition is available as a means of controlling the transformation characteristics, the microstructure, and the toughness of the weld metal.

Studies of weld metal microstructure have found that acicular ferrite is the primary phase associated with high toughness [3]. This transformation product forms intragranularly resulting in randomly oriented, short ferrite needles with high angle grain boundaries, and exhibits a basket weave morphology. The fine grain size and interlocking laths of acicular ferrite provide maximum resistance to cleavage fracture, thus improving notch toughness. For this reason it is desirable to maximize the volume fraction of acicular ferrite in the weld metal by controlling prior austenite grain size and the transformation products. This is done by adjusting alloy content and oxygen content in the weld metal.

Prior investigations [4,5] have shown that during the transformation of austenite to ferrite, the ferrite first forms along austenite grain boundaries and thickens in a direction perpendicular to the plane of the austenite boundary. This grain boundary phase is called an allotriomorph. Depending on the composition and the cooling

rate, ferrite with an aligned phase may develop from these allotriomorphs. Such grain boundary phases are detrimental to weld metal toughness. In the interior of the austenite grain, transformation occurs via nucleation of fine ferrite "needles" called acicular ferrite. It has been shown by Liu *et al.* [6] that acicular ferrite nucleates on oxide inclusions which are present in the weld metal. The acicular ferrite generally increases toughness. Hence modifications in composition are usually directed toward decreasing the grain boundary allotriomorphs and increasing the acicular ferrite phase.

Since it is desirable to maximize the volume of acicular ferrite, any alloying elements which either suppress the formation of grain boundary ferrite or which promote the nucleation of acicular ferrite are beneficial.

During welding, chemical composition of the weld metal is determined by the alloy content of the welding electrode, the flux, and dilution from the base metal. Although many elements may be considered, several have been shown to have a profound effect on mechanical properties, notch toughness, and the weldability of HSLA-100 steel. Let us briefly consider some of the more important ones.

1.3.1 Carbon

Carbon is the most important alloying element when considering the weldability of steel. In fact weldability is often expressed in terms of a carbon equivalent (C_{eq}) which is generally specified to be below a maximum value. As a general rule a steel is considered weldable if C_{eq} is < 0.4 [7]. This value is based on the relative influence of the alloying elements on the transformation behavior of the steel, more specifically on the hardenability of the steel. One form of the carbon equivalent relation which has been adopted by the International Institute of Welding is

$$C_{eq} = \%C + \frac{\%Mn}{6} + \frac{\%Cr + \%Mo + \%V}{5} + \frac{\%Cu + \%Ni}{15} \quad (1)$$

where all amounts are in wt%.

At present there are a number of carbon equivalent formulas which have been developed for particular steels. It has been found [7] that evaluation of the cold cracking susceptibility of low carbon steels with less than 0.18% carbon is best done with the Ito-Bessyo P_{cm} (cracking parameter) as compared with the older C_{eq} shown in equation (1). The C_{eq} relation was developed primarily with steels whose carbon content is greater than 0.18%.

The P_{cm} is determined by

$$P_{cm} = \%C + \frac{\%Si}{30} + \frac{\%Mn + \%Cu + \%Cr}{20} + \frac{\%Ni}{60} + \frac{\%Mo}{15} + \frac{\%V}{10} + 5\%B \quad (2)$$

where the elements are in wt% as before. Here the steel is considered weldable if the P_{cm} is less than 0.30 [8].

Figure 2 shows the relation between P_{cm} and H_{max} (maximum hardness) for steels with 0.09 to 0.17% carbon. Since the value of H_{max} will depend not only on the alloy composition, but also on the cooling rate, it was necessary to estimate the effective cooling rate for a SAW weld. Specifically, a weld with a heat input of 2.2 kJ/mm on 25 mm (1 in) thick steel plate was used as an example. Using data from Deb *et al.*, a cooling time of 30 seconds from 800 °C to 500 °C was used which corresponds to a cooling rate of 11 °C/sec.

From equations (1) and (2) it is clear that the amount of carbon present in the weld metal will have a strong effect on the weldability and on the final microstructure. A reduction in weldability is shown by an increase in susceptibility to cold cracking which is of concern in high strength steel structures.

When the carbon content is kept to the lowest possible level there will be less carbon rejected to the residual austenite by the ferrite. This residual austenite later transforms to a martensite - austenite (M-A) constituent which is known to have poor toughness [10]. Since carbon is known to promote the formation of M-A, low carbon levels are desirable.

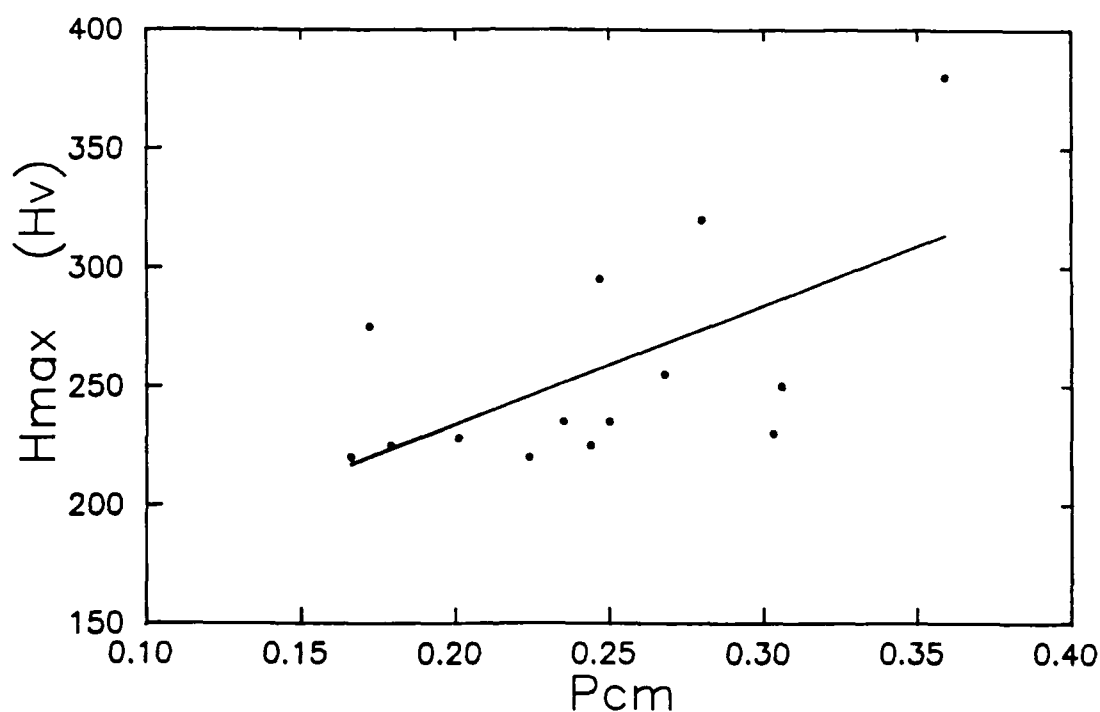


Figure 2. Maximum hardness versus P_{cm} based on cooling from 800 °C to 500 °C in 30 seconds [7].

The process of M-A formation can be described in the following manner. As the weld metal cools from the austenite state, the austenite (γ) to ferrite (α) ($\gamma \rightarrow \alpha$) transformation begins. During this transformation, carbon is rejected from the ferrite while the remaining austenite becomes stable because of further carbon enrichment. At this point the carbon content of the austenite may be 0.6 - 0.7 wt% at 350 - 400 °C [11]. As cooling continues, some of the carbon enriched austenite will decompose to martensite with the remaining austenite present in the microstructure as retained austenite. This M-A constituent then exists as islands within the weld metal microstructure [11]. The temperatures at which the previously described reactions occur will vary depending on the alloy content of the weld metal and the cooling rate.

Coldren *et al.* [12] conducted a study of the M-A constituent on X-70 linepipe steel. The data from the study shows that the amount of M-A present depends on the manganese and silicon in the weld metal. As the wt% Mn + wt% Si exceeded 1.90, the M-A volume fraction increased significantly as shown in figure 3. Coldren *et al.* also showed a strong increase in the fracture appearance transition temperature (FATT) from Charpy specimen testing as the M-A volume fraction increased which is shown in figure 4.

As an aside, the formation of bainitic and martensitic structures occurs at temperatures lower than the transformation temperatures for primary ferrite or acicular ferrite. This can be seen in figure 5 which is a schematic of a continuous cooling transformation diagram for a microalloyed HSLA steel. Here the effect of different cooling rates on the final microstructure can be seen. Addition of elements to the weld metal will generally move this curve to the right. For example, manganese will tend to move the curve to the right. The only two elements which will shift the curve to the left are cobalt and silicon.

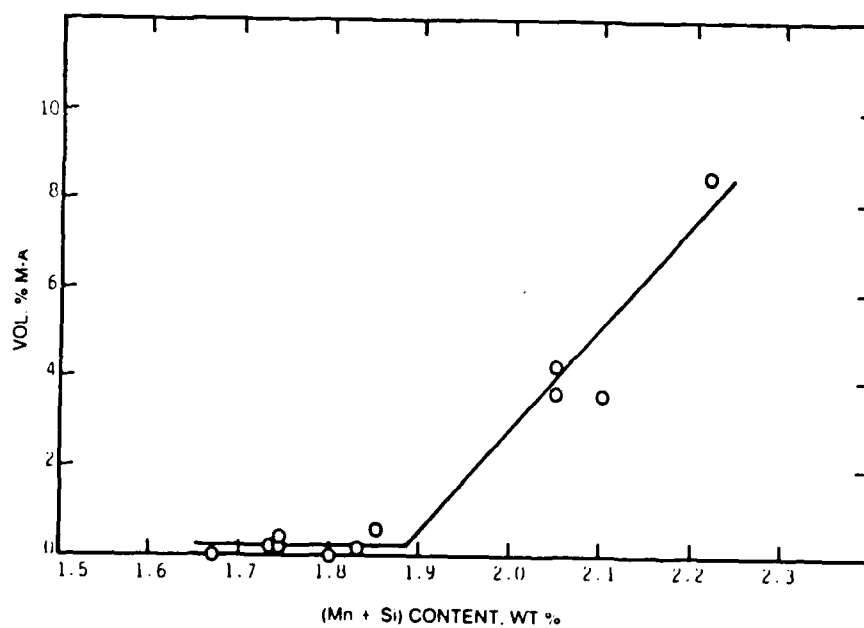


Figure 3. Effect of Mn + Si content on volume fraction of M-A [12].

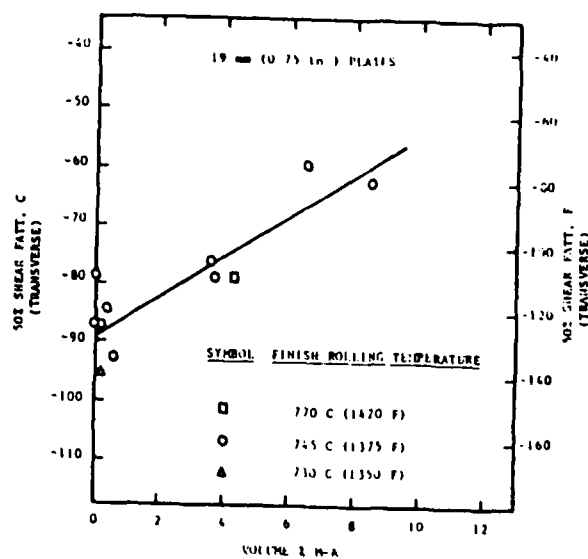


Figure 4. Effect of M-A on FATT [12].

Lowering the amount of M-A constituent in the weld metal may improve mechanical properties, including toughness in high strength steels. This is because the M-A constituent is high in carbon, has been rapidly cooled and is very brittle. Carbon contents in the M-A may be on the order of 0.8 wt%.

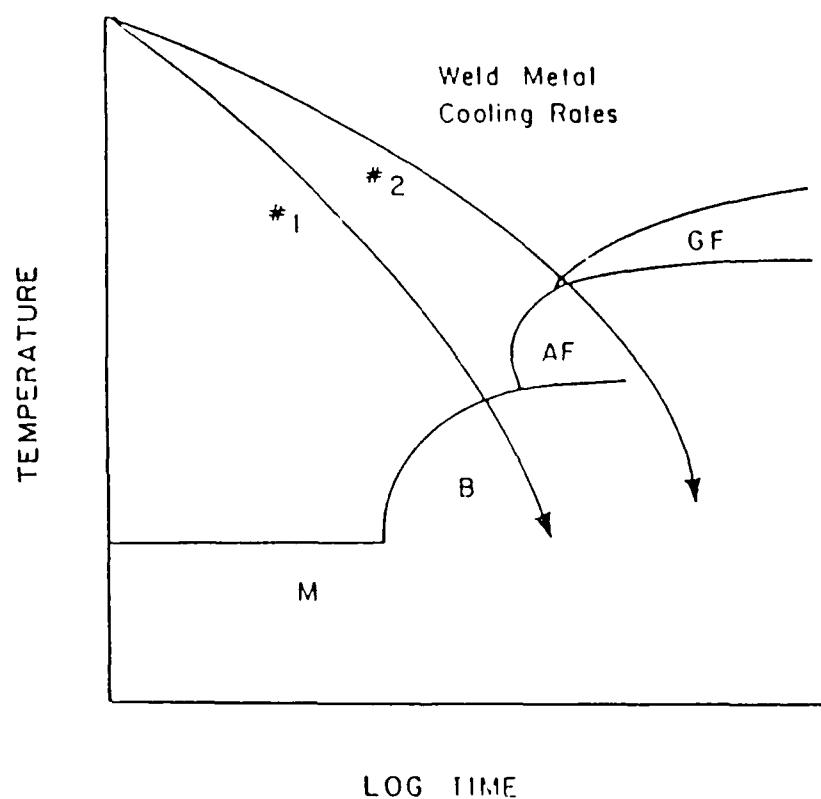


Figure 5. Continuous cooling transformation diagram schematic.

Considering the previous discussion, any attempt to improve the weld metal toughness should begin by reducing the carbon content and thereby the M-A fraction. This will be realized by using base metals and electrodes which are

low in carbon. However, without carbon to serve as a hardener, other alloying additions will be needed in the weld metal. One such element is manganese which is recognized as a hardener in steel systems.

1.3.2 Manganese

Manganese improves the hardenability of the weld metal by shifting the austenite decomposition transformation to longer times, i.e. moving the continuous cooling transformation curve in figure 5 to the right. For a given set of welding parameters (fixed heat input) the microstructure can be controlled by alloying with manganese. This addition of manganese increases the proportion of acicular ferrite at the expense of primary ferrite, and also assists in refining the secondary microstructure.

Manganese is also a significant hardener, not as potent as carbon, but without the detrimental segregation effects associated with carbon in high strength steel. Since manganese does not segregate during the cooling transformation, it improves the hardness of all phases present, including the weaker primary ferrites.

Typical manganese levels may vary from 1.0 to 2.0 wt% with improved properties being noted at the higher level [13]. Selecting an optimum bulk manganese content in the weld metal matrix must include consideration of the amount of manganese in the manganese silicate inclusions. An example is that when the inclusions are manganese silicates, one-eighth of the weld metal manganese is in the inclusions at 1000 ppm oxygen [14]. So when comparing welds with the same bulk manganese level, it cannot be assumed that the effect of the manganese on hardenability and transformation products will be the same unless the welds contain similar levels of inclusions.

As discussed in section 1.3.1, manganese, when present in large amounts may have the effect of increasing the volume fraction of the M-A constituent. For this reason a balance between the advantages and disadvantages of manganese must be found.

In summary, the manganese present in the weld metal refines the grain size, increases hardenability, and promotes the formation of acicular ferrite, by displacing the transformation temperature to lower values. A side effect may be the above mentioned increase in M-A constituent.

1.3.3 Titanium

Titanium has been shown to be an important element for improving weld metal toughness via several mechanisms. Titanium may combine with oxygen to form finely dispersed titanium oxide inclusions which have been shown to promote the intragranular nucleation of acicular ferrite [15]. This is due to a favorable crystallographic orientation between the titanium oxide inclusions and the nucleated acicular ferrite.

A second mechanism involves the formation of titanium nitrides. Nitrogen is present after welding in uncombined form unless there is titanium present, in which case titanium nitrides will form. Free nitrogen has the detrimental effect of increasing the transition temperature 2 - 4 °C per 0.001 wt% increase in nitrogen [16]. Excess titanium over that needed for titanium nitrides may result in the formation of detrimental titanium carbides. The ratio of titanium to nitrogen should be less than 3.5 by weight.

Originally it was thought that these nitrides were likely nucleation sites for acicular ferrite. A more recent explanation is that the titanium nitride precipitates tie up the free nitrogen, thus promoting boron segregation at the prior austenite grain boundaries [17,18]. The solute boron which segregates at the austenite grain boundaries suppresses the nucleation of primary ferrite and so promotes the formation of acicular ferrite.

Relatively small amounts of titanium and boron are necessary to maximize the formation of acicular ferrite in HSLA steels. Masumoto [19] determined optimal ranges of titanium and boron to be:

Ti → 0.01 - 0.05 wt% (< 0.03 wt% preferred)

B → 0.001 - 0.003 wt%

for maximum toughness in high strength steel weld metal.

1.3.4 Oxygen

Oxygen contamination is present in SAW weld metal due to the transfer from the fluxes used to protect and refine the weld metal. Since the oxygen levels in both base metal and electrodes is generally less than 100 ppm, the sources must be either the shielding flux used or the atmosphere. The major oxygen contribution is from the SAW flux and is due to dissociation of the weak oxides which are flux components. For example, fluxes based on FeO, MnO, and SiO₂ may contribute very high levels of oxygen to the weld metal. Since the solubility of oxygen in iron is very low, the majority of the oxygen present is in the form of oxides resulting from reactions of oxygen with alloying elements such as manganese, silicon, aluminum, and titanium.

During the welding process, the oxides grow and separate from the molten metal to the layer of molten slag. However, due to the rapid solidification which takes place during welding, some inclusions become trapped in the matrix. These second phase particles affect the phase transformation of the weld metal and so the physical properties.

To quantify the effect of flux composition on the weld metal Tuliani, *et al.* [20] proposed a popular basicity index (BI)

$$BI = \frac{\%CaO + \%CaF_2 + \%MgO + \%K_2O + \%Na_2O + 0.5(\%MnO + \%FeO)}{\%SiO_2 + 0.5(\%Al_2O_3 + \%TiO_2 + \%ZrO_2)} \quad (3)$$

where values are in wt%.

The use of basicity was first used in the steel making industry to characterize the refining capability of slags. The use of a BI in SAW is used to describe flux behavior in terms of oxygen transfer to the weld metal. Acidic fluxes are associated with high oxygen contents and high densities of large spherical inclusions. Basic fluxes are associated with lower oxygen contents and fewer inclusions. A neutral flux would have a BI of 1.0.

Eagar [21] has modified Tuliani's formula slightly by removing CaF_2 since CaF_2 is neutral in terms of reactions involving silicon, manganese, and oxygen. The BI then becomes

$$BI = \frac{\% \text{CaO} + \% \text{MgO} + \% \text{K}_2\text{O} + \% \text{Na}_2\text{O} + 0.5(\% \text{MnO} + \% \text{FeO})}{\% \text{SiO}_2 + 0.5(\% \text{Al}_2\text{O}_3 + \% \text{TiO}_2 + \% \text{ZrO}_2)} \quad (4)$$

Eagar found that available data fit both equations (3) and (4) equally well, however, he cites thermodynamic data which support the values obtained from equation (4). Figure 6 shows the basicity index versus weld metal oxygen content which was experimentally developed from a series of weld data. As the BI value increases, cleaner welds with respect to non-metallic oxide inclusions can be expected due to reduced oxygen content.

This increase in BI with decreasing oxygen content is shown in figure 6 based on equation (4).

Numerous papers have been published which show the effects of oxygen on toughness of the weld metal. Dallam *et al.* [22] reported that oxygen levels greater than 500 ppm, corresponding to a high concentration of non-metallic inclusions, had a negative effect on Charpy toughness and the ductile to brittle transition temperature. Dallam also reported that oxygen levels of 200 - 500 ppm produced tough acicular ferrite structures. Below levels of 200 ppm oxygen,

acicular ferrite nucleation is restricted because of insufficient nucleation sites. In this case, the ferrite associated with prior austenite grain boundaries (grain boundary allotriomorphs) is evident in the microstructure.

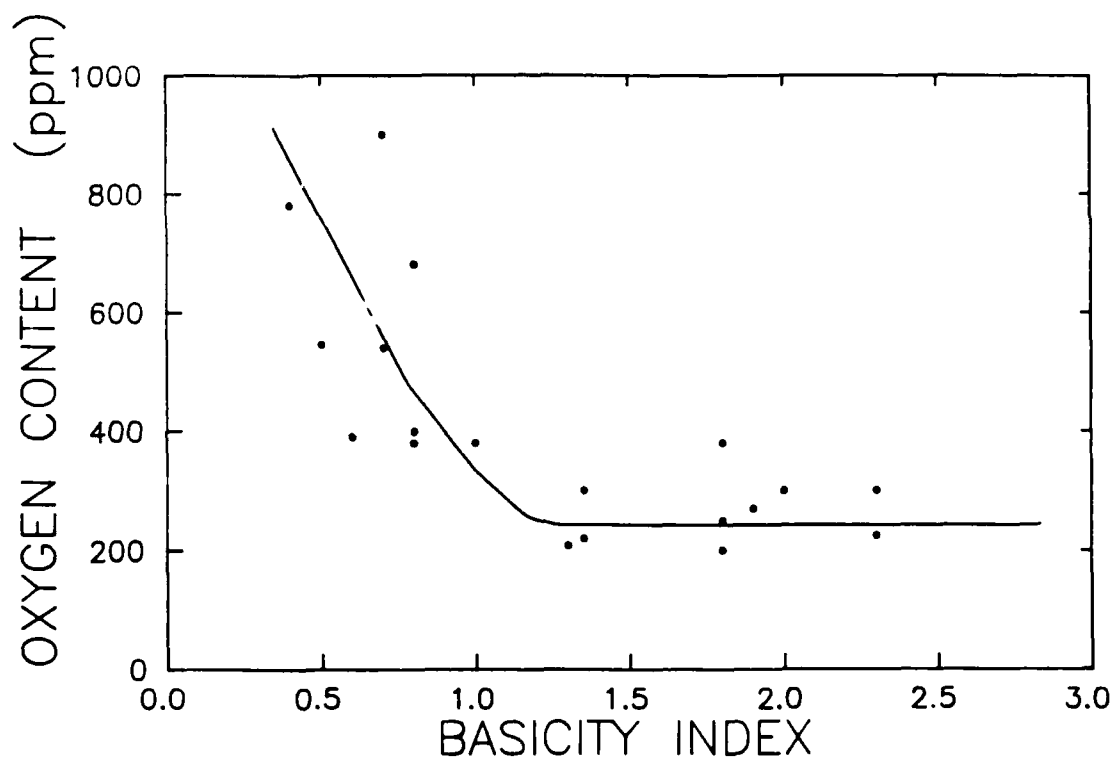


Figure 6. Effect of basicity index on weld metal oxygen content [21].

The desired oxygen concentration in a specific system may differ from the above values due to changes in other alloying element levels. But regardless of

the optimum level, it is the effect of oxygen on inclusion size and population that influences the microstructure, the Charpy energy, and the ductile to brittle transition.

1.4 Inclusions

The inclusions found in HSLA weldments are important in controlling the final microstructure so that the volume fraction of acicular ferrite is maximized. The acicular ferrite consists of fine grained ferrite which forms in austenite grains during the $\gamma \rightarrow \alpha$ transformation. These individual ferrite laths are separated by high angle grain boundaries which hinder cleavage crack growth during fracture. The nucleation of the acicular grains is thought to be strongly controlled by the inclusion population [22,23].

As the molten weld pool is cooled, the solubility of oxygen is decreased. At this point the oxygen begins to react with the deoxidants, forming complex glassy oxides which eventually become trapped in the steel. During the solidification process these oxide particles grow in size and many leave the molten weld pool, becoming part of the slag covering the weld bead. In this way the weld metal is refined. However, since the solidification process is extremely rapid in the weld pool, some of these oxides become trapped in the metal matrix as inclusions. Microanalysis of these inclusions generally reveals manganese, silicon, aluminum, and titanium [24].

The inclusions present in the weld metal affect the $\gamma \rightarrow \alpha$ transformation by providing nucleation sites for the ferrite either at the prior austenite grain boundaries or within the austenite grains. The transformation products will include acicular ferrite, side plate ferrite, polygonal ferrite, and grain boundary ferrite.

For nucleation to occur there must be a certain minimum energy available in order to accommodate the surface and strain energies of the nucleated phase. Ricks

et al. [25] analyzed the energies for the formation of a ferrite nucleus on a spherical inclusion in the following manner. The inclusion and ferrite nucleus are modeled as spheres in an austenite matrix. The increase in surface energy, ΔS , is

$$\Delta S = (A_S - A_{C1})\sigma_{\gamma/a} + A_{C2}(\sigma_{inc/a} - \sigma_{inc/\gamma}) \quad (7)$$

where

A_S = area of sphere of radius R

A_{C1} = area lost due to sectioning of nucleus

A_{C2} = area of inclusion/nucleus interface

$\sigma_{\gamma/a}$ = surface energy of austenite/ferrite interface

$\sigma_{inc/a}$ = surface energy of inclusion/ferrite interface

$\sigma_{inc/\gamma}$ = surface energy of inclusion/austenite interface

Ricks makes the simplifying assumption that $\sigma_{inc/\gamma} = \sigma_{inc/a}$ since the crystal structure of the inclusions is complex and the chance of a rational orientation relationship developing is small.

Substituting for $A_S - A_{C1}$

$$\Delta S = [4\pi R^2 - 2\pi R^2(1 - \cos\theta)]\sigma_{\gamma/a} \quad (8)$$

Figure 7 shows the model used by Ricks in the analysis and defines the terms in equation (8).

The total free energy change associated with nucleation on an inclusion, ΔG_T , is

$$\Delta G_T = V\Delta G_V + \Delta S \quad (9)$$

where ΔG_V is the free energy per unit volume associated with the formation of ferrite from austenite and V is the volume of the nucleus shape in figure 7.

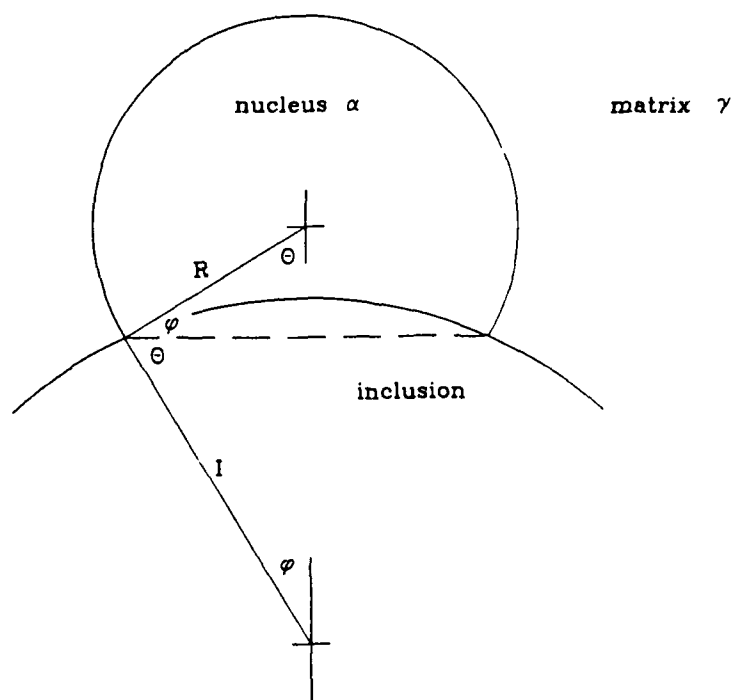


Figure 7. Schematic of nucleation model [25].

The nucleation barrier ΔG^* , may be calculated by differentiating equation (9) with respect to R , equating to zero to obtain the critical nucleus radius, R^* , and then substituting back into equation (9).

Ricks demonstrated that the energy barrier for nucleation of intragranular ferrite on inclusions is a function of inclusion size. He demonstrated that the energy barrier decreased as inclusion size increased up to about $1.0 \mu\text{m}$ with no correlation above $1.0 \mu\text{m}$.

Using this analysis, Easterling [26] proposed that unless the inclusions were of 0.25 - 0.50 μm in size, nucleation of acicular ferrite would not be favorable. This agrees well with experimental data presented by Jang *et al.* and Liu *et al.* [6,27] which suggested the ideal size for acicular ferrite nucleation to be 0.40 - 0.60 μm . Inclusions of smaller sizes are effective in pinning austenite grain boundaries, but not in nucleating acicular ferrite.

Cochrane *et al.* [28] have suggested that inclusions lodged in the austenite grain boundaries encourage ferrite nucleation. Primary ferrite (consisting of grain boundary and polygonal ferrite) forms first during cooling. Ferrite with aligned second phase (consisting of side plate ferrite and bainite) may grow from the primary ferrite. In terms of weld metal toughness, the transformation products associated with the grain boundaries are detrimental since they provide an easy propagation path during cleavage fracture. A second effect is the resulting reduction in volume available for acicular ferrite formation. The acicular ferrite is an intragranular transformation product which consists of individual ferrite laths within prior austenite grains. Garritte *et al.* [29] have provided metallographic evidence for nucleation of acicular ferrite on inclusions; however, insufficient inclusions were found to account for the nucleation of all the acicular ferrite. This may be explained by nucleation on sites other than inclusions, such as dislocations.

1.5 Flux

The flux used in the SAW process shields the molten weld pool from atmospheric contamination, provides arc stabilization, refines the weld metal by removing undesirable contaminants, and provides alloying elements to the weld metal. The flux bed, along with the slag covering, insulates the weld bead after the arc passes, thereby reducing the cooling rate in SAW.

There are four main types of SAW fluxes viz. fused, bonded, agglomerated, and pressed powder fluxes. For the purposes of this discussion, only the bonded type fluxes will be considered. These fluxes are comprised mainly of raw minerals

in granular form, each of which may contain several compounds. These minerals are ground to a predetermined size and then bonded with soluble alkali silicates such as sodium or potassium silicate. The resulting slurry is then mixed, followed by drying at a temperature less than 650 °C. As the silicate dries, a glassy network is formed which binds the raw minerals together. Finally, this mixture is crushed and ground to the required size for use.

The SAW bead shape is influenced by characteristics of the flux such as viscosity, interfacial tension, and arc stabilization. Viscosity must be such that gases generated in the weld pool can escape and also allow element transfer between the flux and the weld metal. As viscosity is increased, the weld bead is confined and heat transfer is concentrated in a narrower region. Rutile and alumina are examples of compounds used to control flux viscosity.

The influence of interfacial tensions of the slag on SAW is related to its effect on the heat flow within the base metal. If the flux-liquid interfacial tension is large, then the weld bead width is minimized and penetration is increased. On the other hand, if the flux-solid interfacial tension is large, then the molten bead width will be larger, reducing penetration.

The SAW arc is stabilized by the ionizable elements found in the flux. If these elements are easily ionized, then the arc is more stable. Arc stabilization is enhanced in the flux by calcium fluoride, rutile, and silica. Fluctuations in the arc voltage during welding results in varying heat input causing reduced penetration.

The slag-metal reactions during the SAW process determine the weld metal alloy content, along with the electrode and base plate compositions. Chai [30] developed a thermodynamic equilibrium model to predict the range of possible manganese and silicon contents in the weld metal for a given flux, electrode, and base metal chemistry. The model is based on the assumption that a neutral point or equilibrium condition exists at which metal transport between the slag and weld pool is zero. By using this concept of a neutral point, a flux composition can be chosen such that the resulting weld metal has a specific alloy composition.

To predict the manganese content of the weld metal, Chai analyzed the MnO slag reaction by first estimating the effective temperature of the weld pool to be 2000 °C. The resulting reaction is represented by the following analysis

$$\begin{aligned}
 \text{MnO}_{\text{liq}} &= [\% \text{Mn}] + [\% \text{O}] \\
 \log K &= -\frac{12760}{T} + 5.68 \\
 K &= \frac{[\% \text{MnO}][\% \text{O}]}{(MnO)}
 \end{aligned}
 \tag{10}$$

where (MnO) is defined as the activity of MnO.

Neglecting terms due to small interactions between manganese and oxygen in the base materials, Chai obtained an equation of the form

$$(MnO) = 0.86[\% \text{Mn}][\% \text{O}] \tag{11}$$

Assuming that weld metal oxygen content decreases with increasing flux basicity, equilibrium plots may be generated for various flux systems as shown in figure 8. From these plots the required flux system can be determined based on required weld metal composition.

Although Chai chose to examine only manganese and silicon, other elements such as titanium are candidates for alloying via the SAW flux system.

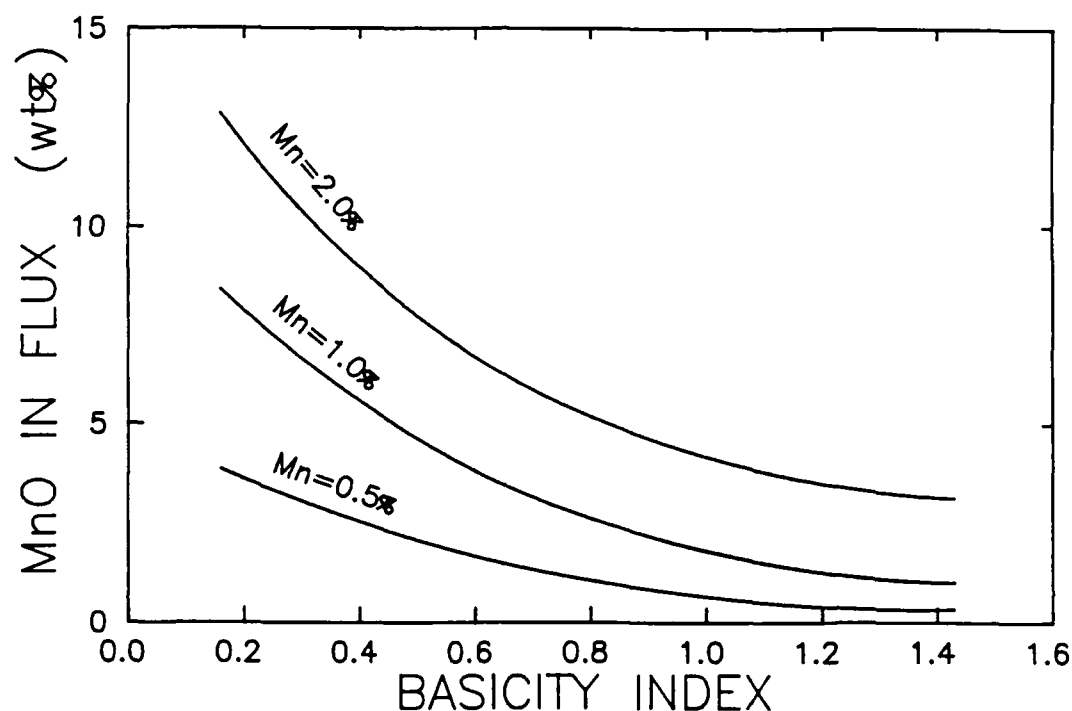


Figure 8. Required flux MnO content for given weld metal manganese content in a MnO-CaO-Al₂O₃ flux system [30].

1.6 Summary

HSLA-100 is a promising material for economical Naval ship construction. However, before certification for use, the joining processes and the filler metals must be qualified via extensive microstructural evaluation and mechanical testing. The variables in the SAW process are extensive; in this investigation only the effects of varying the weld metal manganese and titanium contents through the flux composition will be examined.

An attempt will be made to correlate the weld metal microstructural constituents with the mechanical properties in a series of welds in HSLA-100 steel. This will be done through chemical analysis of the weld metal, quantitative examination of the microstructure, and correlation of the observed microstructure with the fracture surface observed on broken Charpy V-notch specimens.

CHAPTER 2

Experimental Procedure

In chapter two the experimental procedure will be described, including plate and flux preparation, welding, and sectioning. Also included is a discussion of the metallography techniques used for data collection.

2.1 Purpose and Scope

The purpose of this investigation is to examine the effects of manganese and titanium on the microstructure and properties of HSLA-100 submerged arc weld metal. Specifically, systematic additions of manganese and titanium were made via flux composition adjustment. This provided data to describe the effects of manganese and titanium on the microstructure. These effects were then examined via quantitative metallography and mechanical properties.

Metallographic analysis utilized microhardness testing, optical microscopy, and scanning electron microscopy. Auger electron spectroscopy was used to analyze inclusion composition. The weld metal element content was also quantified.

Since the microstructure and properties of HSLA-100 weld metal depend on cooling rate and alloy content as discussed in chapter one, variations in either of these must be made to improve the weld metal properties. In this investigation the cooling rate was constant (heat input constant) with the only variable being the flux systems used.

2.2 Experimental Procedure

For the purpose of this investigation the parent metal, which was HSLA-100 and the electrode, Linde 120S wire 2.4 mm (3/32 in dia.), were fixed, whereas the flux composition was varied in MnO and TiO₂ content. As discussed in section 1.5, the variation in flux basicity will cause the neutral points of the alloying elements to change. For this reason it was necessary to formulate a matrix of different flux systems resulting in the desired weld metal chemistries. As the basicity index is varied due to changes in flux oxide content, the transfer of elements between the weld metal and slag will also change. This is an important consideration in this investigation since relatively large amounts (10 - 30 wt%) of TiO₂ were added to the flux system.

The target amounts of manganese and titanium in the weld metal were based on a review of previous experimental data. From these studies, levels of 1.2 to 1.8 wt% manganese and 0.01 to 0.03 wt% titanium were chosen as the most desirable ranges when considering weld metal toughness. Figure 9 is a schematic of the weld metal compositional matrix used in this investigation.

As will be discussed in section 3.1, the actual weld metal composition differed from these target values.

2.2.1 Flux Preparation

Flux preparation began by first selecting Oerlikon OP121TT SAW flux as the base to which manganese and titanium oxides would be added. Oerlikon OP121TT flux is a basic, bonded flux with a basicity index of 1.4¹. The flux composition is given in table 2.

¹ Calculated using Eggar's relation for the BI shown in equation (4).

Calculation of the needed amount of manganese oxide required in the flux to produce the required weld metal manganese content shown in figure 9 began by referring to Chai's equilibrium diagrams [30]. From these models it was estimated that 2.0 wt% MnO would be required for a weld metal manganese content of 1.2 wt%. This, however, ignores the effect of TiO_2 additions which will lower the basicity index and so the neutral point for manganese. Since there was no equilibrium model which considered both MnO and TiO_2 effects, a simple experiment consisting of five test welds was conducted to quantify the MnO and TiO_2 interactions.

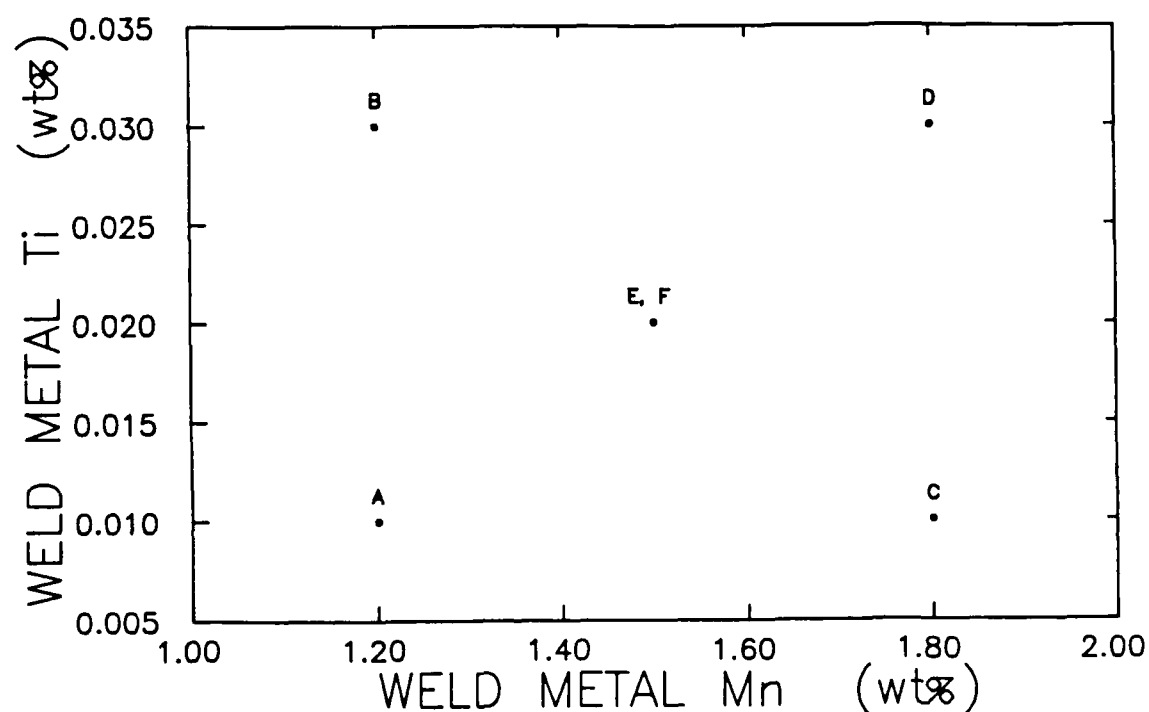


Figure 9. Weld metal compositional matrix.

Based on these test welds the flux systems shown in table 3 were developed (using Oerlikon OP121TT SAW flux as a base) in which the flux identification corresponds to the welds listed in figure 9.

Compound	wt%
MgO	18.19
CaO	16.58
CaF ₂	20.93
SiO ₂	15.45
Al ₂ O ₃	21.81
PbO	0.13
FeO	1.32
TiO ₂	0.72
MnO	0.65
K ₂ O	0.67
P ₂ O ₅	0.22
Na ₂ O	0.74
Loss on Ignition	3.6
% Moisture	0.05
BI	1.4

Table 2. Oerlikon OP121TT flux composition.

Flux	MnO wt%	TiO ₂ wt%
A	5.5	14.5
B	5.5	31.0
C	12.5	14.5
D	12.5	31.0
E, F	8.2	22.5

Table 3. Proposed flux system MnO and TiO₂ contents.

The flux was prepared by adding the MnO and TiO₂ to Oerlikon OP121TT flux, binding the mixture with sodium silicate, and then drying in an oven at 232 °C (450 °F). Following drying, the flux was crushed and then screened to a range from 12 to 100 mesh.

The flux was then stored at 232 °C (450 °F) until it was to be used in the welding process.

2.2.2 Plate Preparation

The base metal used in this investigation was one-half inch HSLA-100 plate produced by Phoenix Steel Corporation for the U.S. Navy David Taylor Research Center.

C	S	O	N	Mn	P	Si	Ni	Cr	Mo	Cu	Ti	V	Al	Zr	B
0.032	0.005	0.0039	0.015	0.80	<002	0.27	3.97	0.65	0.61	1.46	0.002	<001	0.018	<001	<001

Table 4. HSLA-100 plate alloy content.

The plate was rolled from ingots and then austenitized at 900 °C (1650 °F) for 30 minutes followed by water quenching. Aging followed at 690 °C (1275 °F) for 30 minutes with air cooling. The chemical composition of the plate is shown in table 4 where all values are wt%. Hydrogen content was 0.6 ppm.

The weld joint geometry used is shown in figure 10. The plates were cut such that each side was 108 mm (4.25 in) wide before welding. Following welding,

51 mm (2.0 in) was removed from each side to use as future backing bars since the finished plates were wider than necessary for subsequent testing. This was done to minimize the amount of plate needed for the study.

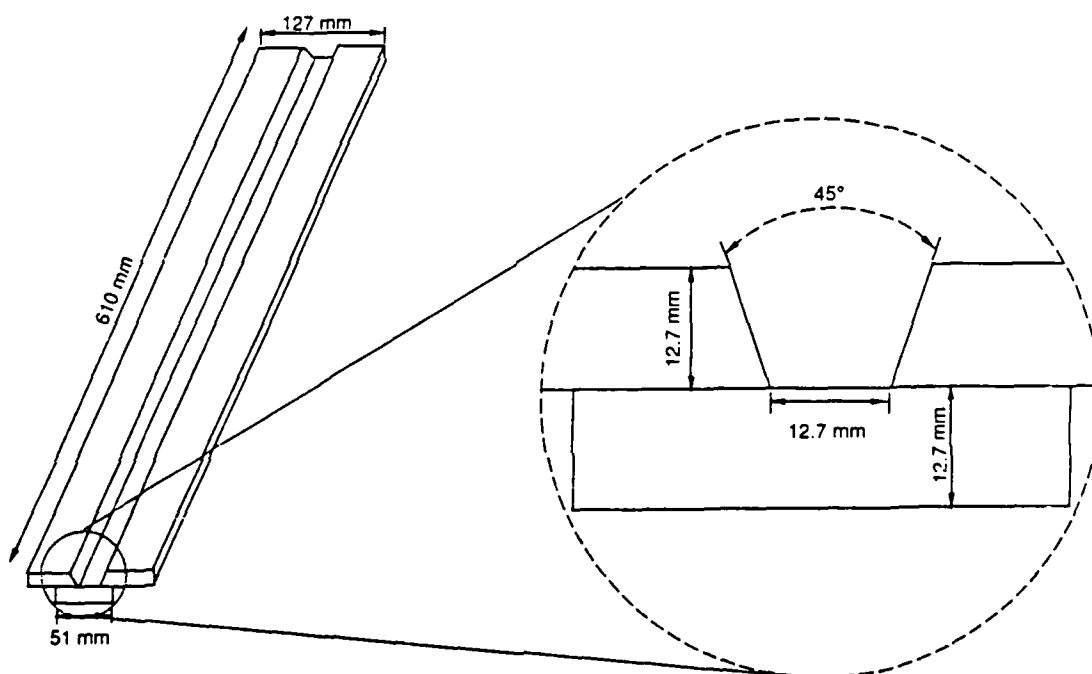


Figure 10. Weld joint geometry.

After rough cutting of the plates, contamination was removed by grinding before tack welding the backing bars, run-on, and run-off tabs. One hole was drilled at the center of the plate length, 12 mm (0.5 in) from the beveled edge so that interpass temperatures could be monitored via a thermocouple.

2.2.3 Welding Procedure

All welding was done using a Linde VI-800 CV/DC power supply with a UCC-8 controller and a Linde EH-10 wire feed head. A Union Carbide "J" Governor was used to control carriage travel speed. A sketch of a submerged arc welding equipment layout is shown in figure 11 for information.

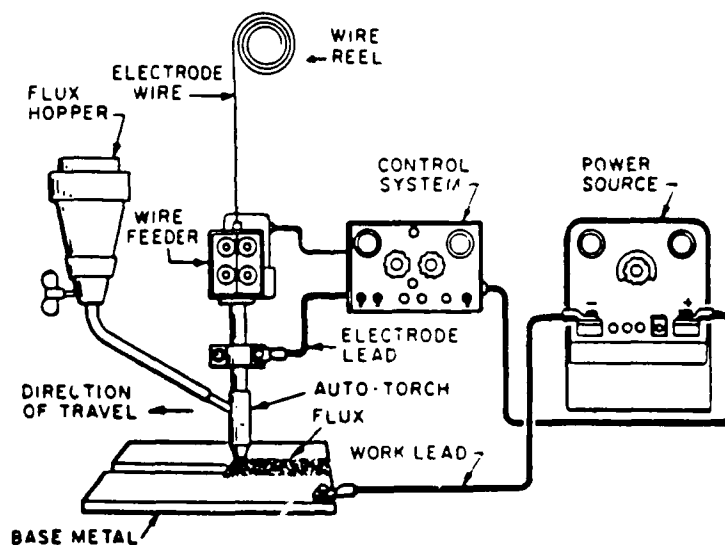


Figure 11. Sketch of SAW equipment.

The voltage for all welds was 33 volts and the current was 400 amperes. Carriage speed was set at 356 mm/min (14.5 in/min) for a nominal heat input of 2.2 kJ/mm (55 kJ/in). Plate ambient temperature was 21 °C (70 °F) with no

preheat applied. Interpass temperature was 82 °C (180 °F) as monitored via the thermocouple located as described in section 2.2.3. Arc voltage was monitored with a digital voltmeter and welding current was measured by sampling the voltage drop across a shunt resistor. The electrode extension was maintained at 25 mm (1 in). The polarity used was D.C., reverse, making the electrode positive.

2.3 Testing and Metallographic Examination

After the completion of welding, the run-on and run-off tabs were removed as well as 51 mm (2.0 in) from each side of the weld as described in section 2.2.2. Specimens were then removed for chemical analysis, metallography, tensile, and Charpy testing as shown in figure 12. The Charpy specimens were machined transverse to the welding direction with notches cut in the plate thickness direction as shown in figure 13. 35.6 mm (1.4 in) gage length all-weld-metal tensile specimens were machined in the longitudinal direction.

The specimens which were mounted for metallography were sectioned as shown in figure 14. This was done so that the microstructure of the successive welds could be examined (orientation B), as well as the prior austenite grain boundaries (orientation A).

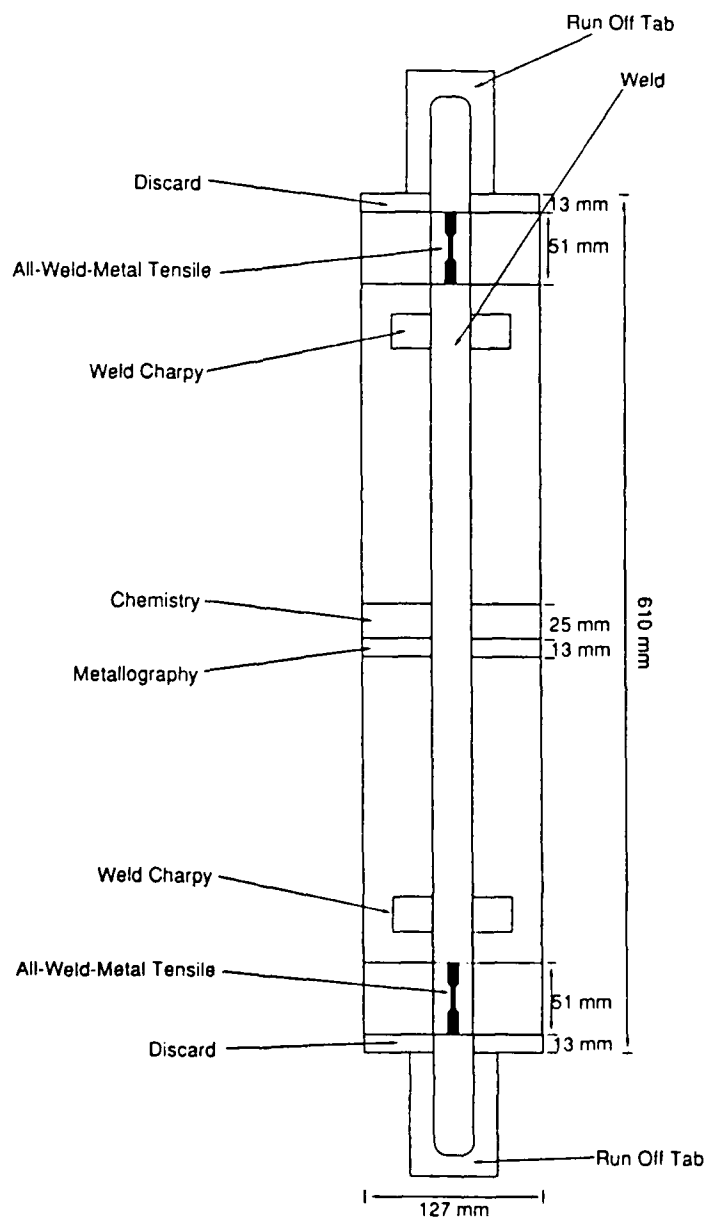


Figure 12. Test plate sectioning for examination.

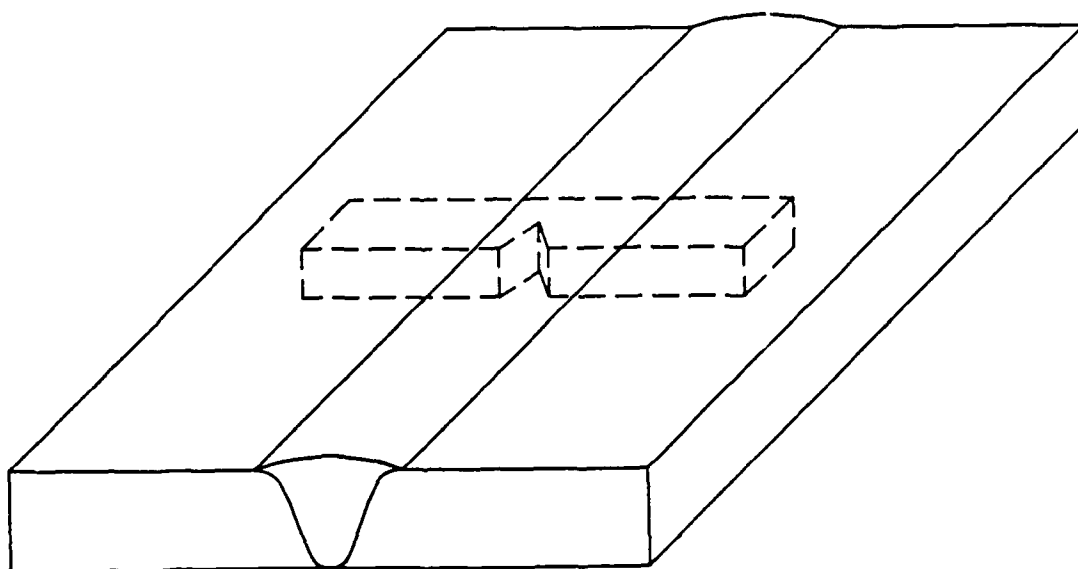


Figure 13. Charpy specimen orientation.

2.3.1 Chemical Analysis

Chemical analysis of the weld metal alloy content was done by LUVAK, Inc. of Boylston, Massachusetts. Five methods of analysis were utilized and are listed in the following table.

Carbon	Combustion Infrared Detection
Sulfur	Combustion Automatic Titration
Oxygen and Nitrogen	Inert Gas Fusion
Hydrogen	Vacuum Hot Extraction
Remaining Elements	Plasma Emission

The confidence limits for this analysis are listed in appendix A.

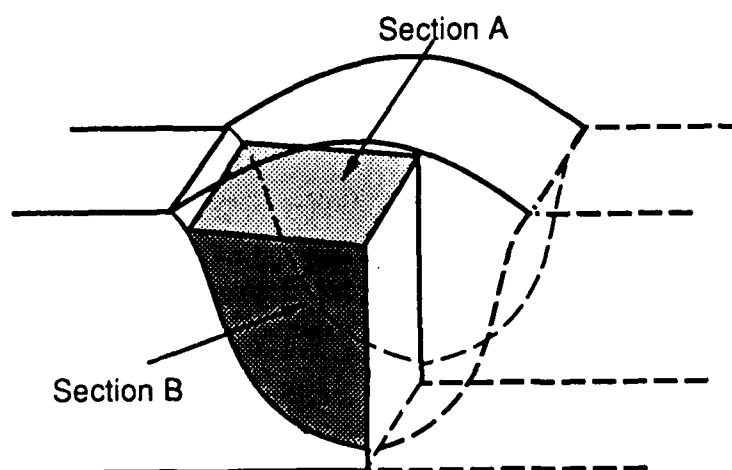


Figure 14. Sectioning for metallography specimens.

2.3.2 Microhardness Testing

A weld metal sample from each weld (orientation B in figure 14) was mounted for metallography. These specimens were then ground and polished using standard metallographic techniques and then etched using 2% nital. Microhardness traverses were made from the root to crown of each weld. Vickers microhardness measurements were made using a diamond indenter with a 500 g load applied for 12 seconds. Reference indentations were also made at this time to be used during optical and SEM microscopy.

2.3.3 Optical Microscopy

Following microhardness testing the weld metal microstructure was examined using a Nikon Epiphot optical microscope. A series of micrographs was taken from an area as shown in figure 15 to characterize the microstructure. The reference area was bounded by the reference microhardness indentations described in section 2.3.2. This area was chosen so that the observed microstructure was one that had been thermally cycled by successive weld passes, and yet was far enough removed from the root passes so that dilution effects would be minimized.

An area 0.35 x 0.40 mm was examined at a magnification of 1000X with micrographs taken so that a montage could be made for quantitative examination of the microstructure.

Table 5 is a summary of the terminology applied to weld metal microstructures by a number of researchers. For the purpose of this study, the metallographic terms proposed by Abson will be used.

Primary ferrite most often nucleates at prior austenite grain boundaries and appears as elongated ferrite veins or a band of equiaxed grains. This is referred to as grain boundary or polygonal ferrite.

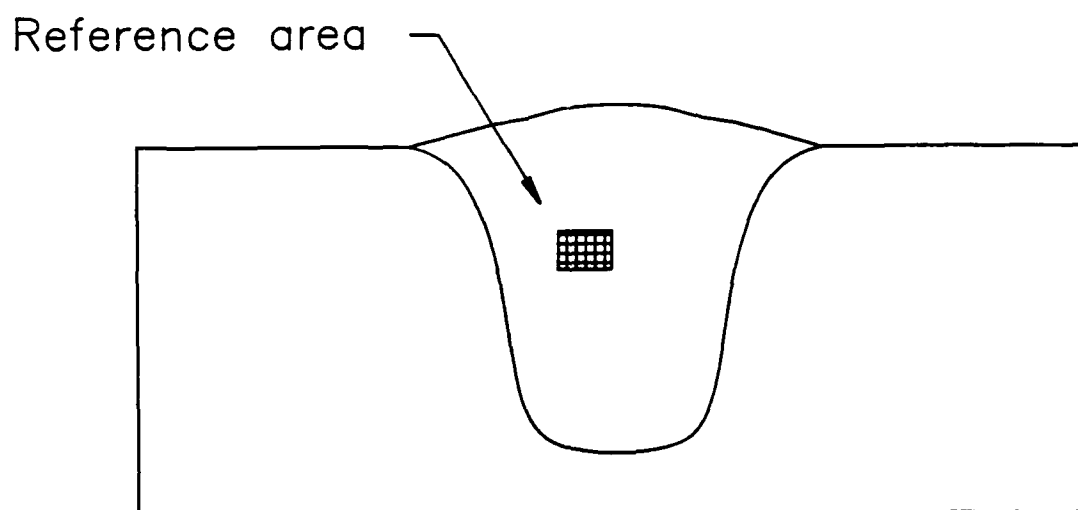


Figure 15. Microscopy reference location.

As the cooling rate is increased, ferrite with an aligned phase forms which is referred to as ferrite with aligned martensite, austenite, or carbide (M-A-C) and occurs at lower transformation temperatures.

Dube, C.A. [31] Aaronson, H.I. [32] Cochrane, R.C. [33]	Widger, D.J. [34]	Abson, D.J. [35]	Others [5, 36-39]	Japanese researchers [40-42]
Allotriomorphic (polygonal ferrite)	Proeutectoid ferrite	Grain boundary ferrite	Proeutectoid ferrite Grain boundary ferrite Polygonal ferrite Blocky ferrite	Proeutectoid ferrite Grain boundary ferrite Polygonal ferrite
		Polygonal ferrite	Ferrite islands	Polygonal ferrite
	Lamellar component (product)	Ferrite with aligned M-A-C	Ferrite sideplate Lath ferrite Upper bainite	Ferrite sideplates Lath-like ferrite
Primary and secondary ferrite sideplates				
Intragranular ferrite plates	Acicular ferrite	Acicular ferrite	Acicular ferrite Fine bainitic ferrite	Acicular ferrite Needle-like ferrite Fine grained ferrite
Massive ferrite				Granular ferrite
Microphases			Granular ferrite	
Pearlite	Pearlite	Ferrite-carbide aggregate	Pearlite	
Lath martensite	Martensite	Martensite	Martensite	
Twinned martensite		M-A constituent	M-A constituent	
Retained austenite			High-C martensite	
Upper/lower bainite			Upper bainite	

Table 5. Classification of microstructures in low C-low alloy steel. [43]

When the transformation temperature is lower than that required for ferrite with aligned M-A-C, acicular ferrite forms. This phase, as described in chapter one, nucleates intergranularly throughout the prior austenite grains, producing an interlocking grain structure with high misorientation.

At very rapid cooling rates, martensite and bainite can form at low transformation temperatures. Bainite exists as a highly dislocated lath structure which may include aligned carbides. The formation of these phases is more likely when the weld metal has a high level of alloying additions.

Prior austenite grain size was measured by sectioning as shown in figure 14, orientation A. This section orientation was chosen (perpendicular to the columnar grains) so that approximately equiaxed grains could be observed. This was done since austenite grain size measured on a transverse section would not correspond to true austenite grain size due to the columnar orientation.

The etchant used to resolve the prior austenite grain boundaries was 100 ml of Winsteads etchant with 1 ml HCl at room temperature. The Winsteads etchant was prepared by combining 20 ml ethanol, 4 g picric acid, 400 ml distilled water, and 2 g sodium tridecylbenzene sulfonate. The sample was agitated in an ultrasonic cleaner with the etchant for 30 seconds followed by cleaning ultrasonically in methanol. Prior austenite grain size measurement was done using an austenite reticle in the optical microscope. A summary of the etchants used in this investigation is provided in appendix B.

2.3.4 Scanning Electron Microscopy

A Cambridge 250 Mk3 scanning electron microscope was used to examine the inclusions and the M-A constituent in the weld metal. The inclusions were first examined after etching in 2% nital. A montage was taken covering a 0.035 mm x 0.35 mm strip at a magnification of 5000X to be used for inclusion size measurement and volume fraction calculations. The SEM was chosen over the optical microscope for inclusion examination because of the relatively small size

of the inclusions, approximately $0.5\text{ }\mu\text{m}$. An x-ray spectrometer (TRACOR Northern), part of the SEM, was used for quantitative analysis of the inclusions. Although the average size of the inclusions was small, the largest were approximately $2\text{ }\mu\text{m}$, and these were analyzed with the x-ray spectrometer.

Next the specimens were repolished in preparation for electrolytic etching to reveal the M-A constituent. This was a two step electrolytic etching process proposed by Ikawa [10]. The electrolyte for the first etching was 5 g EDTA (ethylenediamine tetracetic acid), 0.5 g sodium fluoride, and 100 ml distilled water. This etchant attacks only the ferrite, leaving the M-A constituent and carbides in an embossed condition. Etching conditions were 6.5 V for 15 seconds.

The electrolyte for the second etching was 5 g picric acid, 25 g sodium hydroxide, and 100 ml distilled water which preferentially etched any carbides. Etching conditions were 6 V for 30 seconds. At this point all phases were depressed except the martensite and retained austenite which would appear as embossed islands.

For etching, the samples were in a phenolic mount with all but 0.7mm^2 (0.1 in^2) of the polished surface electrically masked to limit the anodic area. Masking was accomplished by covering the surface with a piece of electrician's tape with a 1.4 mm (0.35 in) diameter hole removed.

The etched surface was then observed at a magnification of 10,000 with a series of micrographs taken for quantitative metallography.

Attempts to analyze the M-A fraction using secondary ion mass spectroscopy (SIMS) were not successful. It was surmised that the martensite and retained austenite, having an increased carbon fraction, could be detected by the SIMS equipment. However, no correlation could be obtained between the SIMS data and the observations from the electrolytically etched surface examined with SEM.

2.3.5 Tensile and Charpy Testing

Tensile and impact testing were performed by the U.S. Navy David Taylor Research Center. The following data was recorded as a function of test temperature.

- a. Absorbed energy, in J (ft-lb).
- b. Lateral expansion.
- c. Percentage of fracture surface area in fibrous appearance.

The following values were then plotted to determine:

- a. The temperature at which the amount of energy absorption decreased to one-half of the upper shelf energy at high temperature. This energy value is referred to as TrE.
- b. The temperature which corresponded to a 50% fibrous fracture appearance which is referred to a Trs. This may also be referred to as the fibrous appearance transition temperature (FATT).

Next, examination of the Charpy fracture surfaces was undertaken to correlate the crack propagation path with the microstructure. Charpy specimens with a large percentage of cleavage fracture were chosen because low temperature performance was of primary concern. The fracture surface was first examined at low magnification using a binocular microscope. This was done so that locations of interest could be identified before using the SEM for detailed examination.

Next, the SEM was used to obtain micrographs of the M-A microstructure from the corresponding weld specimen which had been prepared as described in section 2.3.4. Since the micrographs taken during this stage of examination were to be used in correlating the microstructure with the fracture surface, it was important that the magnifications chosen would be the same as those used in examination of the fracture surface. It was also important that the tilt angle

was identical for both sets of micrographs. This is the angle in the SEM between the specimen surface and the detector. By keeping this angle the same, the distortion in the photographs would be the same, making the correlation between microstructure and fracture easier.

Fractographs were taken of initiation sites at magnifications of 1000X, 2000X, 5000X, and 10,000X to compare with micrographs of the M-A structure taken at the same magnification.

Subsurface cracks near the major fracture surface were also of interest so a second set of specimens was prepared by first sectioning so that a surface perpendicular to the fracture surface could be polished and then etched. This would permit the microstructure to be observed along the plane of the crack propagation.

After sectioning, the specimens were mounted using phenolic powder, and then successively ground with the final grinding on 600 grit paper. Polishing was done on nylon covered polishing platens using 9 μm and 1 μm diamond polishing compound. Nylon polishing cloths and minimum polishing times were used to minimize edge rounding of the cracks of interest.

After polishing was completed, the specimens were electrolytically etched as described in section 2.3.4 to resolve the M-A constituent. Examination using the SEM followed etching.

2.4 Summary

In summary, a series of six multiple pass welds was made with varying titanium and manganese contents due to doping of the SAW flux. Quantitative metallography was used to characterize the weld microstructures. The weld metal properties were measured via all weld metal tensile tests and Charpy V-notch testing.

CHAPTER 3

Results and Discussion

The data from this investigation will be presented in tabular form for reference and then graphically for discussion purposes. Trends and correlations will be discussed in terms of the data presented in various graphs. Also included in the discussion will be micrographs, both optical and SEM, depicting the weld metal microstructures. Finally the mechanical property data, tensile and Charpy V-notch, will be discussed with correlations involving the observed microstructures. Fractographs highlighting specific features of the fracture surfaces will also be presented.

Emphasis will be on the analysis of the weld metal inclusions and the effect of titanium on the formation of these inclusions. Also emphasized will be the formation of martensite and retained austenite and the effect of this phase on the mechanical properties of the weld metal.

3.1 Data Summary

Table 6 shows the weld metal composition for each weld with the base plate and electrode alloy content included for reference. Note that the titanium content varies from 0.012 to 0.025 wt% and the manganese content varies from 1.08 to 1.86 wt%. These ranges are reasonable when compared to the target ranges of 0.01 to 0.03 wt% for titanium and 1.2 to 1.8 wt% for manganese.

In all of the welds, the oxygen content is higher than would be expected from welds made with Oerlikon OP121TT flux. The increased levels are due to the additions of TiO_2 to the flux system which reduced the basicity index as shown in table 7.

	C	S	O	N	Mn	P	Si	Ni	Cr	Mo	Cu	Ti	V	Al	Zr	B	H (ppm)
A	0.034	0.014	0.047	0.006	1.07	0.012	0.25	2.88	0.46	0.56	0.96	0.012	0.001	0.013	0.001	0.004	2.3
B	0.033	0.007	0.050	0.006	1.08	0.011	0.27	2.67	0.38	0.56	0.60	0.025	0.002	0.007	0.001	0.005	0.7
C	0.036	0.007	0.055	0.006	1.86	0.016	0.20	2.45	0.30	0.51	0.15	0.017	0.003	0.006	0.001	0.003	3.2
D	0.039	0.009	0.058	0.007	1.17	0.029	0.18	2.54	0.27	0.53	0.12	0.025	0.002	0.005	0.001	0.002	1.1
E	0.039	0.005	0.047	0.006	1.57	0.028	0.22	2.47	0.29	0.49	0.10	0.018	0.003	0.005	0.001	0.001	2.0
F	0.040	0.007	0.053	0.008	1.52	0.018	0.25	2.56	0.31	0.50	0.24	0.020	0.002	0.006	0.002	0.003	2.5
plate	0.032	0.005	0.0039	0.015	0.80	<002	0.27	3.97	0.55	0.61	1.48	0.002	<001	0.018	<001	<001	0.6
wire	0.076	0.009	0.006	0.004	1.35	0.010	0.007	2.65	0.26	0.43	0.014	0.016	<001	0.012	0.015	0.003	1.3

Table 6. Weld metal alloy summary.

	MgO	CaO	CaF ₂	SiO ₂	Al ₂ O ₃	FeO	TiO ₂	PbO	MnO	K ₂ O	P ₂ O ₅	Na ₂ O	Loss	BI ²
A	16.83	7.54	18.78	16.20	14.25	0.91	15.30	0.26	3.92	0.59	0.21	2.11	3.7	0.95
B	17.32	6.49	19.15	16.17	14.08	0.99	14.01	0.26	5.79	0.55	0.20	2.07	3.6	0.99
C	13.16	7.87	15.90	16.13	12.12	0.76	15.89	0.26	9.29	0.58	0.18	2.28	5.8	0.96
D	14.89	5.03	13.68	11.83	9.41	0.63	32.38	0.22	5.34	0.51	0.27	2.01	3.6	0.78
E	16.73	6.94	15.74	14.41	11.69	0.81	21.43	0.25	6.40	0.57	0.20	2.36	2.9	0.98
F	12.09	6.00	16.07	14.13	10.82	0.64	27.35	0.25	6.63	0.60	0.21	2.18	3.5	0.73
OP121TT	18.19	16.58	20.93	15.45	21.81	1.32	0.72	0.13	0.65	0.67	0.22	0.74	3.6	1.39

Table 7. Flux system composition summary.

	Hv (ave)	P _{cm}	Primary Ferrite %	Ferrite w/Algn %	Acicular Ferrite %	M-A %	Boundary Intercept μm	Austenite Grain Sz. μm	Nr Incl, per mm ³ $\times 10^7$	Inclusion Volume %	Inclusion Size Max. μm	Inclusion Size Mean μm
A	273	0.25	14.4	5.0	76.2	4.4	4.8	55	5.46	0.22	1.04	0.33
B	279	0.23	15.1	5.6	74.2	5.1	3.9	75	1.83	0.38	2.67	0.49
C	282	0.26	11.3	5.4	78.0	5.3	4.1	50	3.38	0.26	1.19	0.40
D	269	0.22	43.6	1.0	52.3	3.1	7.3	55	3.78	0.49	1.78	0.47
E	271	0.24	47.5	3.1	43.4	6.0	4.6	75	3.75	0.27	1.19	0.41
F	276	0.25	7.6	1.1	87.1	4.2	3.6	65	4.66	0.34	1.63	0.39

Table 8. Summary of quantitative metallography data.

The chemical composition of the flux systems for welds A through F is shown in table 7. Included for reference in the table is the composition of the Oerlikon OP121TT flux used as the base. Note the systematic change in manganese and titanium oxides which were adjusted as described in section 2.2.1.

Table 8 is a summary of the results of quantitative metallography for each of the welds characterizing the weld metal microstructure. Note here the reduction in the acicular ferrite fraction in welds D and E which will be discussed in section 3.2.4.

3.2 Weld Metal Microstructures

Figure 16 is a macro photograph of one of weldments which is representative of the series of welds, A through F. The solidification structure was etched with a nital macro etchant and is shown at an approximate magnification of 4.5X.

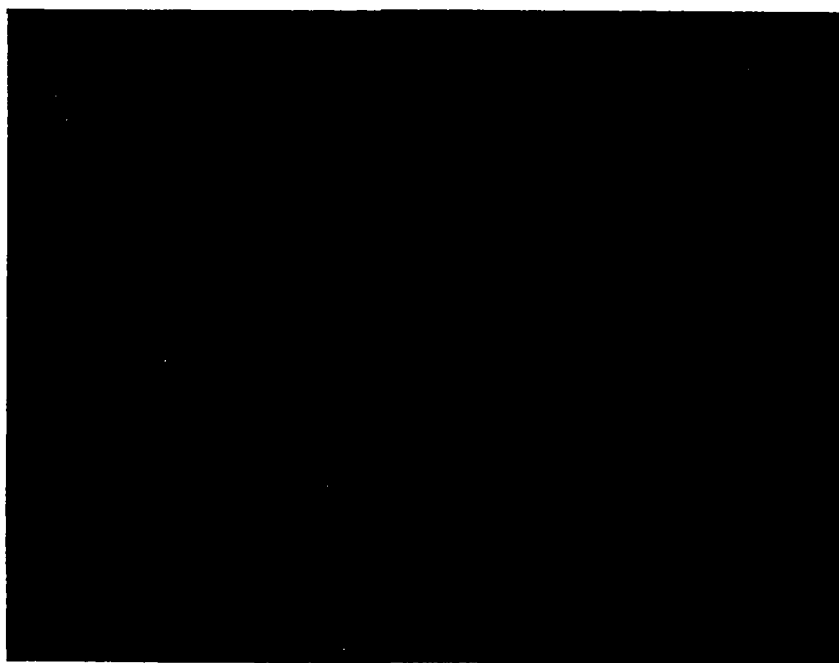


Figure 16. Macro photograph of a representative weldment.

The weld metal microstructures of the six weldments are shown at a magnification of 400X in figures 17 through 22. These micrographs represent the center line microstructures of each weldment as shown in figure 15 and were selected to be representative of the overall weld metal microstructure.

The microstructural fineness, as expressed by the mean linear intercept, and the volume percent of the microconstituents present are summarized in table 9. Microconstituent designations used in the analysis were summarized in table 6.

In the following sections the correlation factor, r^2 , will be used to quantify the data values and the estimated values determined by the line or curve fit shown on each graph. The correlation factor expresses the proportion of the variation in Y related to the variation of X.

The value r^2 is calculated by dividing the total variation by the explained variation. The total variation represents the sum of the squared deviations between the actual values and the mean value of the sample, while the explained variation represents the sum of the squared deviations between the estimated values and the mean value of the sample.

A value of $r^2=0.80$, would indicate 80 percent certainty that the Y value is related to the value of X on the graph in question.

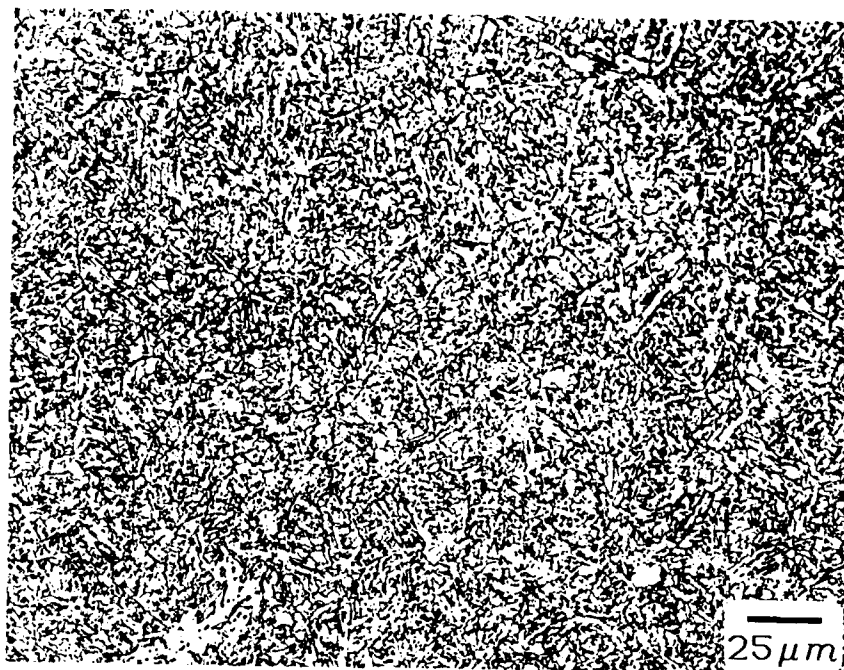


Figure 17. Weldment A weld metal microstructure, 2% nital.

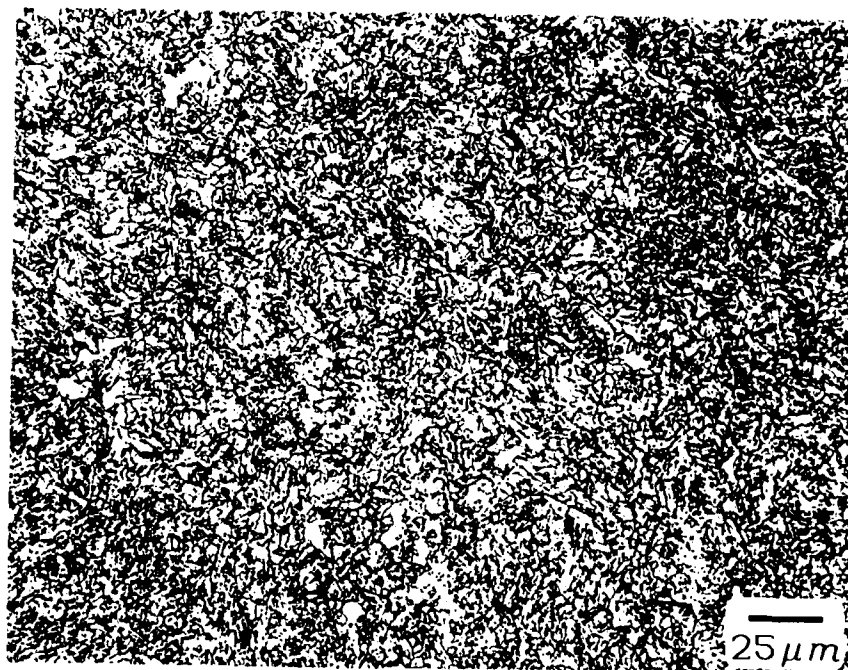


Figure 18. Weldment B weld metal microstructure, 2% nital.

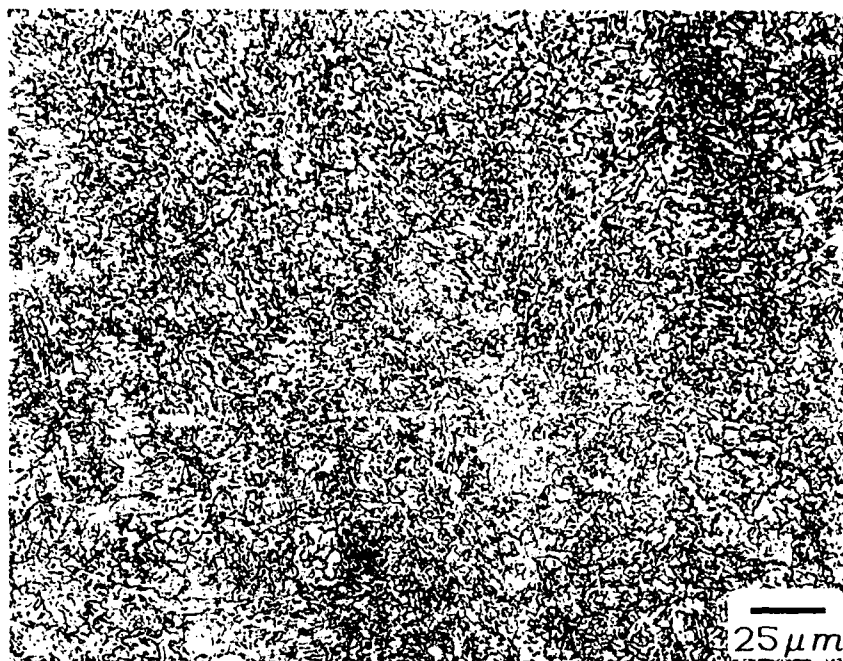


Figure 19. Weldment C weld metal microstructure, 2% nital.

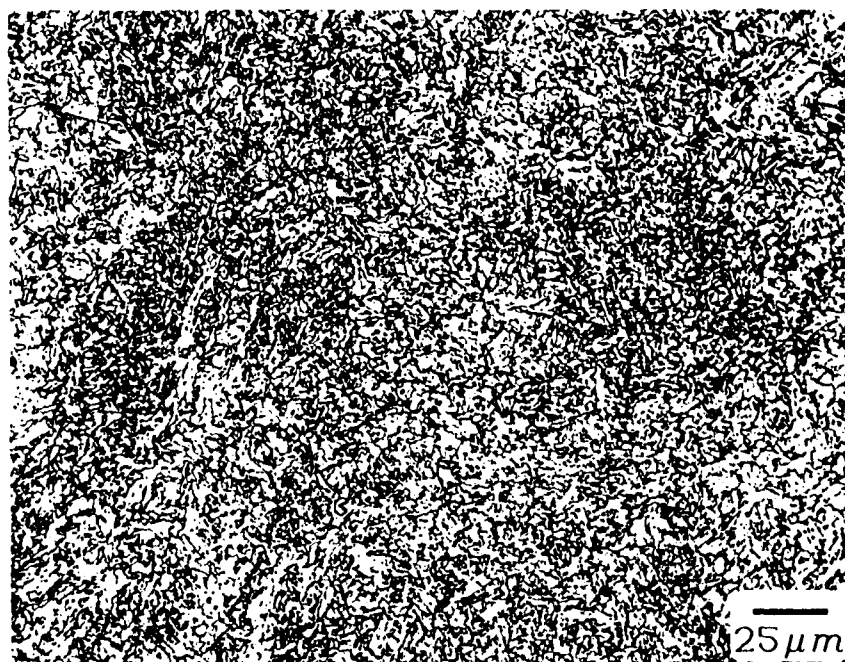


Figure 20. Weldment D weld metal microstructure, 2% nital.

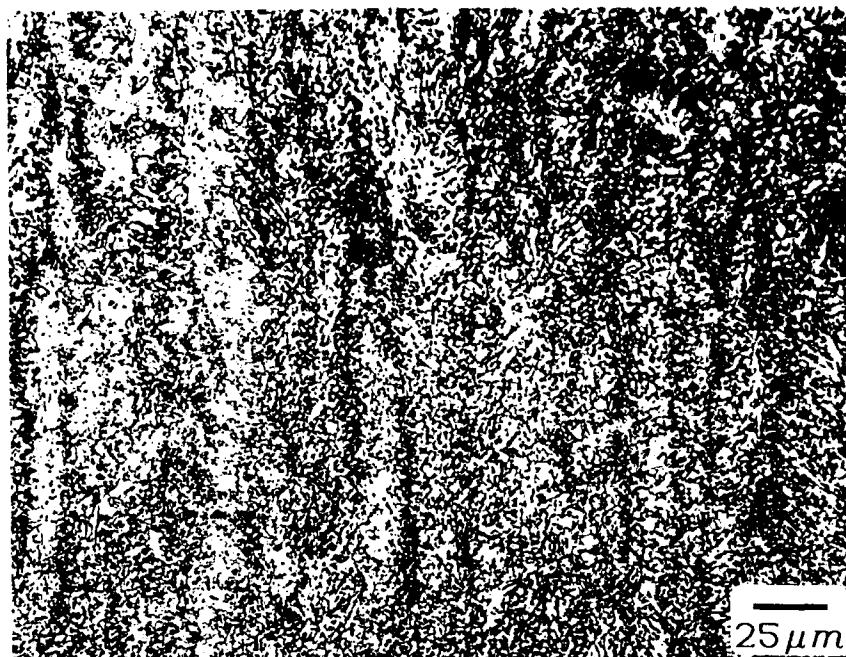


Figure 21. Weldment E weld metal microstructure, 2% nital.

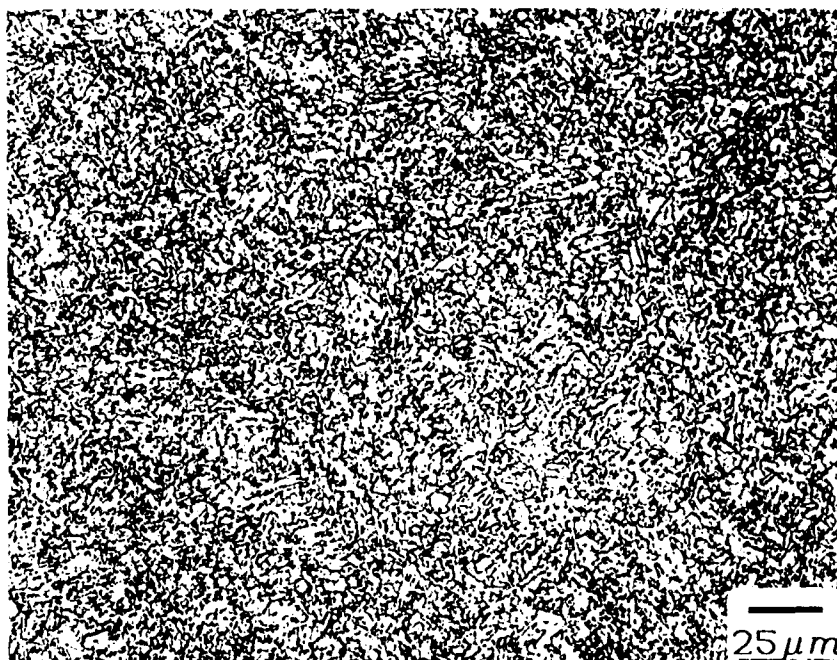


Figure 22. Weldment F weld metal microstructure, 2% nital.

3.2.1 Titanium Effects

Since titanium was one of the alloying elements which was systematically varied in this study, it was of interest to analyze its effect on the weld metal microstructure. The volume fraction of acicular ferrite was first evaluated by plotting the wt% titanium versus the volume fraction of acicular ferrite as shown in figure 23. From this figure it is apparent that the variation of 0.012 to 0.025 wt% titanium has little direct correlation with the acicular ferrite fraction in these welds. This is because the range over which the titanium was varied is well within the preferred range of 0.01 to 0.03 wt% which was discussed in chapter one. The available titanium formed titanium nitrides, thus protecting the available boron from forming boron nitrides. However, this still did not explain the effect of titanium in the weld metal.

A far stronger correlation was observed between the titanium level in the weld metal and both inclusion size and volume fraction. Figure 24 shows the strong influence of titanium on the mean inclusion size. Figure 25 shows that with increasing wt% titanium, the inclusion volume of the weld metal increased. Finally, figure 26 shows a decreasing number of inclusions as the wt% titanium is increased.

Since these inclusions provide nucleation sites for acicular ferrite, it is advantageous to optimize the formation of the inclusions with regard to size and number in the weld metal.

In this study the variation in inclusion volume percent ranged from 0.22% to 0.49% and the number of inclusions per mm^3 was of the order of 10^7 for all of the welds. The mean inclusion size varied from 0.33 to 0.49 μm .

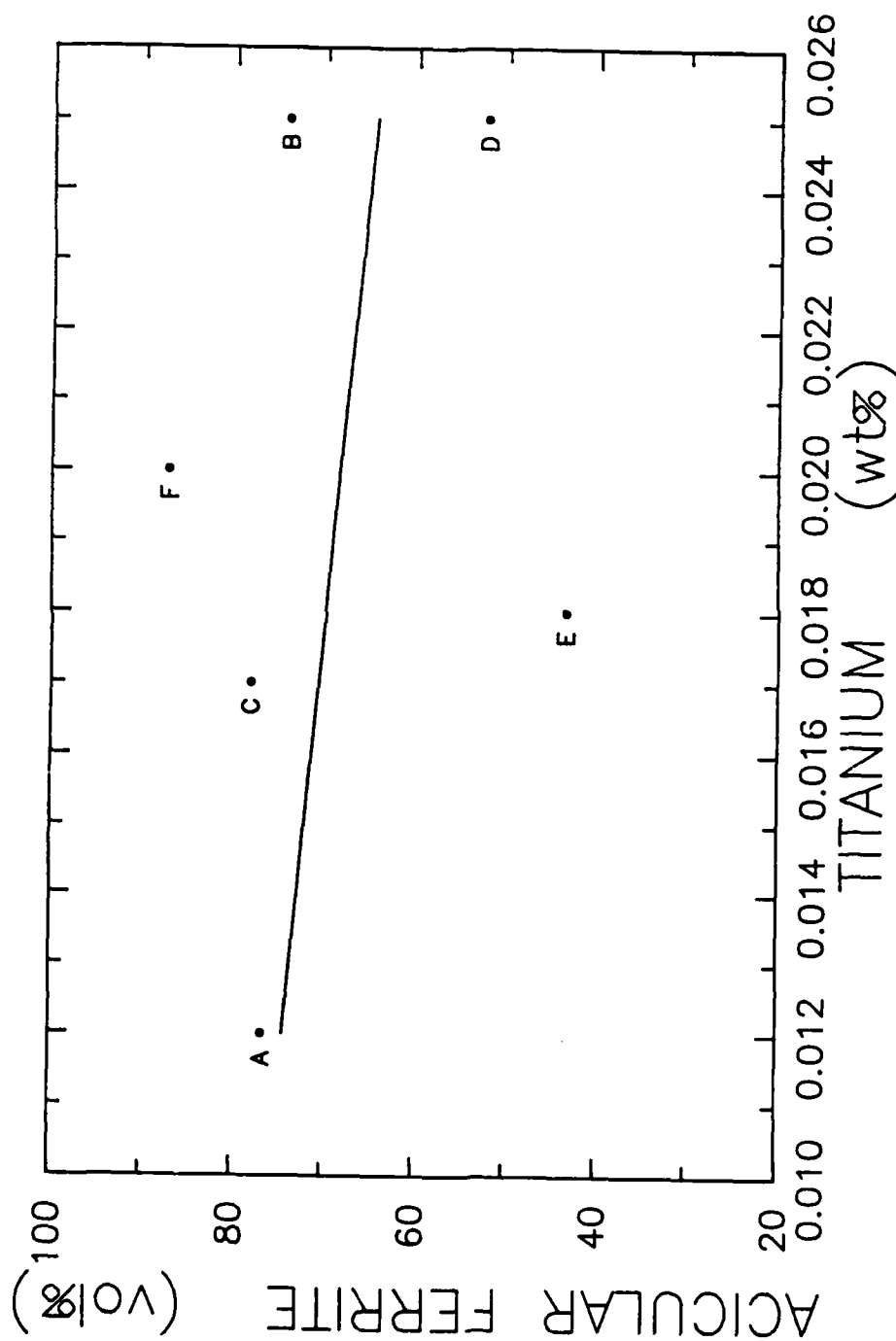


Figure 23. Ti content versus acicular ferrite fraction. ($r^2=0.05$)

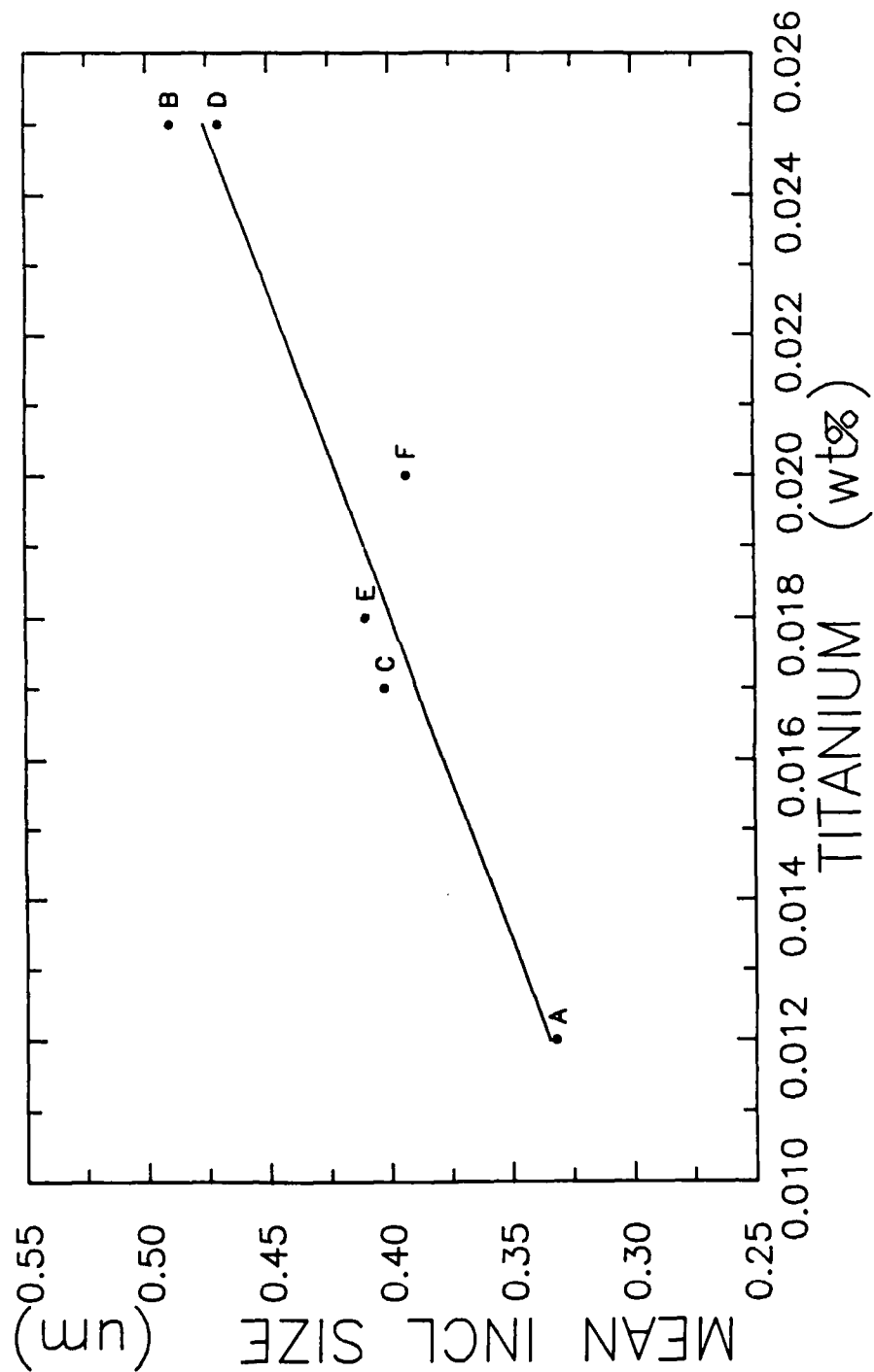


Figure 24. Ti content versus mean inclusion size. ($r^2=0.92$)

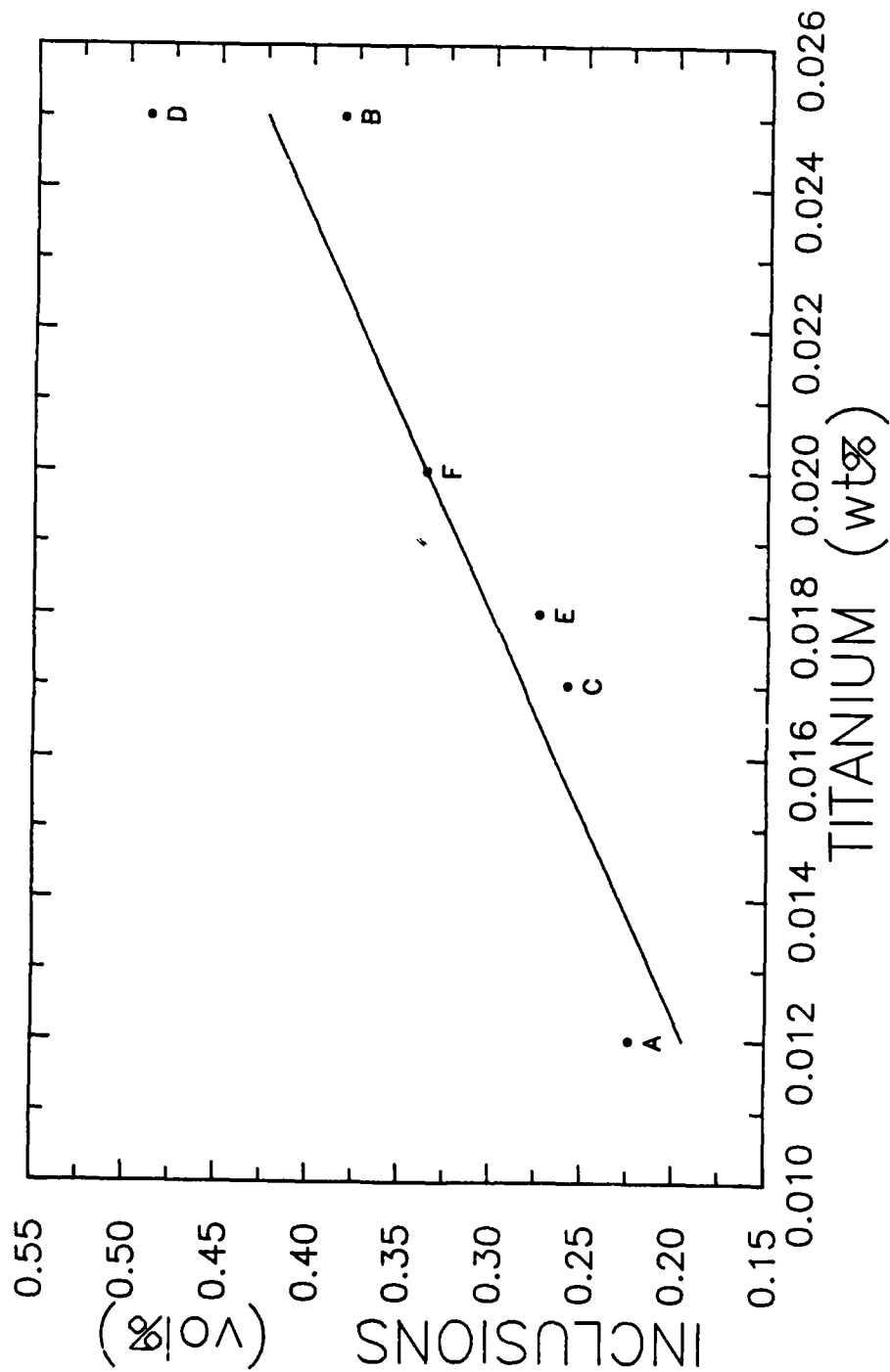


Figure 25. Ti content versus weld metal inclusion volume. ($r^2=0.83$)

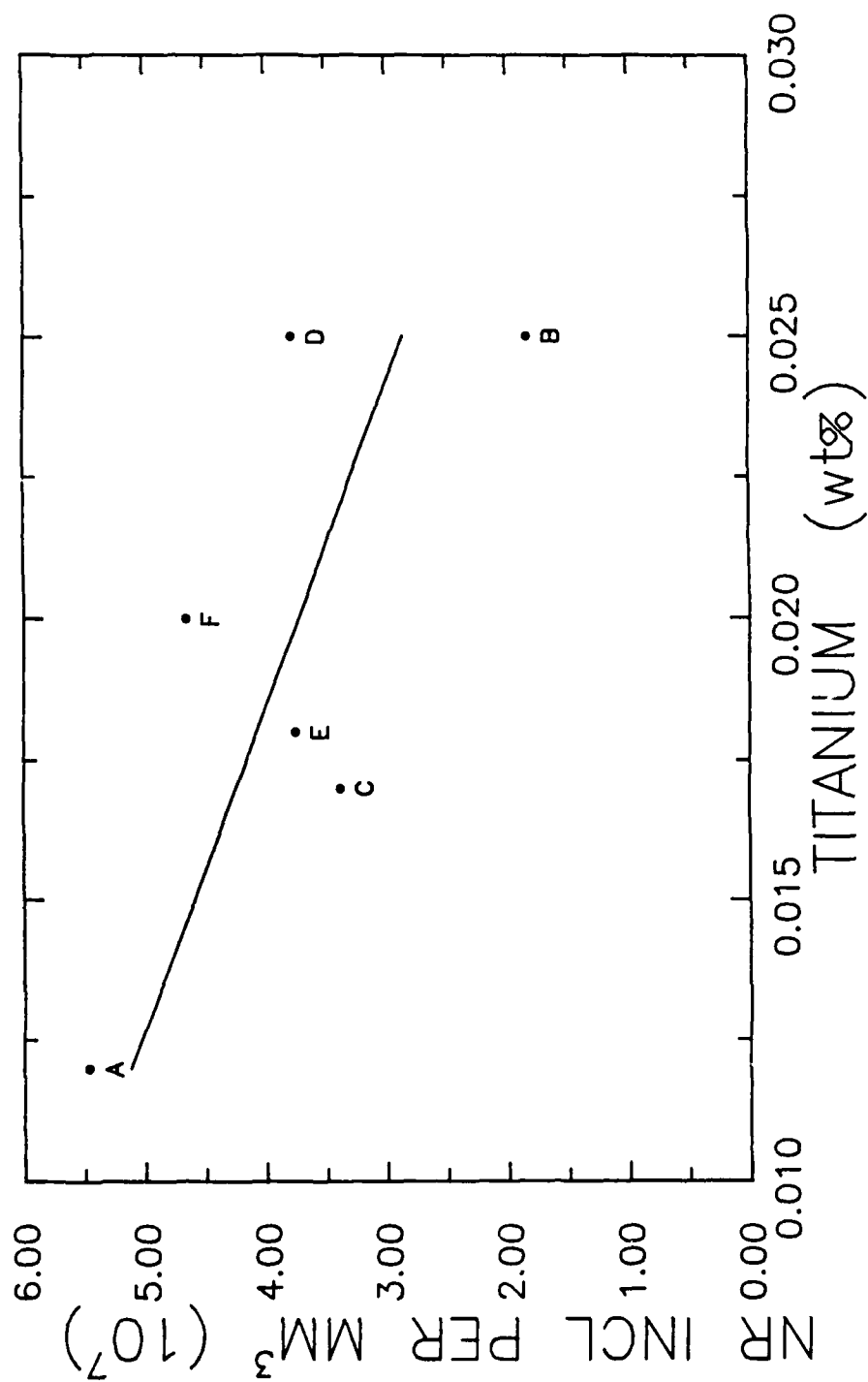


Figure 26. Ti content versus number of weld metal inclusions. ($r^2=0.50$)

This data explains in part why there was little correlation between titanium and acicular ferrite in this study. Since the mean inclusion size was well within the optimum range of 0.40 to 0.60 μm proposed by Jang *et al.* [6], the available inclusions were favorable nucleation sites. The available number of inclusions was approximately equal for all of the welds so that the opportunity for acicular ferrite nucleation was similar in all cases.

Examination of these trends showed that titanium should be limited to a minimum range since excessive amounts not only decreased the number of available nucleation sites, but also increased the mean inclusion size.

The formation of the weld metal inclusion then becomes important since it is these nucleation sites that are important in the transformation of the weld metal microstructure. The structure of these inclusions was resolved during the two step electrolytic etching process described in section 2.3.4. Following etching, it was observed that portions of the weld metal inclusions were preferentially etched away, leaving a small faceted particle. Figures 27 and 28 are typical examples of the appearance of the inclusions following etching when examined by SEM. Examination of welds A through F showed faceted particles to be present in a large portion of the inclusions. It may be postulated that a particle was present in every inclusion and some were lost during the etching process and subsequent preparation for SEM examination.

Based on the angular, faceted shape of the particles, it is believed that the particles are titanium nitrides. To quantitatively examine the particles, a Perkin Elmer PHI 600 Scanning Electron Multiprobe was used. Using this instrument Auger electron spectroscopy was carried out on a small area within a few angstroms of the particle surface. Beam energy was 3kV and beam current at the surface was 0.2 nA. The small beam current resulted in a relatively small activation volume which was necessary for examining particles in the submicron range.

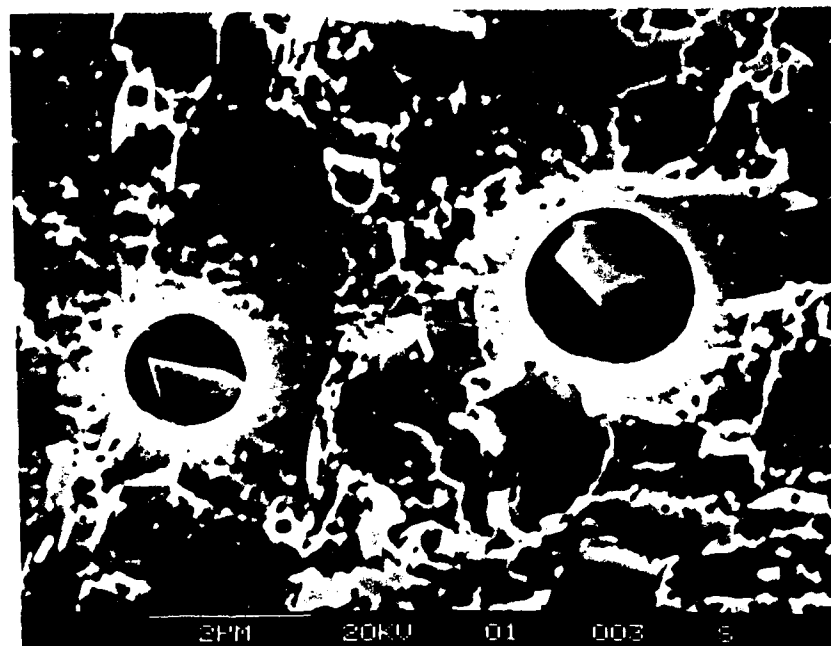


Figure 27. Example of faceted inclusion particle. Electrolytically etched.

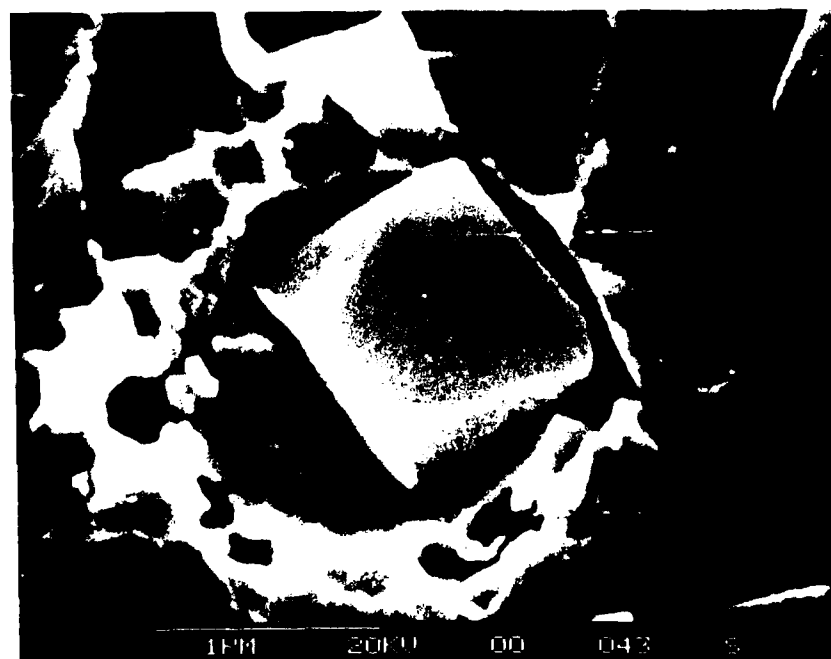


Figure 28. Example of faceted inclusion particle. Electrolytically etched.

The specimen surface first was cleaned using argon ion sputtering to remove any contamination present. Figure 29 shows an Auger spectrum after one minute of sputtering. Note that the principal elements are titanium, nitrogen, oxygen, and manganese.

Figure 30 is an Auger spectrum of the same particle as in figure 29 after five minutes of argon ion sputtering. Here the manganese peaks are reduced indicating that manganese (oxides and/or silicates) surrounded the particle and was not completely removed in the electrolytic etching process. A sharpening of the particle features was also noted after five minutes of sputtering.

Table 9 is a quantitative analysis of the inclusion particle examined with the Auger equipment. Note that in this technique the results are dependent upon the sensitivity factor used and so the data should be viewed as relative values rather than the actual fraction of elements present.

Element	Sensitivity Factor	Weight Percent
Titanium	0.23	16
Nitrogen	0.16	30
Oxygen	0.35	38
Manganese	0.15	16

Table 9. Inclusion particle Auger element analysis.

For comparison, table 10 shows SEM energy dispersive X-ray analysis of a representative inclusion prior to electrolytic etching. Recall that nitrogen and oxygen cannot be detected by this method. Also, beam size is on the order of 2 μm so analysis was done on an inclusion of appropriate size.

Element	wt%
Titanium	20
Manganese	53
Silicon	20
Aluminum	7

Table 10. Inclusion SEM X-ray element analysis.

Since the particles are composed primarily of titanium, oxygen, and nitrogen, and both oxygen and nitrogen are readily available in the molten weld pool, titanium then becomes the controlling element in the formation of the faceted particles. Further, it is believed the size and population of the weld metal inclusions is controlled by the size and population of the faceted particles.

In summary, the titanium content in the weld metal should be as low as possible with enough present so that the available boron is protected from any nitrogen. In this study the optimum level is the lowest, 0.012 wt% titanium based on producing a large fraction of acicular ferrite (76 %), the highest tensile yield 675 MPa (98 ksi), and Charpy impact energy of 62 J (46 ft-lb) at -51 °C (-60 °F).

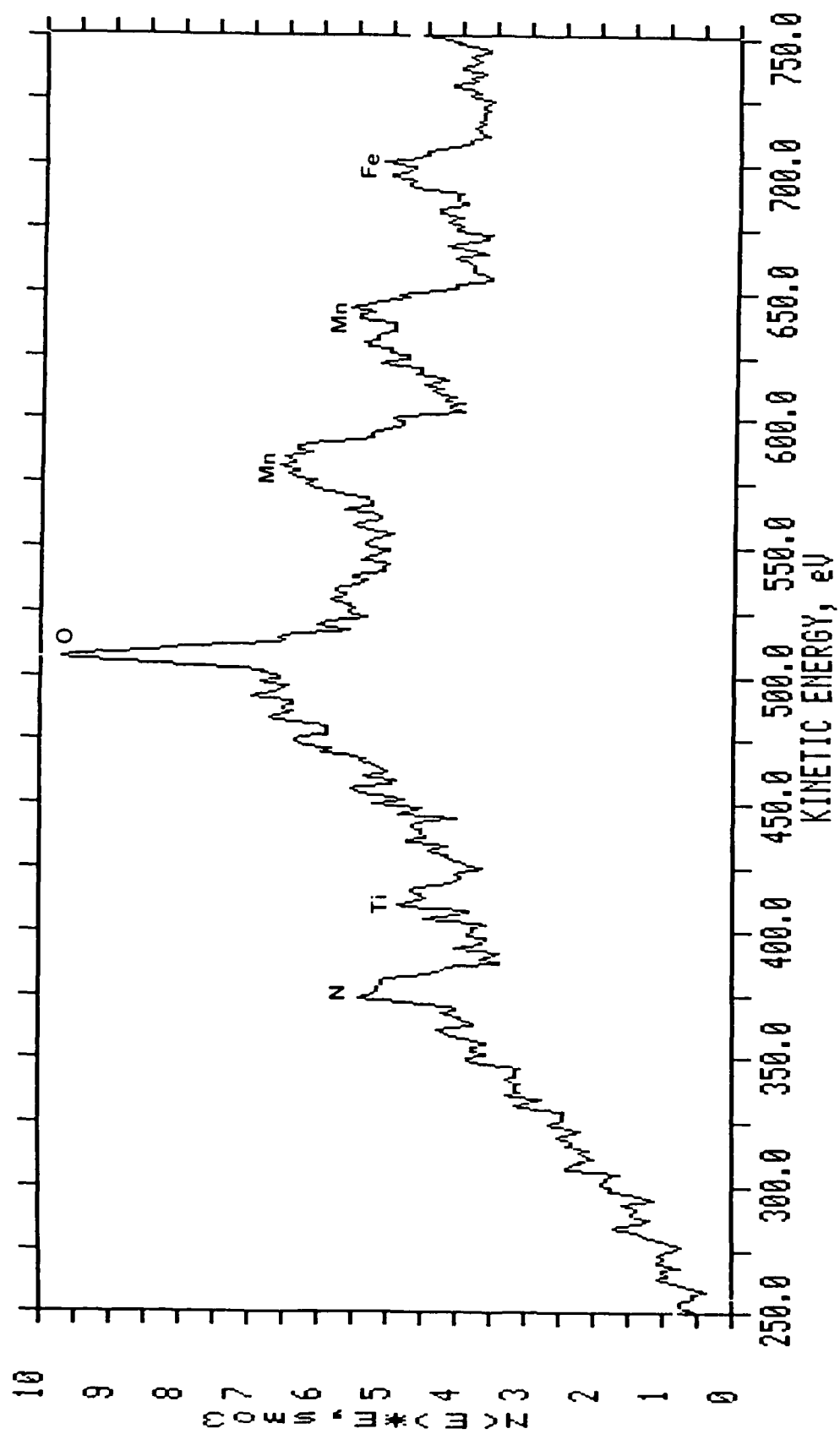


Figure 29. Inclusion particle Auger spectrum after one minute of ion sputtering.

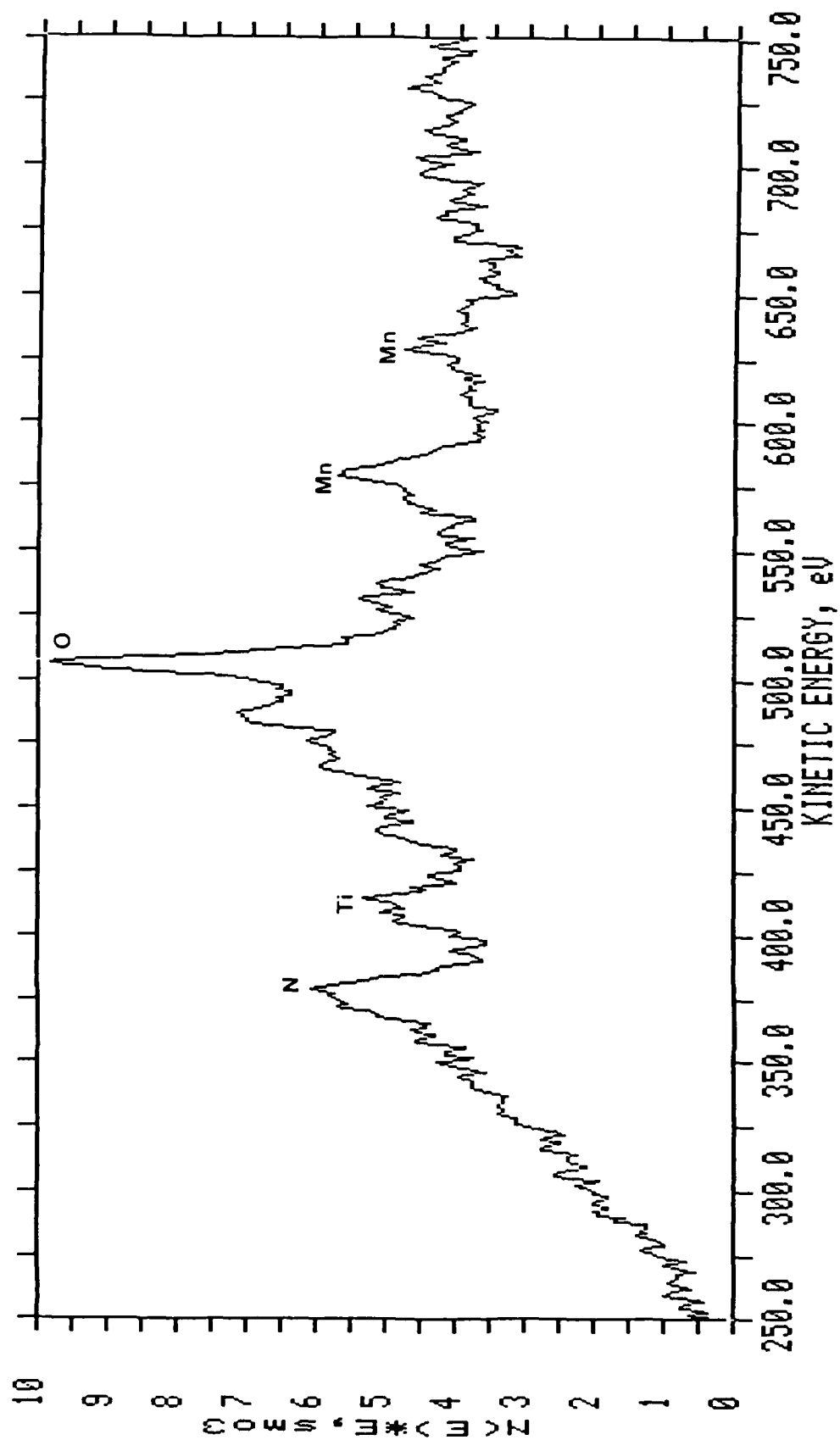


Figure 30. Inclusion particle Auger spectrum after five minutes of ion sputtering.

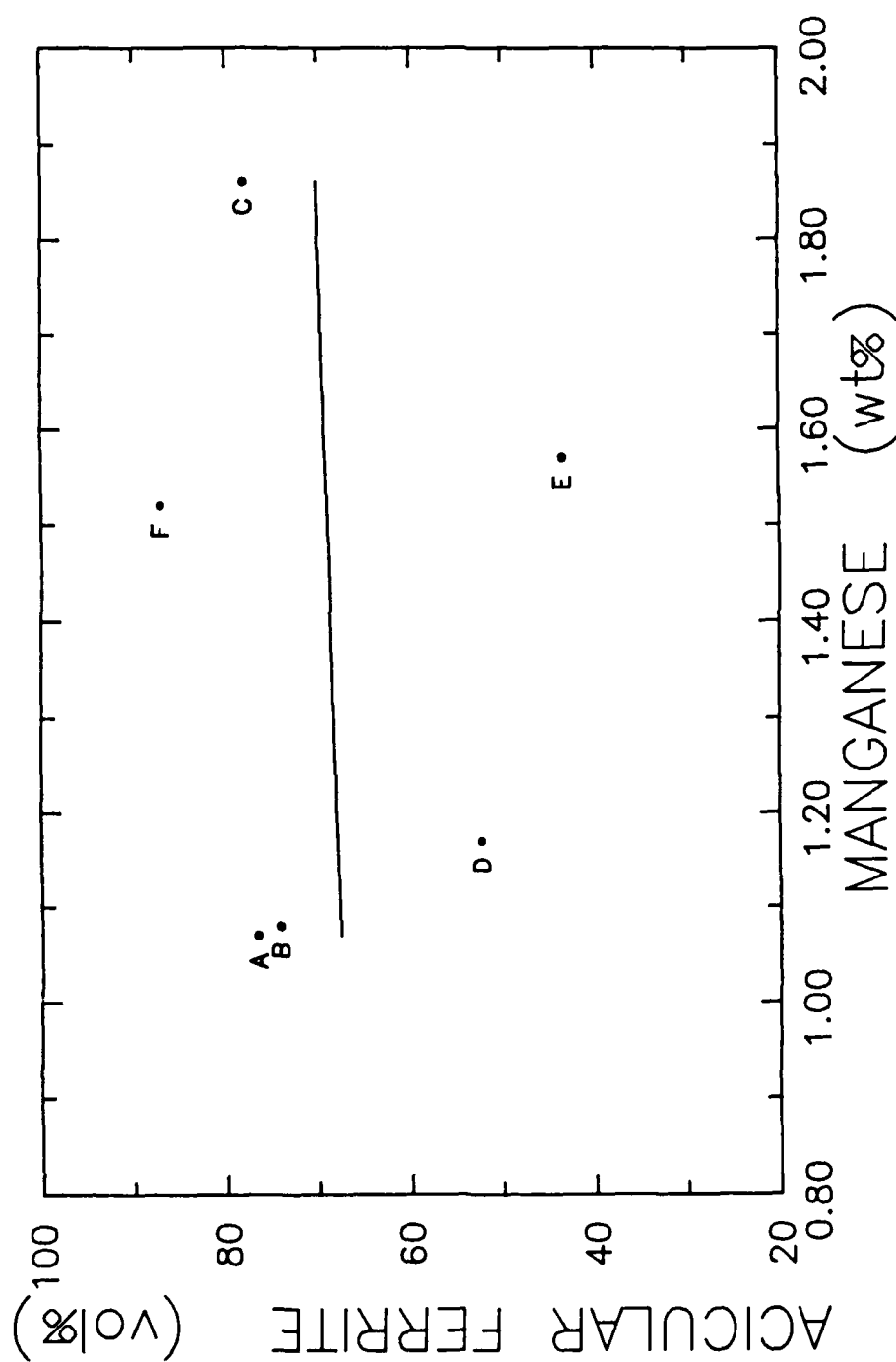


Figure 31. Manganese versus weld metal acicular ferrite. ($r^2=0.01$)

3.2.2 Manganese Effects

Based on previous work, manganese was expected to increase the fraction of acicular ferrite; however, as shown in figure 31, there was little correlation between manganese and acicular ferrite. Manganese is recognized as a ferrite hardener and is generally beneficial when present in the weld metal.

The primary effect of manganese in this study was in the formation of the M-A constituent which will be discussed in section 3.2.3.

3.2.3 Martensite and Retained Austenite

The M-A constituent present in the weld metal was resolved using the etching process described in section 2.3.4 and then observed using the SEM. Ikawa *et al.* [10] showed that the volume fraction of M-A is dependent on the cooling rate for a given alloy system. The morphology at rapid cooling rates is rod-shaped and changes to large, blocky shapes as the cooling rate is decreased. As the cooling time increased above 20 seconds from 800 °C to 500 °C, Ikawa noted a sharp increase in the amount of M-A present in the microstructure.

Figures 32 through 37 show the M-A constituent present in each weld at a magnification of 2000X. This magnification was chosen to show the general distribution of the M-A islands (appearing as light areas) throughout the weldment microstructure.

Figures 38 through 43 depict the weld metal M-A constituent at a magnification of 5000X. Here the blocky shape of the M-A islands is evident. Figures 44 and 45 show the M-A constituent at a magnification of 10,000X which was the magnification used for quantitative metallography in determining the volume fraction of M-A present in each weldment. The results are listed in table 9.

Figures 46 and 47 are of several selected M-A islands showing the structure at a magnification of 25,000X.

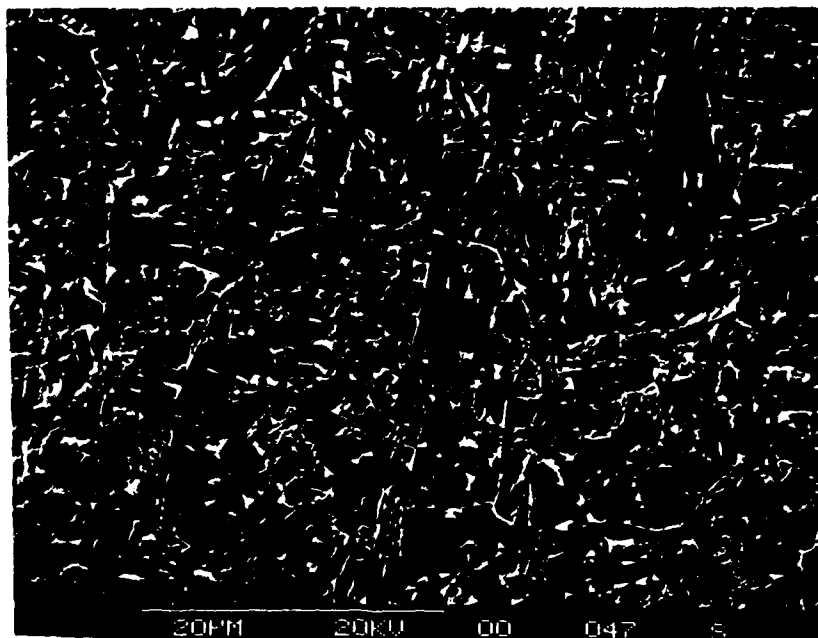


Figure 32. Weld A weld metal M-A constituent. 2000X.

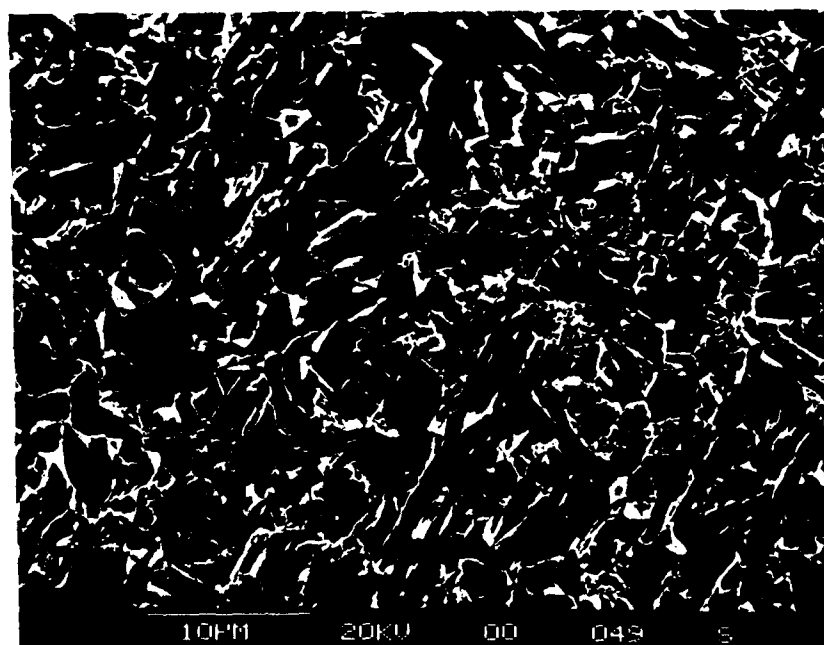


Figure 33. Weld B weld metal M-A constituent. 2000X.

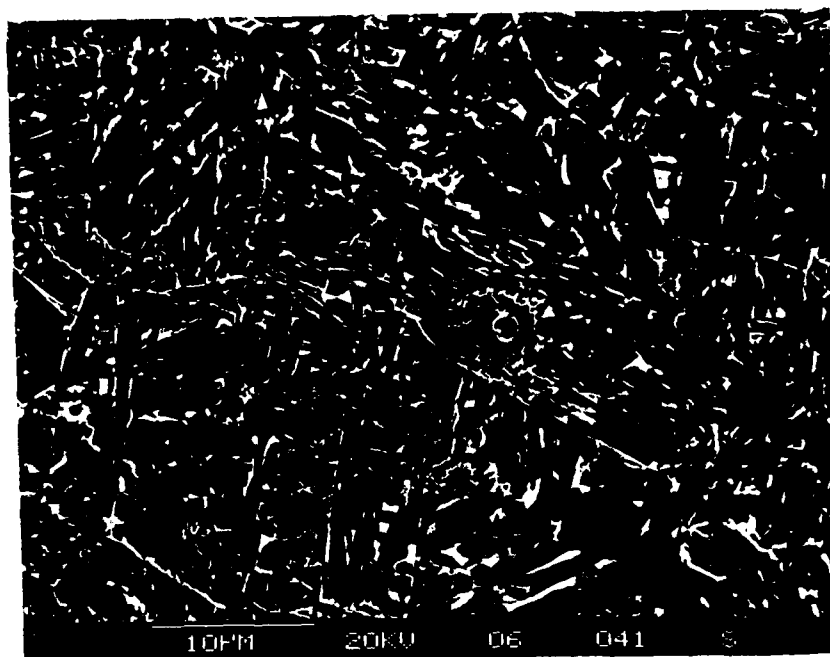


Figure 34. Weld C weld metal M-A constituent. 2000X.

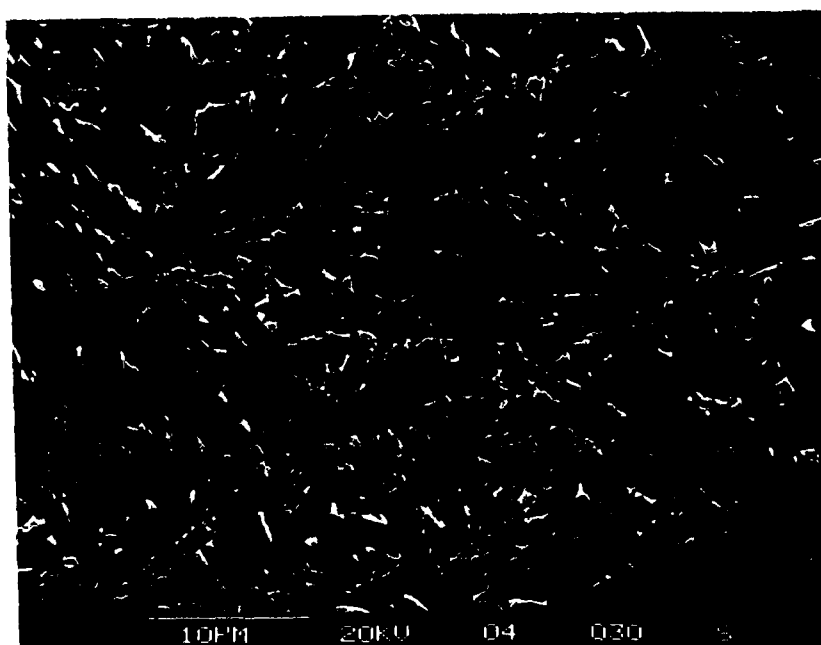


Figure 35. Weld D weld metal M-A constituent. 2000X.

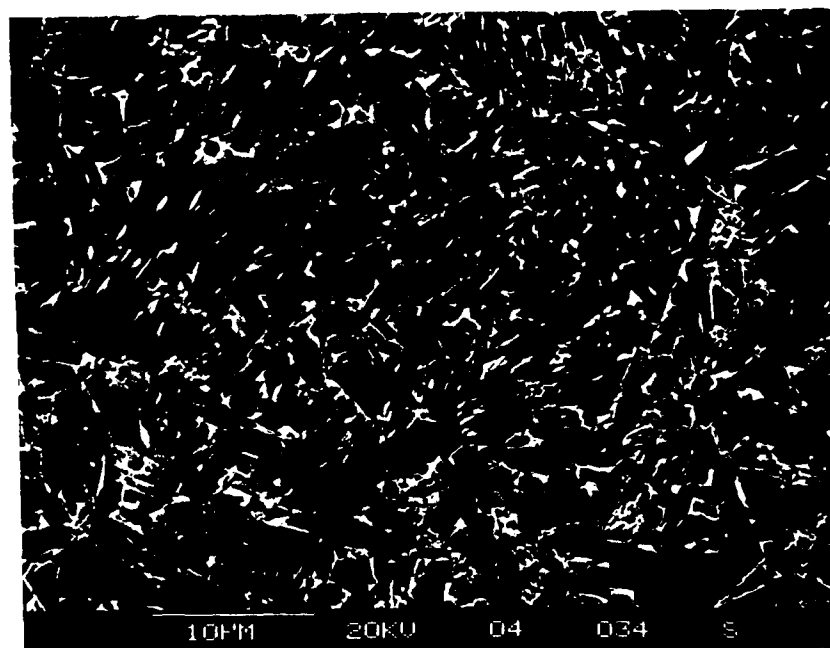


Figure 36. Weld E weld metal M-A constituent. 2000X.

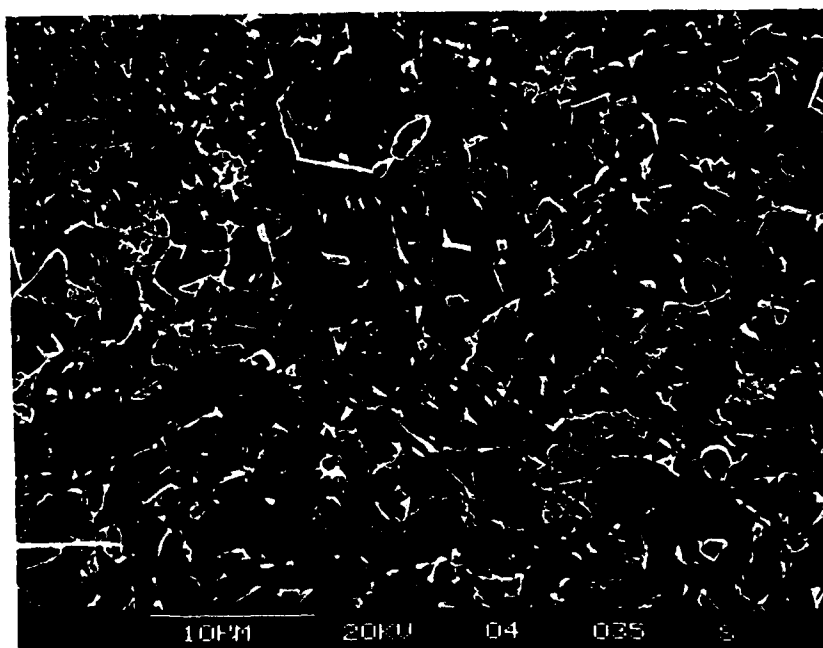


Figure 37. Weld F weld metal M-A constituent. 2000X.

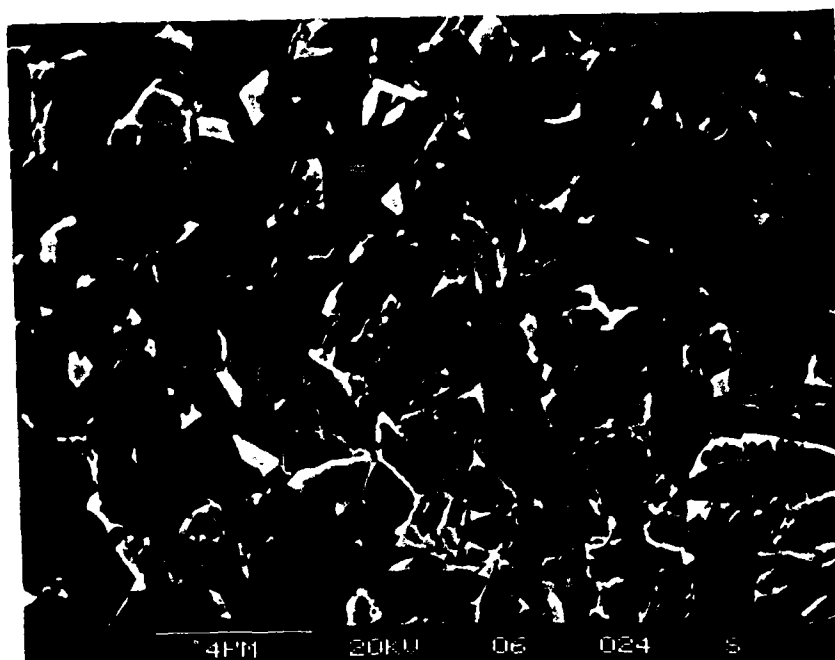


Figure 38. Weld A weld metal M-A constituent. 5000X.

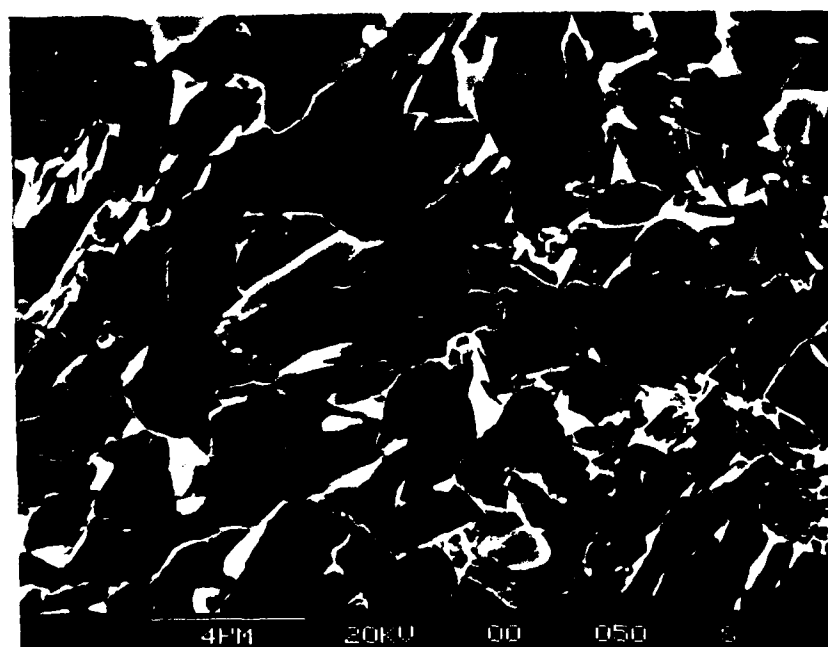


Figure 39. Weld B weld metal M-A constituent. 5000X.

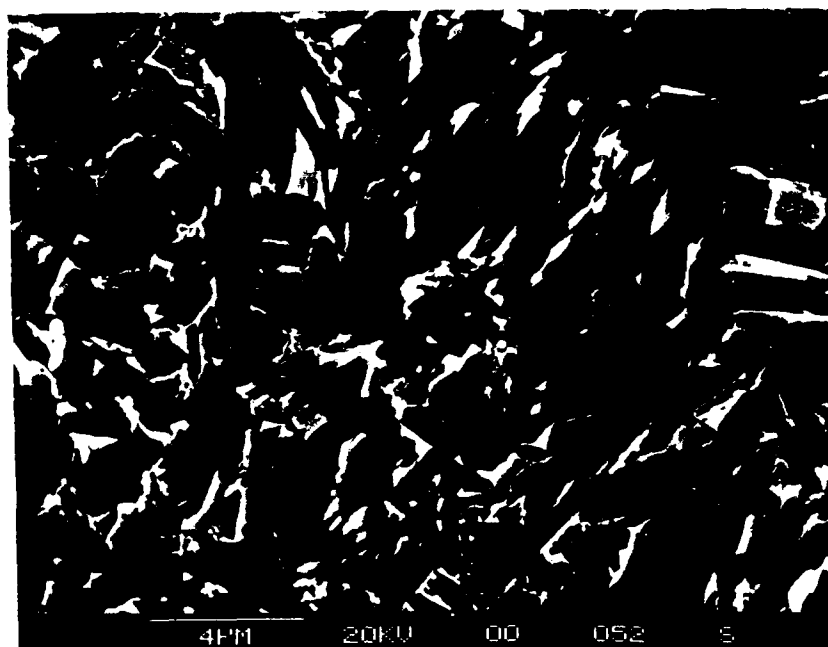


Figure 40. Weld C weld metal M-A constituent. 5000X.

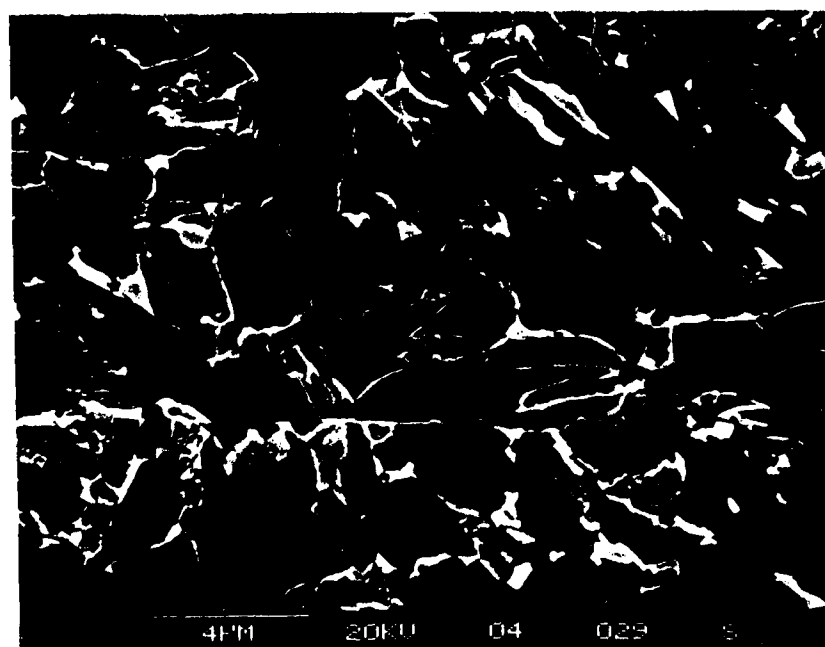


Figure 41. Weld D weld metal M-A constituent. 5000X.

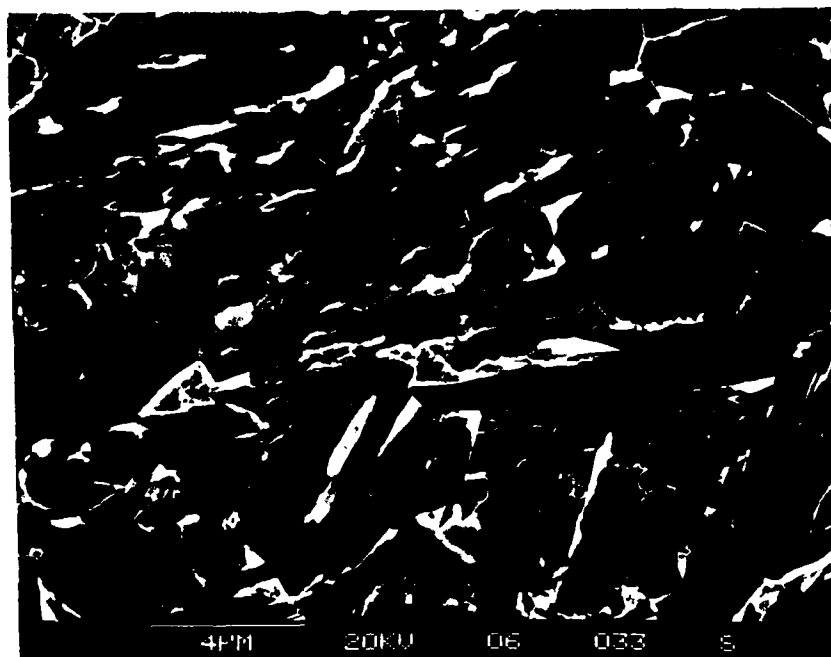


Figure 42. Weld E weld metal M-A constituent. 5000X.

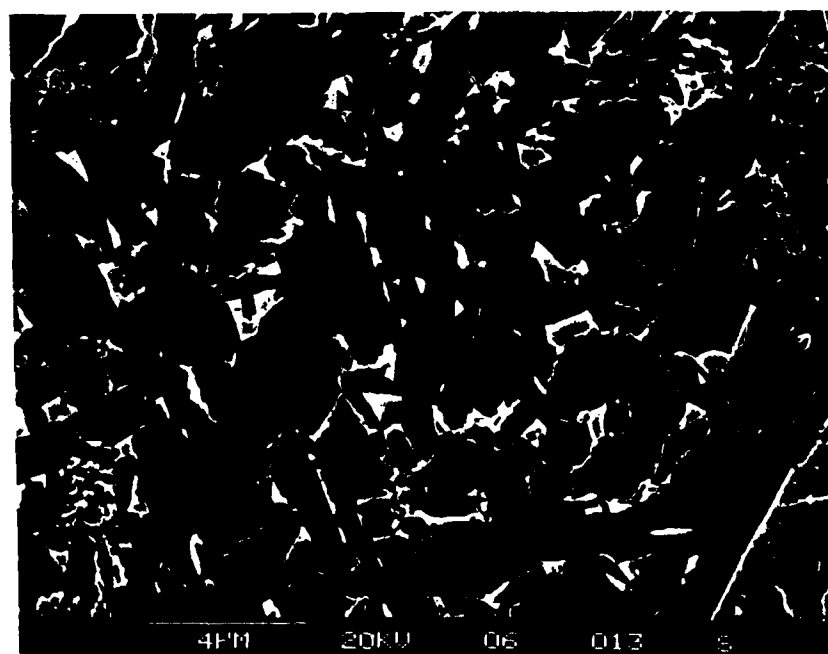


Figure 43. Weld F weld metal M-A constituent. 5000X.

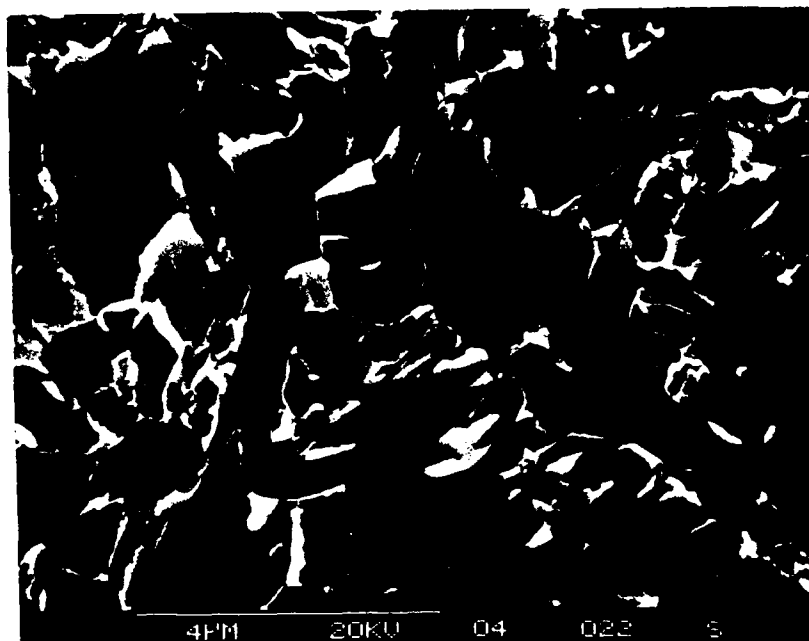


Figure 44. Weld F weld metal M-A constituent. 10,000X.

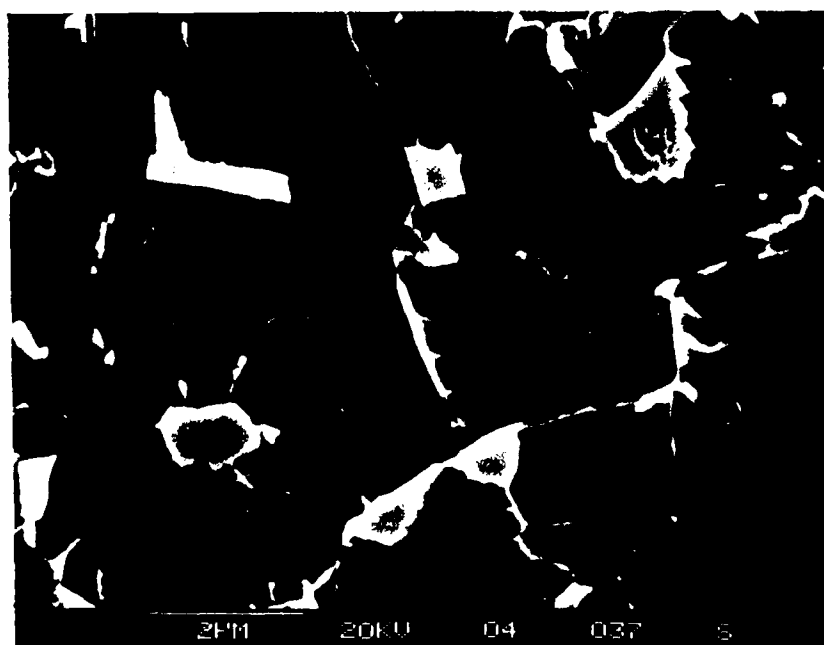


Figure 45. Weld A weld metal M-A constituent. 10,000X.



Figure 46. Weld A weld metal M-A constituent. 25,000X.

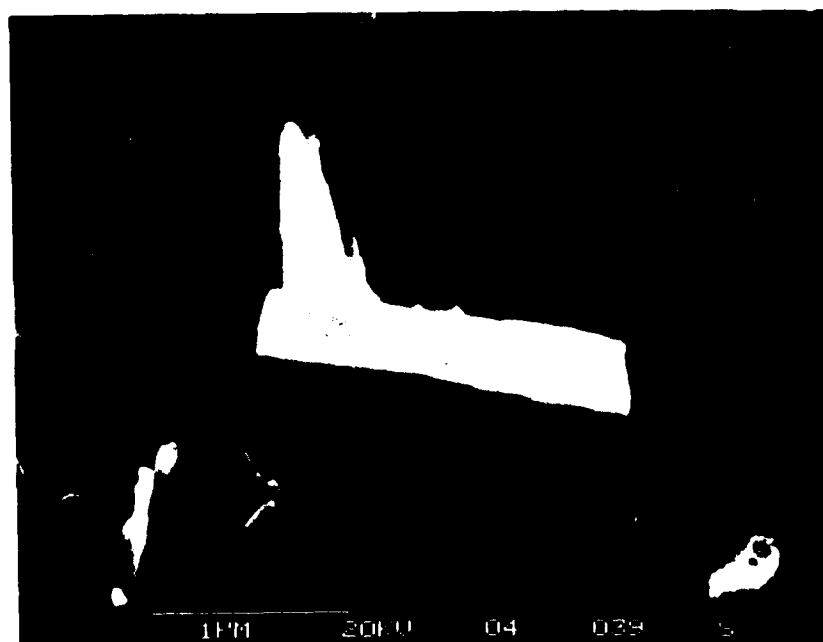


Figure 47. Weld F weld metal M-A constituent. 25,000X.

The formation of the M-A occurs as a result of the $\gamma \rightarrow \alpha$ transformation when carbon is rejected from the growing primary and acicular ferrite. The carbon content of this remaining austenite is

$$wt\%C = \frac{wt\%C}{\text{volume fraction austenite remaining}} \quad (12)$$

The fraction of remaining austenite is estimated to be on the order of 5% in this case based on the work of Speich and Scoonover [44]. From this estimate, the untransformed austenite contains $0.037/0.05 = 0.74$ wt% carbon, where 0.037 wt% is an average value of the carbon content of the six welds.

This remaining carbon rich austenite does not transform until much lower temperatures with the transformation being incomplete at room temperature. The temperature marking the onset of the martensite transformation, M_s , in these carbon rich areas may be estimated by the following equation [45]

$$M_s(^{\circ}C) = 539 - 423C - 30.4Mn - 12.1Cr - 17.7Ni - 7.5Mo \quad (13)$$

Substituting the values from weld A, the M_s temperature was computed to be 133 $^{\circ}C$ while the martensite finish temperature, M_f , was below room temperature.

An estimate of the volume fraction of M-A that will result may be made using the Fe-C equilibrium diagram. At 738 $^{\circ}C$ with 0.68 wt% carbon in the remaining austenite, the fraction of M-A is

$$\frac{0.037}{0.68} \times 100 = 5.4\% \quad (14)$$

This is a theoretical value for the fraction of M-A present which may vary depending on the alloy system. However, this demonstrates the need to reduce the carbon content if the volume fraction of M-A is to be reduced.

As described in section 1.3.1, Coldren [11] proposed that the combined effect of manganese and silicon is important in the formation of the M-A constituent. Examination of Coldren's data shows that only manganese and silicon were varied in the study while the remaining alloy composition was constant. Here the hardenability, P_{cm} , could have been plotted versus M-A yielding a similar graph. It is believed that it is the hardenability which influences the formation of M-A, not just manganese and silicon, and so the relationship to consider is that of P_{cm} and M-A fraction. Figure 48 shows increasing M-A volume fraction with increasing P_{cm} .

Element	Diffusivity cm ² /sec	x μm	Temperature ³ °K
Carbon	1.5x10 ⁻⁸	9.10	1073
Manganese	7.1x10 ⁻¹³	0.06	1273
Silicon	1.4x10 ⁻¹¹	0.28	1073

Table 11. Diffusivity of C, Mn, and Si during $\gamma \rightarrow \alpha$ transformation.

In considering the alloy system during the $\gamma \rightarrow \alpha$ transformation, it is the carbon which has the greatest effect due to its diffusivity. Table 11 shows the relative diffusivity of carbon, manganese, and silicon with the associated calculations described in appendix C.

³ Temperature at which data presented in Metals Reference Book, Butterworths, 1976

From the data in table 11 it is clear that carbon may diffuse easily from the ferrite during the $\gamma \rightarrow \alpha$ transformation as compared to the other elements. The mechanism by which the formation of M-A is influenced by elements other than carbon was not investigated further in this study and remains as future work.

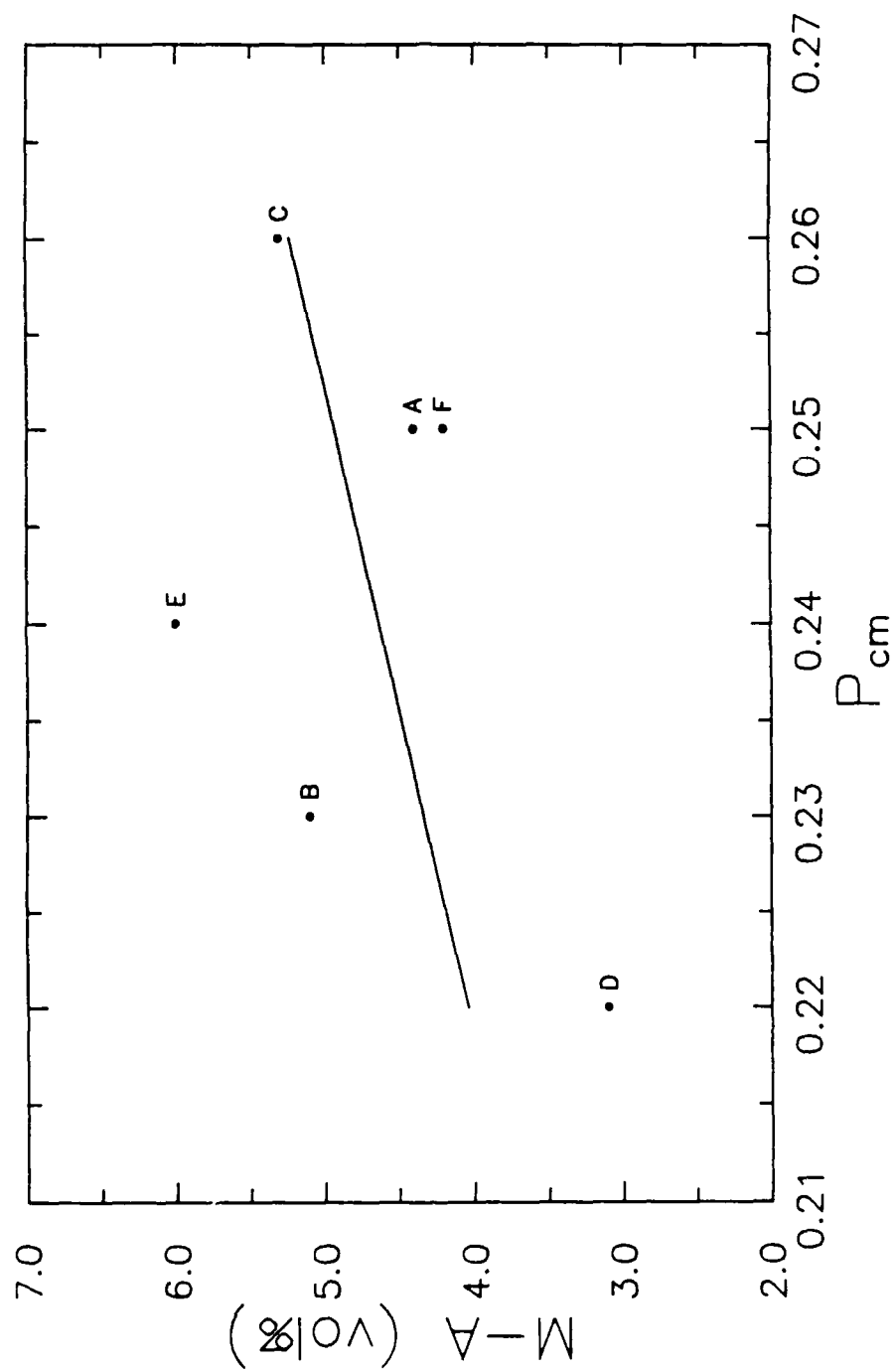
In summary carbon is an important consideration in controlling the formation of the M-A constituent and should be kept as low as possible to limit the volume fraction of M-A. To a lesser degree, the other elements present may increase the M-A fraction beyond that due to carbon. Finally, the detrimental effect of M-A on the mechanical properties will be discussed in section 3.3.

3.2.4 Other Effects

Comparison of the microstructures of the six welds, particularly welds E and F, reveal significant differences. These differences were also evident in the mechanical property test data which is presented in section 3.3. Welds E and F were to have been identical since these were the center points of the matrix proposed in chapter two. Welding conditions, base plate, and consumables were the same. However, as seen in figure 21, the microstructure of weld E exhibits veining and very poor mechanical properties.

The correlation between the boron content and fraction of acicular ferrite is shown in figure 49. As described in section 1.3.3, the boron suppresses the nucleation of primary ferrite at the prior austenite grain boundaries and thereby promotes the formation of acicular ferrite. The trend seen in the six welds of this study would suggest that this is a possible mechanism to explain the reduction in acicular ferrite, particularly in weld E.

Based on the data from this study, the boron level should be greater than 0.002 wt%. The largest amount of boron was in weld B with 0.005 wt% which exhibited good mechanical properties.

Figure 48. P_{cm} versus M-A volume fraction.

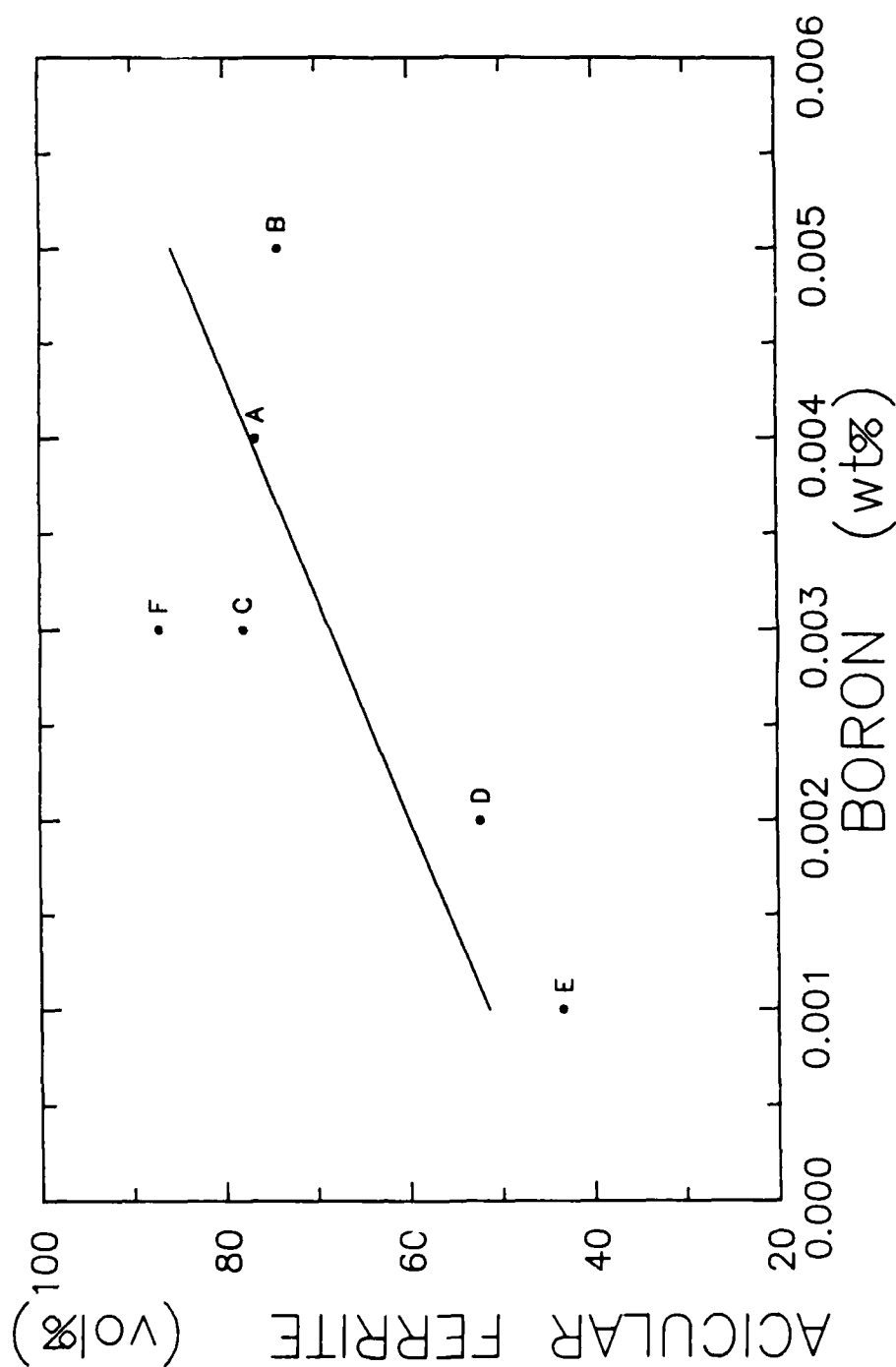


Figure 49. Boron content versus acicular ferrite fraction. ($r^2=0.52$)

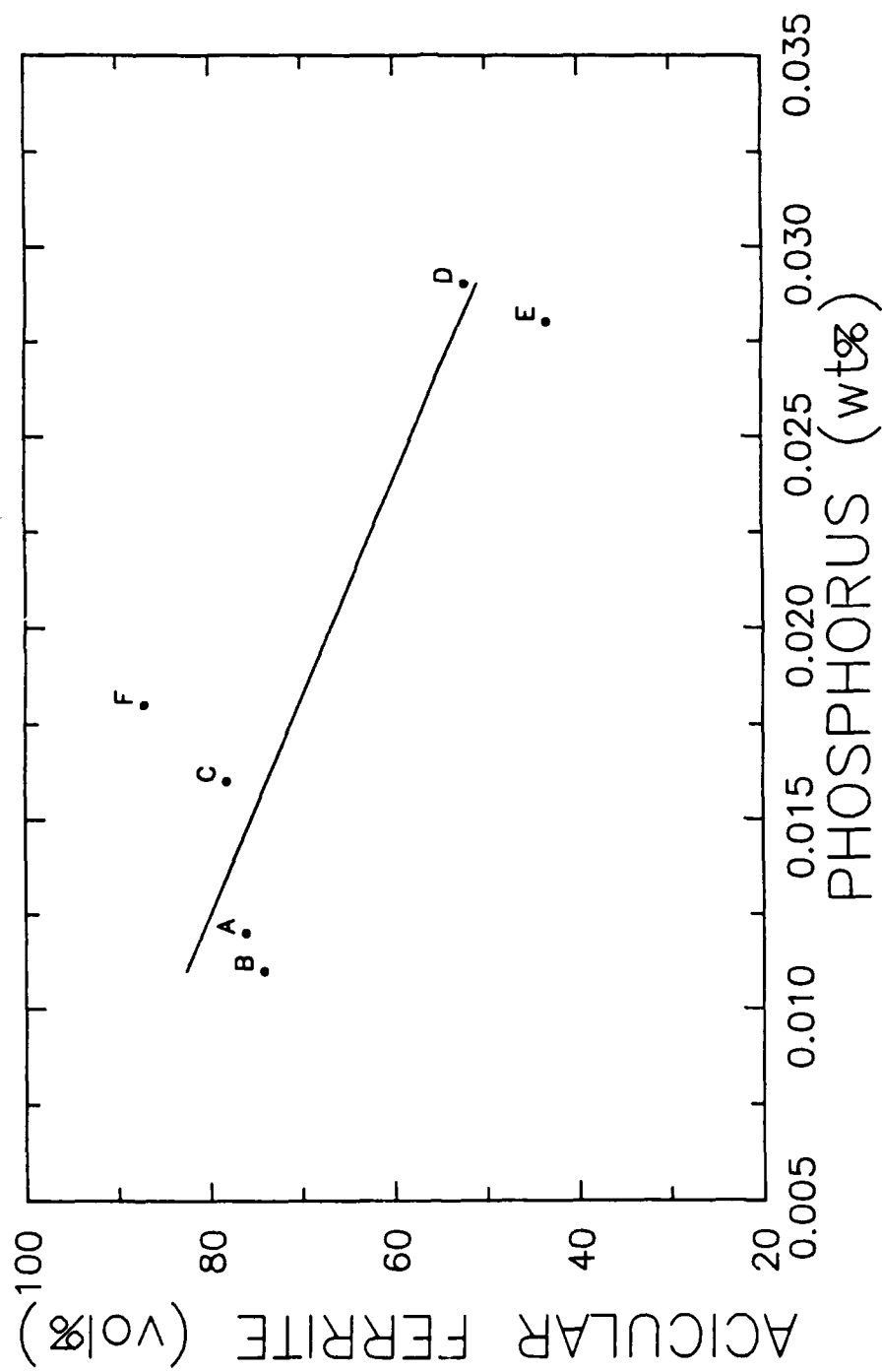


Figure 50. Phosphorus content versus acicular ferrite fraction. ($r^2=0.66$)

	Boron (Analysis 1) wt%	Boron (Analysis 2) wt%	Phosphorus (Analysis 1) wt%	Phosphorus (Analysis 2) wt%	Acicular Ferrite %
A	0.004	0.003	0.012	0.020	76.2
B	0.005	0.003	0.011	0.020	74.2
C	0.003	0.002	0.016	0.020	78.0
D	0.002	<0.001	0.029	0.032	52.3
E	0.001	<0.001	0.028	0.027	43.4
F	0.003	0.002	0.018	0.024	87.1

Table 12. Chemical check analysis for boron and phosphorus.

In addition to the differences in boron content, an increase in phosphorus content was noted in welds D and E which had the lowest fraction of acicular ferrite. As a check a second chemical analysis for boron was conducted with the results shown in table 12. Also shown for reference in table 12 is the volume fraction of acicular ferrite in each weld. Figure 50 shows a trend of decreasing acicular ferrite fraction with increasing phosphorus content. This trend and the source of the phosphorus could not be explained in this study, however, these results suggest a very strong effect of phosphorus on the amount of acicular ferrite. This should be investigated in future work.

3.3 Mechanical Properties

Tables 13 and 14 summarize the mechanical property data collected from the tensile and Charpy specimen testing of the weld metal. Appendix D contains individual graphs of the Charpy data for each weld.

	TENSILE			CHARPY						
	0.2% Yield ksi	UTS ksi	Elonga- tion %	-180 °F ft-lb	-120 °F ft-lb	-60 °F ft-lb	0 °F ft-lb	60 °F ft-lb	120 °F ft-lb	180 °F ft-lb
A	98	113	24	13	25	46	64	75	73	74
B	93	108	22	7	15	36	59	70	73	75
C	99	117	21	10	16	33	51	53	56	59
D	90	106	23	7	12	49	63	69	72	71
E	98	114	22	11	11	30	39	64	64	77
F	96	110	8	9	24	41	69	69	65	66

Table 13. Mechanical property data summary.

	CHARPY						
	-180 °F % shear	-120 °F % shear	-60 °F % shear	0 °F % shear	60 °F % shear	120 °F % shear	180 °F % shear
A	10	35	60	85	95	98	100
B	10	25	45	80	83	95	100
C	10	25	40	70	85	100	95
D	10	13	50	80	92	97	100
E	10	25	30	50	88	95	100
F	10	30	57	80	98	97	100

Table 14. Mechanical property data summary continued.

Analysis of the impact data presented in tables 13 and 14 indicated that there is a strong correlation between the volume fraction of M-A present in the weld metal and the Charpy energies recorded. Figure 51 shows the relation between the volume fraction of M-A and the FATT as determined by taking the temperature corresponding to 50% shear. The correlation factor, $r^2=0.57$, shows a correlation between increasing M-A fraction and increasing transition temperature. Figure 52 demonstrates the relation between M-A and the Charpy impact energy at 0 °F. Here the correlation factor, $r^2=0.67$, demonstrates the detrimental effect of the M-A on fracture toughness. Finally, figure 53 showing M-A versus Charpy energy at -60 °F with $r^2=0.89$ further supports the fact that M-A will be detrimental to mechanical properties at low temperatures. In each case it is evident that as the M-A fraction increases, the Charpy energy can be expected to decrease. The question then becomes, what is the mechanism of fracture involving the M-A constituent?

Figure 54 is a macro photograph showing the Charpy fracture surface at approximately 9X which was used in the following discussion. Examination of the matrix below the Charpy fracture surface was possible after sectioning as described in section 2.3.5. This weld metal from weldment C, fractured at -180 °F, was chosen for examination. Figure 55 shows one of the sub cracks in which the fracture path followed the outside of the M-A particle, a behavior which was typical of all low temperature cleavage fracture areas. The Charpy impact surface showed cleavage regions with small ductile areas exhibiting dimples. Since cleavage was the primary fracture mode, these areas were closely examined. Chen *et al.* [9] observed identical behavior in the HAZ of HSLA-80 steel.

Figure 56 depicts the fracture surface and shows a M-A block as a crack origin with river patterns indicating the crack initiation site. Figure 57 is a second example of a M-A block acting as a crack initiation site. In each case the M-A particle is indicated with an arrow. The mechanism by which the M-A phase becomes a crack initiator is explained in the following paragraphs.

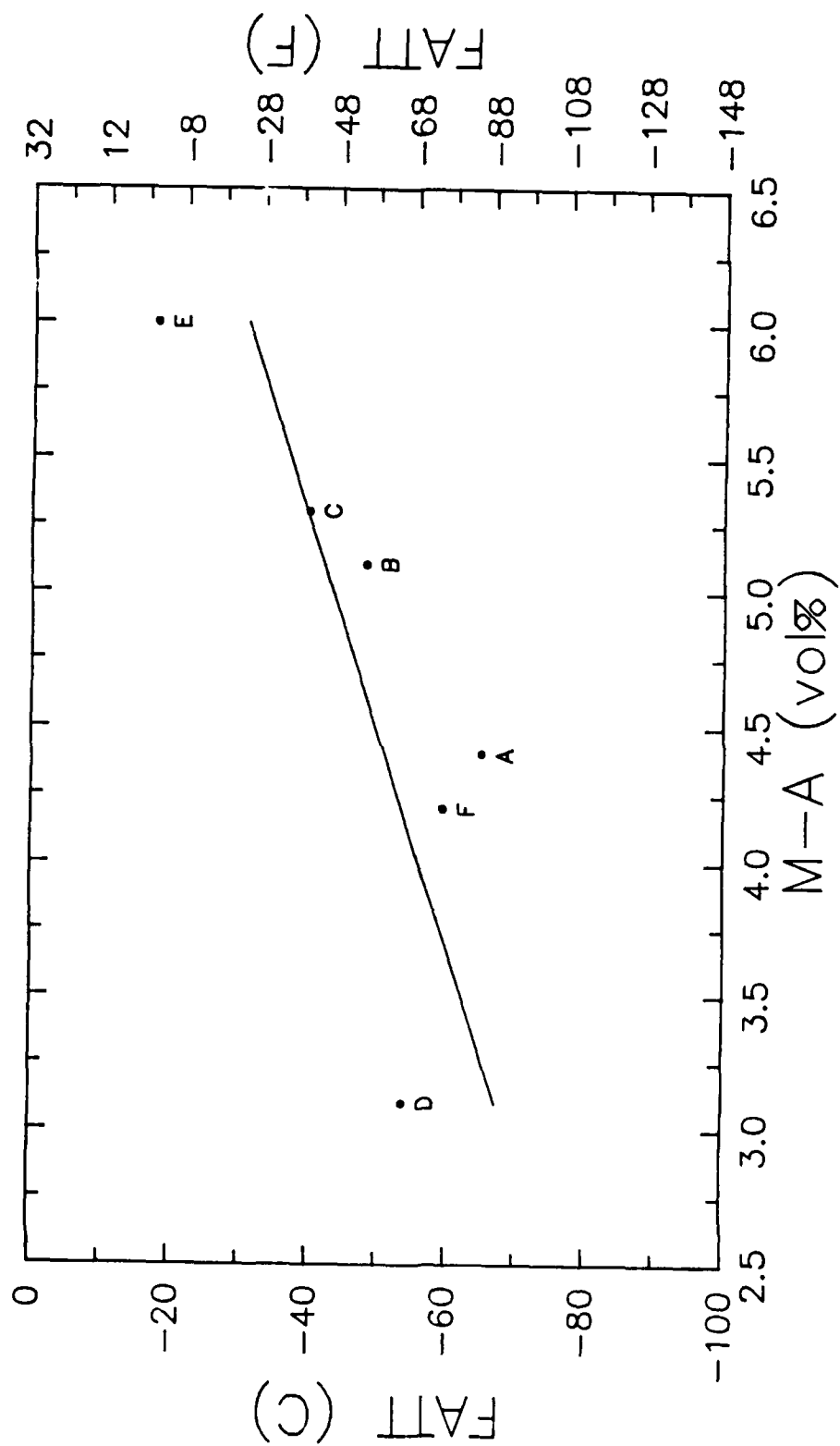


Figure 51. M-A fraction versus transition temperature based on 50% shear. ($r^2=0.57$)

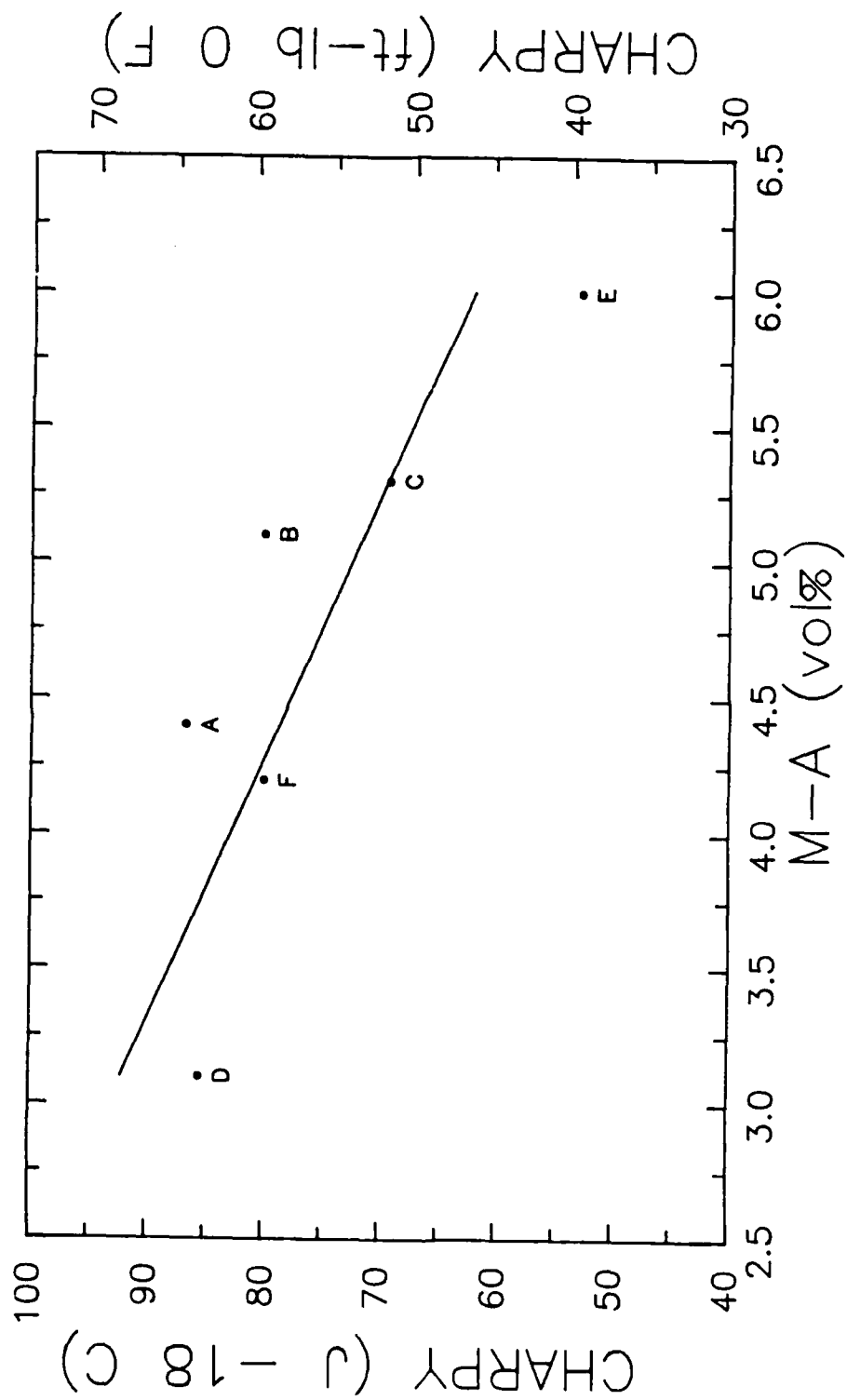


Figure 52. M-A fraction versus Charpy energy at 0 °F. ($r^2=0.67$)

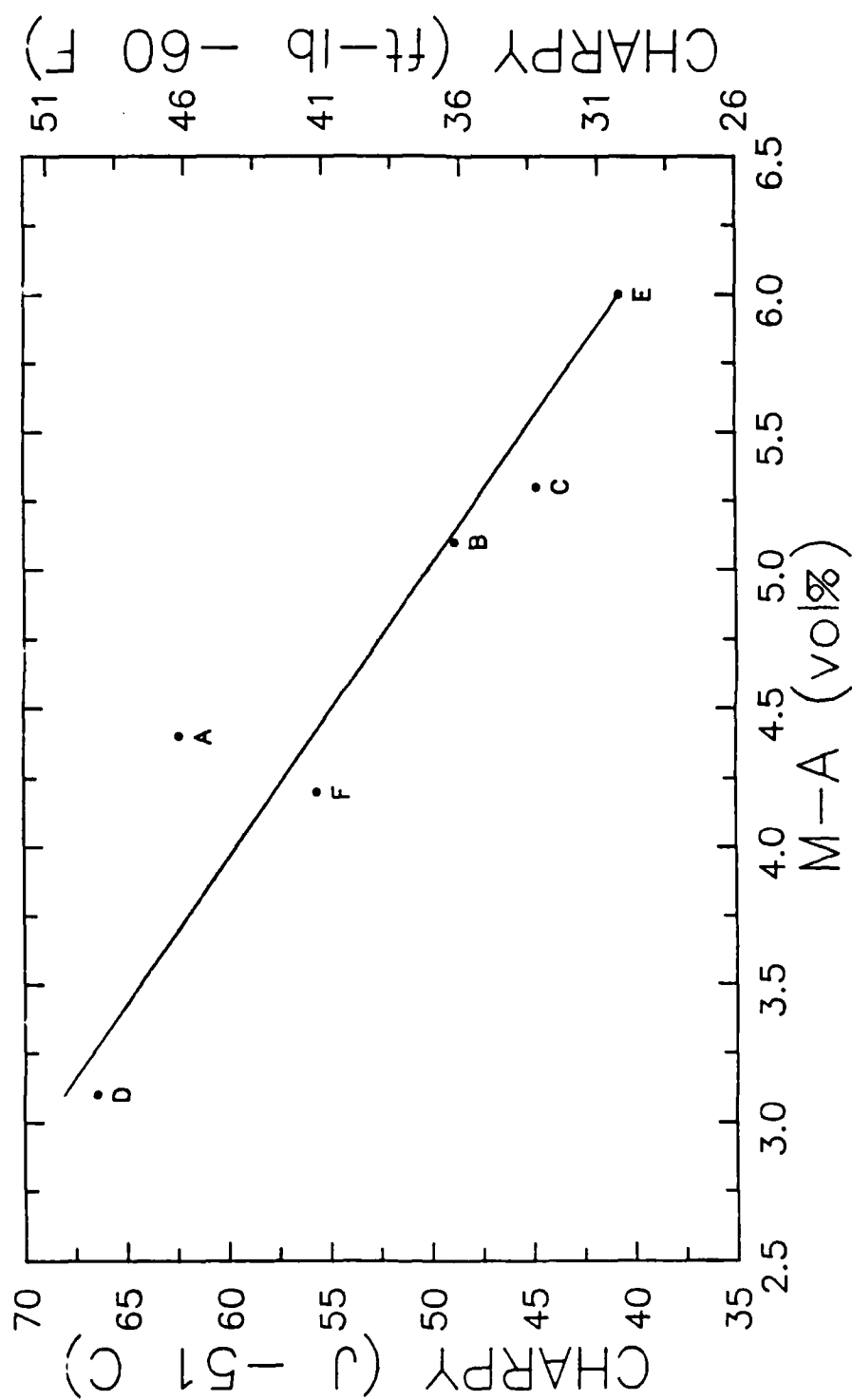


Figure 53. M-A fraction versus Charpy energy at -60 °F. ($r^2 = 0.89$)

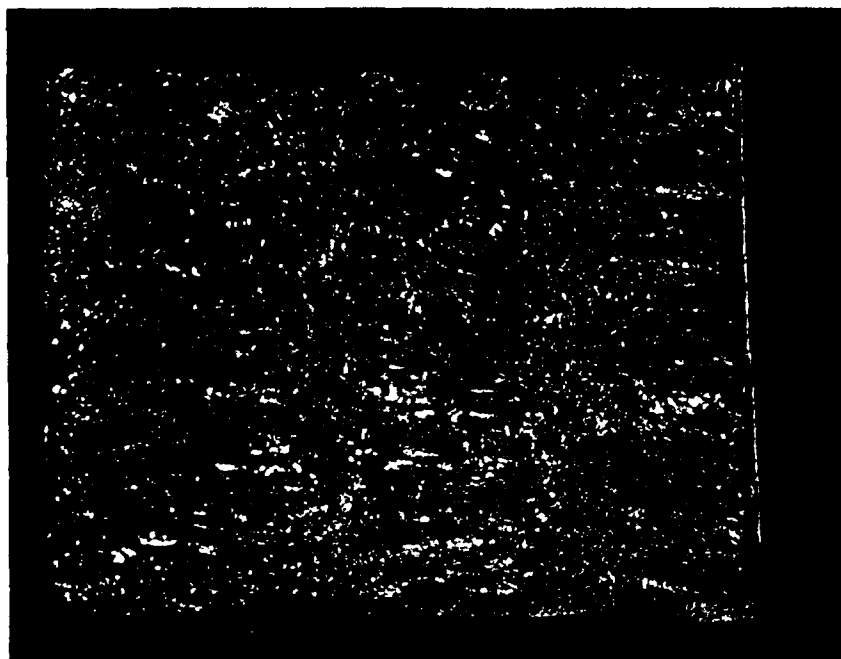


Figure 54. Charpy fracture surface, Weld C, -180 °F.

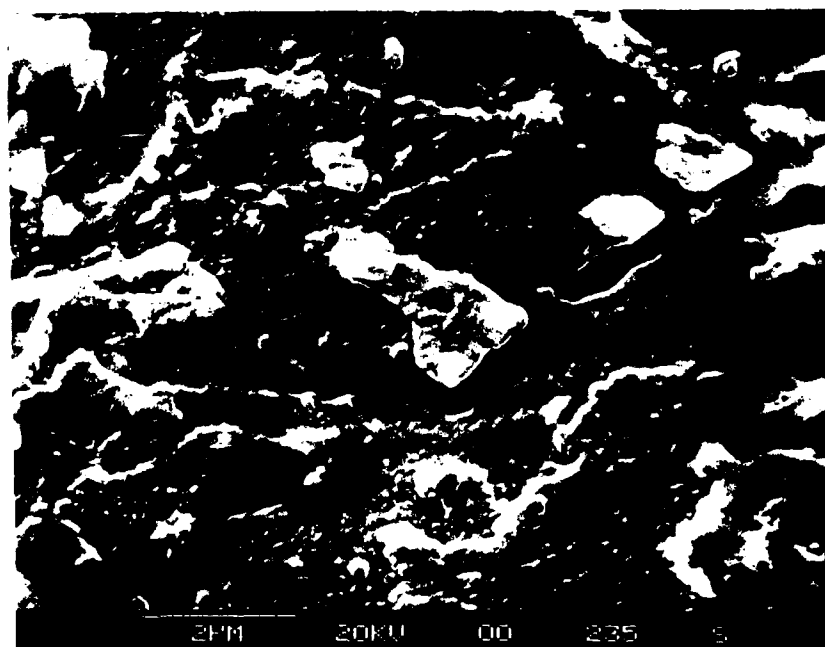


Figure 55. Charpy impact specimen sub crack showing fracture around M-A particle.

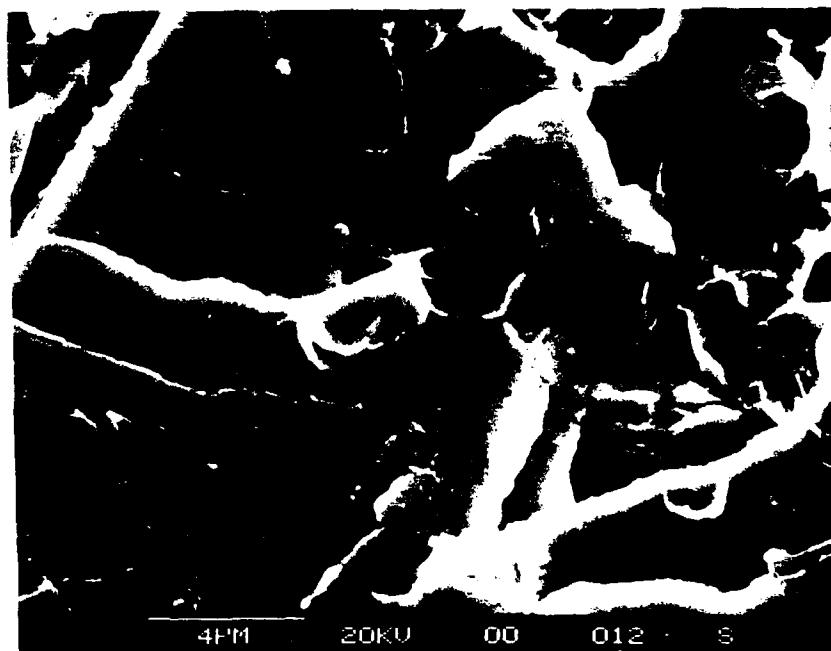


Figure 56. Charpy impact specimen fracture surface showing M-A initiation site.

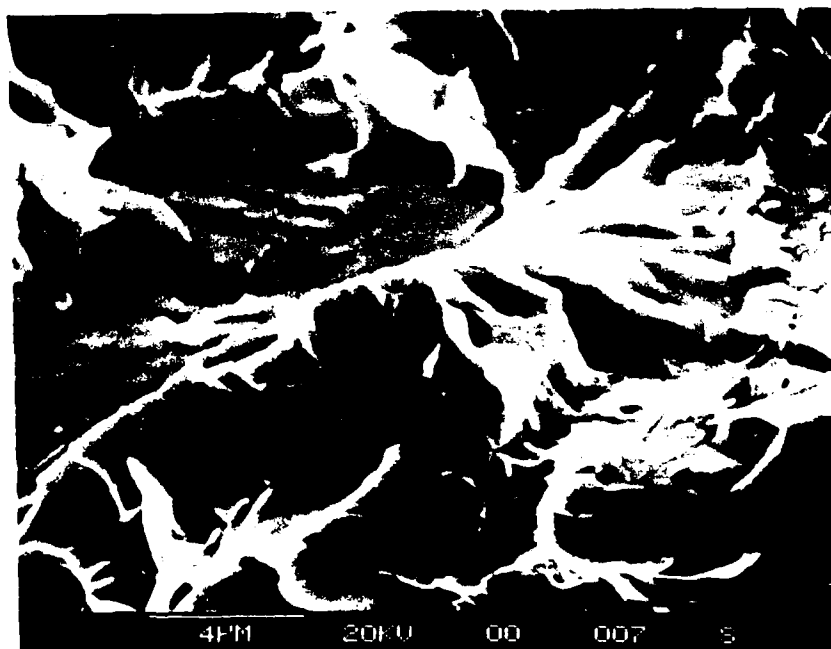


Figure 57. Charpy impact specimen fracture surface showing M-A initiation site.

These hard, sharp featured, M-A particles localize the strain as the metal matrix is loaded and so act as stress concentrators. As the stress level increases the high strength of the M-A block causes a triaxial stress concentration in the ferrite matrix near the M-A particle. At low temperature the ferrite cannot deform to relieve the stress and cleavage fracture occurs.

The fracture event involving cleavage then proceeds with the initiation and joining of microcracks in the region of stress concentration moving ahead of the major fracture.

Taking the average length of the M-A blocks to be 1.5 μm in the direction of crack propagation, the critical stress may be estimated by Griffith's criterion

$$\sigma_c = \sqrt{\frac{2E\gamma_p}{\pi c}} \quad (15)$$

where

$$E = \text{Young's modulus} \left(210 \frac{\text{GN}}{\text{m}^2} \right)$$

$$\gamma_p = \text{effective surface energy of crack} \left(11.2 \frac{\text{J}}{\text{m}^2} \right)$$

$$2c = \text{defect length} (2\mu\text{m})$$

The value of γ_p was taken from data reported by Chen *et al.* [9] for HSLA steel.

From equation (15), $\sigma_c = 1000 \text{ MPa}$ (145 ksi) when $2c = 3.0 \mu\text{m}$.

The critical stress, σ_c , is then controlled by the defect size. As the size of the M-A particles increase, this critical stress is reduced with a net reduction in the observed Charpy energy. Or stated differently, the larger the M-A particles, the smaller the load to create new initiation sites.

In summary the controlling factor in low temperature Charpy crack propagation is the size and population of the M-A particles present in the weld metal matrix. Any effort to improve the weld metal toughness must include a reduction in the size and volume of the M-A phase through alloying and/or controlling the cooling rate.

CHAPTER 4

4.1 Conclusions

The results of this investigation on as deposited weld metal which contained systematic variations of titanium and manganese led to the following conclusions.

- a. The number of nonmetallic oxide inclusions per unit volume and the inclusion size distribution were controlled by the titanium bearing, faceted particles found within the spherical inclusions.
- b. The titanium content in the weld metal should be kept to the lowest possible level consistent with protecting the available boron from nitrogen.
- c. The martensite and retained austenite can be revealed using an electrolytic etching technique and scanning electron microscopy. The formation of this M-A constituent is controlled primarily by the carbon present in the weld metal with a secondary effect from the manganese and silicon present.
- d. There is a strong correlation between the Charpy V-notch energy at low temperatures and the volume fraction of martensite and retained austenite with the M-A constituent providing crack initiation sites during fracture.
- e. The reduction in acicular ferrite fraction and the poor mechanical properties in welds D and E may be due to low boron and high phosphorus contents, although the exact cause could not be determined in this study.

4.2 Future Work

Based on the observations during this investigation, recommendations for future work center around the formation of the M-A constituent and its role in low temperature fracture. The following paragraphs describe the possible direction of that work.

The formation of M-A could be better understood by designing an experiment where number of weld metal samples are produced, all of identical chemical composition. These samples would then be re-heated and then quenched over a range of cooling rates to quantify the changes in M-A shape and size due to changes in cooling rate. These cooling rates should be consistent with those expected from high deposition rate SAW.

Next, a series of very low carbon welds should be made, varying only the manganese content. Again the interest would be in the change between welds in the M-A morphology and distribution.

Finally, Charpy V-notch specimens should be tested from the above welds and then examined carefully to determine the mechanism by which crack initiation occurs due to the presence of M-A.

REFERENCES

1. Cary, H. E., *Modern Welding Technology*, Prentice-Hall, Inc., 1979.
2. Houldcroft, P. T., *Welding Process Technology*, Cambridge University Press, 1977.
3. Garland, J. G. and Kirkwood, P. R., *Towards Improved Submerged Arc Weld Metal*, Metal Construction, May 1975, p. 275-283 and June 1975, p. 320-330.
4. Levine, E. and Hill, D. C., *Structure-Property Relationships in Low C Weld Metal*, Metallurgical Transactions, September 1977, p. 1453-1463.
5. Choi, C. L. and Hill, D. C., *A Study of Microstructural Progression in As-Deposited Weld Metal*, Welding Journal, August 1978, p.232s-236s.
6. Liu, S. and Olson, S. L., *The Role of Inclusions in Controlling HSLA Steel Weld Microstructures*, Welding Journal, June 1986, p. 139s-149s.
7. Suzuki, H., *Carbon Equivalent and Maximum Hardness*, Trans. Japan Welding Society, April 1984, p. 25-33.
8. Masubuchi, K., *Analysis of Welded Structures*, Pergamon Press, 1980.
9. Deb, P., Challenger, K. D., and Therrien, A. E., *Structure-Property Correlation of Submerged -Arc and Gas-Metal-Arc Weldments in HY-100 Steel*, Metallurgical Transactions, June 1987, p. 987-999.
10. Chen, J. H., Kikuta, Y., Araki, M., Yoneda, M., and Matsuda, Y., *Micro-Fracture Behavior Induced by M-A Constituent (Island Martensite) in Simulated Welding Heat*

Affected Zone of HT80 High Strength Low Alloyed Steel, Acta Metallurgica, October 1984, p. 1779-1788.

11. Ikawa, H., Oshige, H., and Tanoue, T., *Effect of Martensite-Austenite Constituent on HAZ Toughness of a High Strength Steel*, Trans. Japan Welding Society, October 1980, p. 3-12.

12. Coldren, A. P. and Oakwood, T. G., *A New Economical X-70 Linepipe Steel*, Journal of Metals, April 1983, p. 28-33.

13. Chen, B., private communication, 1989.

14. Farrar, R. A. and Watson, M. N., *Effects of Oxygen and Manganese on SA Weld Metal Microstructure*, Metal Construction, June 1979, p. 285-286.

15. Pargeter, R. J., *Acicular Ferrite and Inclusions in C-Mn Steel Weld Metals*, The Welding Institute Research Bulletin, July 1983, p. 215-220.

16. Mori, N., Homma, H., Okita, S., and Wakabayshi, S., *The Behavior of B and N in Notch Toughness Improvement of Ti-B Bearing Weld Metals*, IIW Doc. IX-1158-80, 1980.

17. Terashima, H., N. Nishiayama, and J. Tsuboi, *Effects of Ti, Al, and N on Toughness in 60 kg/mm² Class Submerged-Arc Weld Metal*, Proceedings, Annual Assembly of the Japanese Welding Society 80-81, 1981.

18. Mori, N., Homma, H., Okita, S., and Wakabayashi, M., *Mechanism of Notch Toughness Improvement in Ti-B Bearing Weld Metals*, International Institute of Welding, IIW Doc. IX-1196-81, 1981.

19. Masumoto, I., *Effects of Micro-Alloying Elements on Toughness of Steel Weld Metal*, IIW Doc. XII-F-38-79, 1979.
20. Tuliani, S. S., Boniszewski, T., and Eaton, N. F., *Notch Toughness of Commercial Submerged-Arc Weld Metal*, *Welding and Metal Fabrication*, August 1969, p. 327.
21. Eagar, T. W., *Sources of Weld metal Oxygen contamination During Submerged Arc Welding*, *Welding Journal*, March 1980, p. 76s-80s.
22. Dallam, C. B., Liu, S., and Olson, D. L., *Flux Composition Dependence of Microstructure and Toughness of Submerged Arc HSLA Weldments*, *Welding Journal*, May 1985, p. 140s-151s.
23. Keville, B. R., *Preliminary Observations of the Type, Shape and Distribution of Inclusions Found in Submerged Arc Weldments*, *Welding Journal*, September 1983, p. 253s-260s.
24. Bhatti, A. R., Saggese, M. E., Hawkins, D. N., Whiteman, J. A., and Golding, M. S., *Analysis of Inclusions in Submerged Arc Welds in Microalloyed Steels*, *Welding Journal*, July 1984, p. 224s-230s.
25. Ricks, R. A., G. S. Barritte, and Howell, P. R., *Influence of Second Phase Particles on Diffusional Transformations in Steels*, Solid \rightarrow Solid Phase Transformations (conference Proceedings), eds. Aaronson, H. I. and C. M. Wayman, Metall. Society of AIME, Pittsburgh, 1981.
26. Easterling, K., *Introduction to the Physical Metallurgy of Welding*, Butterworths, 1983.
27. Jang, J., and Indacochea J. E., *Inclusion Effects on Submerged-Arc Weld Microstructure*, *Journal of Materials Science*, February 1978, p. 689-700.

28. Cochrane, R. C. and P. R. Kirkwood, *The Effect of oxygen on Weld Metal Microstructure*, The Welding Institute, England, 1978.
29. Garritte, G. S., Ricks, R. A., and Howell, P. R., *Application of STEM/EDS to Study of Microstructural Development in HSLA Steel Weld Metals*, Conference on Quantitative Microanalysis With High Spatial Resolution, Manchester, 1984.
30. Chai, C., *Slag-Metal Reactions During Flux Shielded Arc Welding*, MIT doctoral thesis, 1980.
31. Dube, C. A., Aaronson, H. I., and Mehl, R. E.: *Rev. Met.*, V. 55, 1958, p. 201.
32. Aaronson, H. I., *Decomposition of Austenite by Diffusional Processes*, AIME, Philadelphia, 1960, p. 389.
33. Cochrane, R. C.: British Steel Corporation Report No. T/PDM/462/1/77/C, V. 1, 1977, p. 462.
34. Widgey, D. J. and Davey, T. G.: IIW Doc. IIA-389-76, 1976.
35. Abson, D. J. and Dolby, R. E.: *Welding Institute Research Bulletin*, April 1980, p. 100.
36. Parageter, R. J.: IIW Doc. IX-J-37-80, 1980.
37. Watson, M. N., Harrison, P. L., and Farrar, R. A., *How Niobium Influences SA Mild Steel Weldments*, *Welding and Metal Fabrication*, March 1981, p. 161.
38. Levine, E. and Hill, D. C., *Toughness in HSLA Steel Weldments*, *Metal Construction*,

August 1977, p. 346-353

39. Abson, D. J., Dolby, R. E., and Hart, P. H. M., *The role of Non-Metallic Inclusions in Ferrite Nucleation in Carbon Steel Weldments*, Welding Research Bulletin, November 1978, p. 75.
40. Mori, N., Homma, H., Okita, S., and Wakabayashi, M., *Mechanism of Notch Toughness Improvement in Ti-B Bearing Weld Metals*, IIW Doc. IX-1196-81, May 1981.
41. Itoh and Nakanishi, *Study on Charpy Impact Properties of Welds (Report 1)*, Journal of the Japan Welding Society, September 1975, p. 728-733.
42. Itoh, Nakanishi, and Komizo, *Study on Microstructure and Toughness of the Weld Metal (2nd Report)*, Journal of the Japan Welding Society, February 1982, p. 111-118.
43. *Classification of Microstructures in Low C - Low Alloy Steel Weld Metal and Terminology*, committee of Welding Metallurgy of Japan Welding Society, IIW Report, IX-1282-83, 1983.
44. Speich, G. R. and Scoonover, T. M., *Continuous-Cooling-Transformation Behavior and Strength of HSLA-80 (A710) Steel Plates*, Processing. Microstructure and Properties of HSLA Steels, A. J. DeArdo, ed., AIME, 1988.
45. Krauss, G., *Principles of Heat Treatment of Steel*, AIME, 1980.

APPENDIX A

Confidence Limits for Chemical Testing

The following summarize the confidence limits for the weld metal chemical testing done by LUVAK, Inc.

ELEMENT	CONFIDENCE LIMIT ±(wt%) ⁴
Carbon	0.001
Manganese	0.02
Silicon	0.01
Phosphorus	0.002
Sulfur	0.001
Nickel	0.05
Molybdenum	0.01
Chromium	0.02
Vanadium	0.001
Aluminum	0.002
Titanium	0.002
Zirconium	0.001
Copper	0.002
Oxygen	0.001
Nitrogen	0.001
Boron	0.001
Hydrogen	0.0001

⁴ From LUVAK, Inc., Boylston, Massachusetts.

APPENDIX B

Etchant Summary

The following table summarizes the etchants used in this investigation.

ETCHANT	CONTENTS	COMMENTS
2% Nital	2 ml nitric acid 98 ml methanol	Reveals ferrite boundaries.
Winsteads	4 g picric acid 20 ml methanol 400 ml distilled water 2 g sodium tridecylbenzene sulfonate	Mix 100 ml Winsteads etchant with 1 ml HCl. Agitate sample ultrasonically for 30 seconds to resolve prior austenite grain boundaries
Ikawa Electrolytic [11] (two step)	1. 5 g EDTA, 0.5 g sodium fluoride, and 100 ml distilled water. 2. 5 g picric acid, 25 g sodium hydroxide, and 100 ml distilled water.	Etch at 6.5 V for 15 seconds using first electrolyte followed by 6 V for 30 seconds in the second electrolyte.

APPENDIX C

Diffusion Distances of C, Mn, and Si

The following summarize the calculations demonstrating relative diffusion distances for carbon, manganese, and silicon in weld metal.

First, the reduction in the $\gamma \rightarrow \alpha$ temperature due to each of the three elements was determined based on the amount of each element in weld A using appropriate equilibrium diagrams.

ΔT_c	14 °C
ΔT_{Mn}	20
ΔT_{Si}	~0

The starting temperature then becomes

$$T = 912 - \sum \Delta T \\ = 878^\circ\text{C}$$

The time for the transformation process was then calculated using a cooling rate of 11 °C/sec based on thermocouple plunges in the molten weld pool. The time considered for diffusion is

$$\begin{aligned} \text{time} &= \frac{T - 723}{\text{cooling rate}} \\ &= 14.1 \text{ sec} \end{aligned}$$

The diffusion distances were then determined from

$$D = D_0 e^{-\frac{Q}{RT}}$$

and

$$x = 2\sqrt{Dt}$$

where the variables and results are tabulated in the following table. In each case

$R = 1.98 \frac{\text{cal}}{\text{mol} \cdot ^\circ\text{K}}$ and $t = 14.1 \text{ sec}$.

Element	D_0 cm ² /sec	Q kcal/mole	T ⁵ °C	x μm
C	0.668	37.46	1073	9.0
Mn	5.95	75	1273	0.06
Si	17.0	59.1	1073	0.28

5 Temperature at which data presented in Metals Reference Book, Butterworths, 1976.

APPENDIX D

Charpy Curves

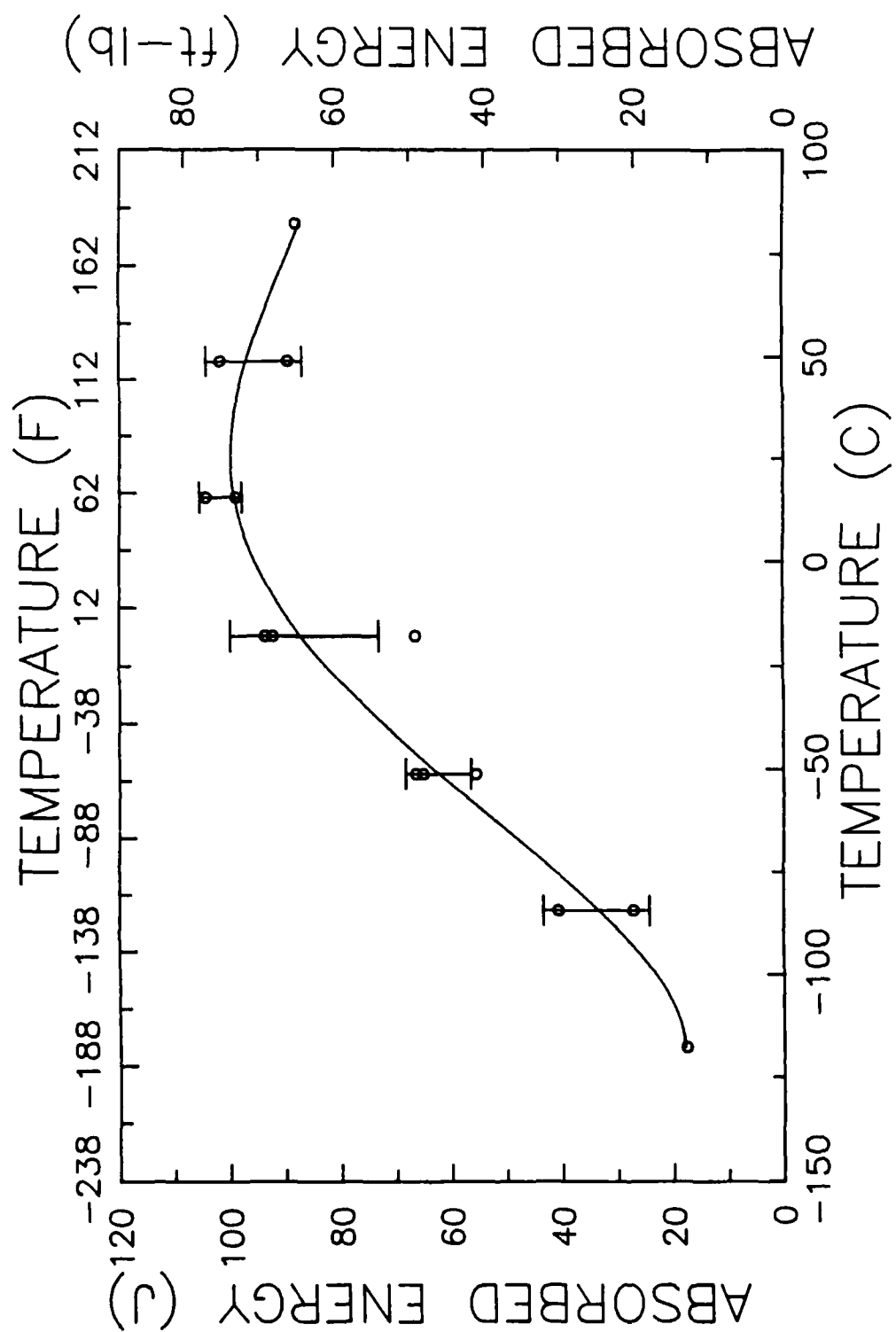


Figure 58. Temperature versus Charpy energy for weld A.

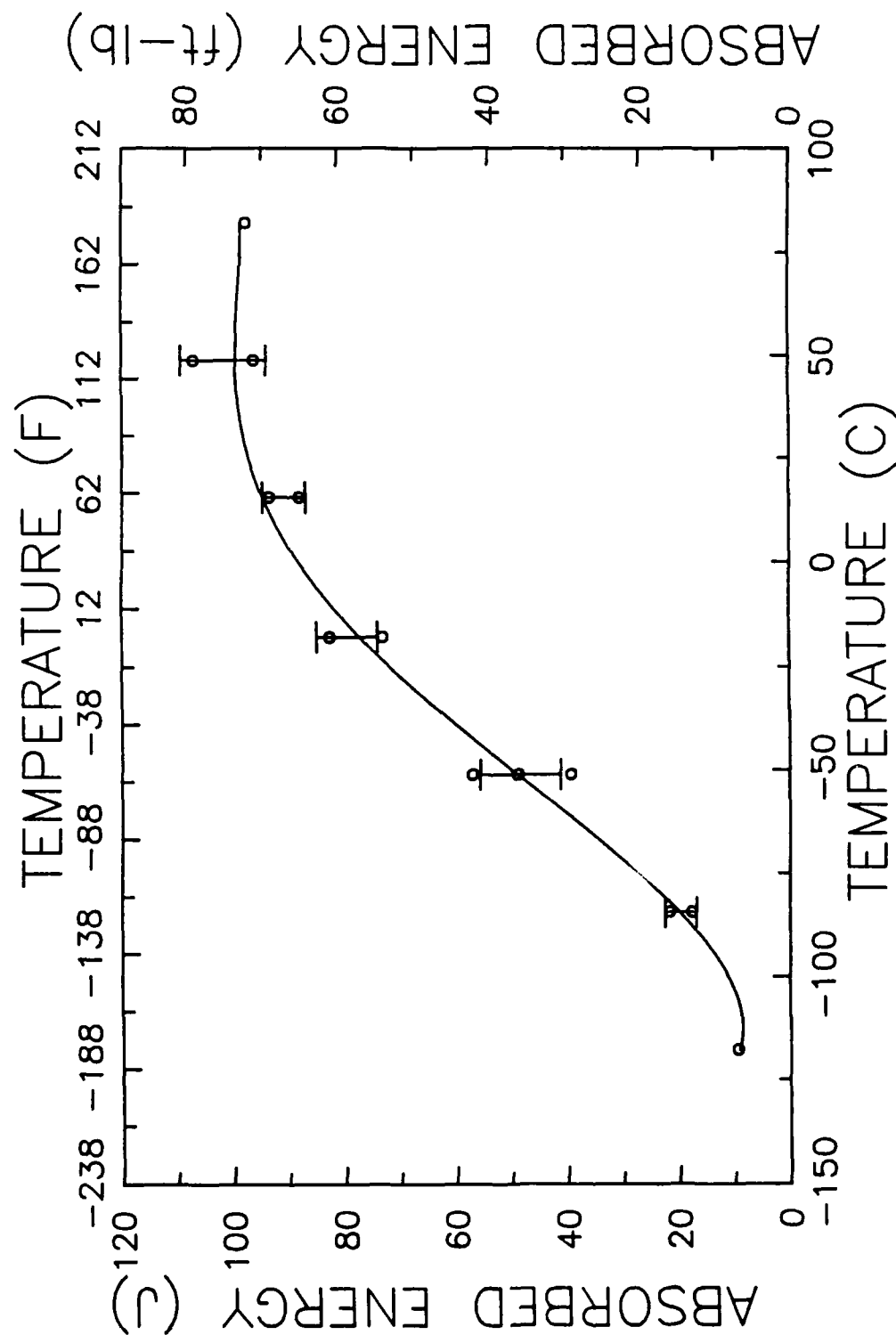


Figure 59. Temperature versus Charpy energy for weld B.

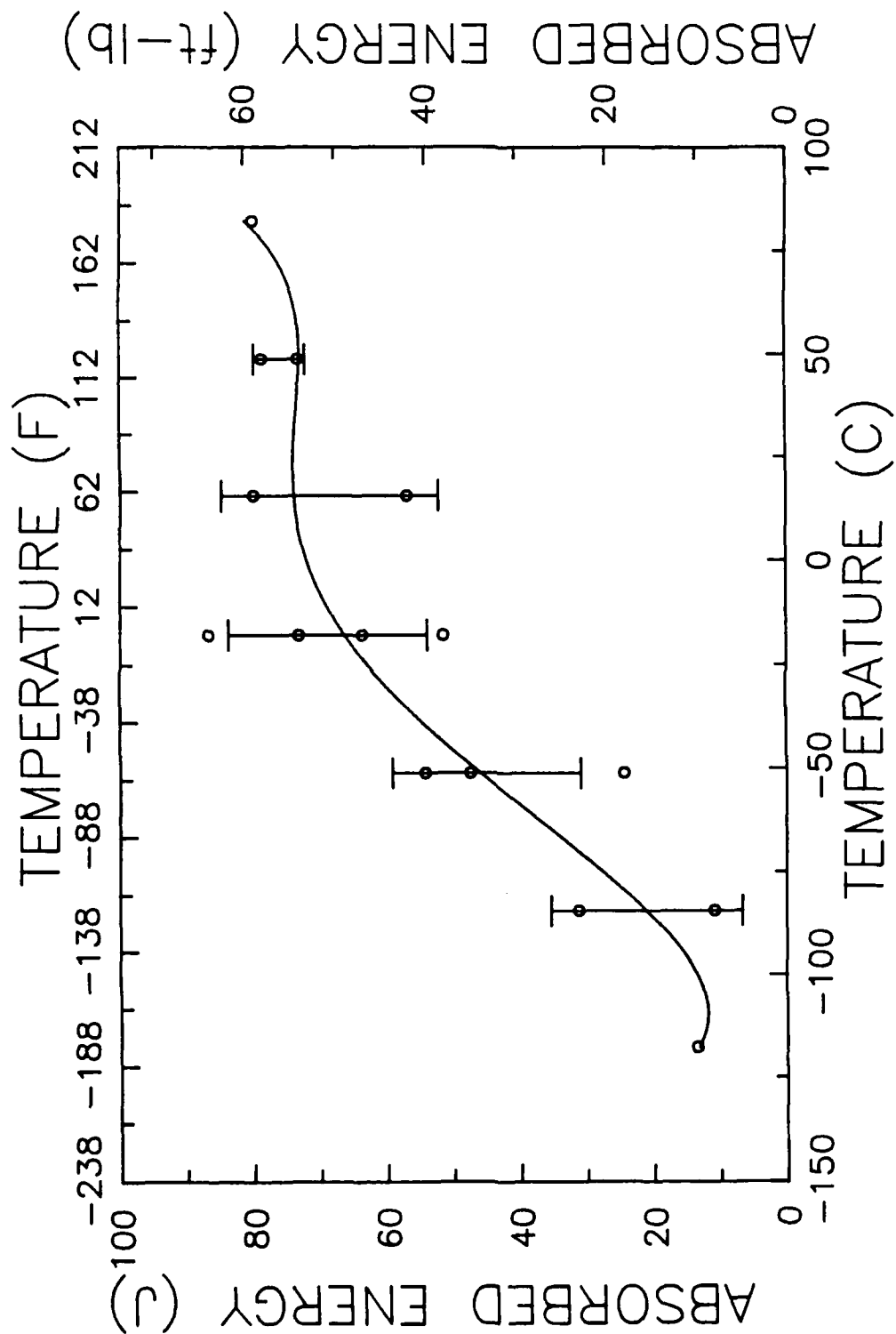


Figure 60. Temperature versus Charpy energy for weld C.

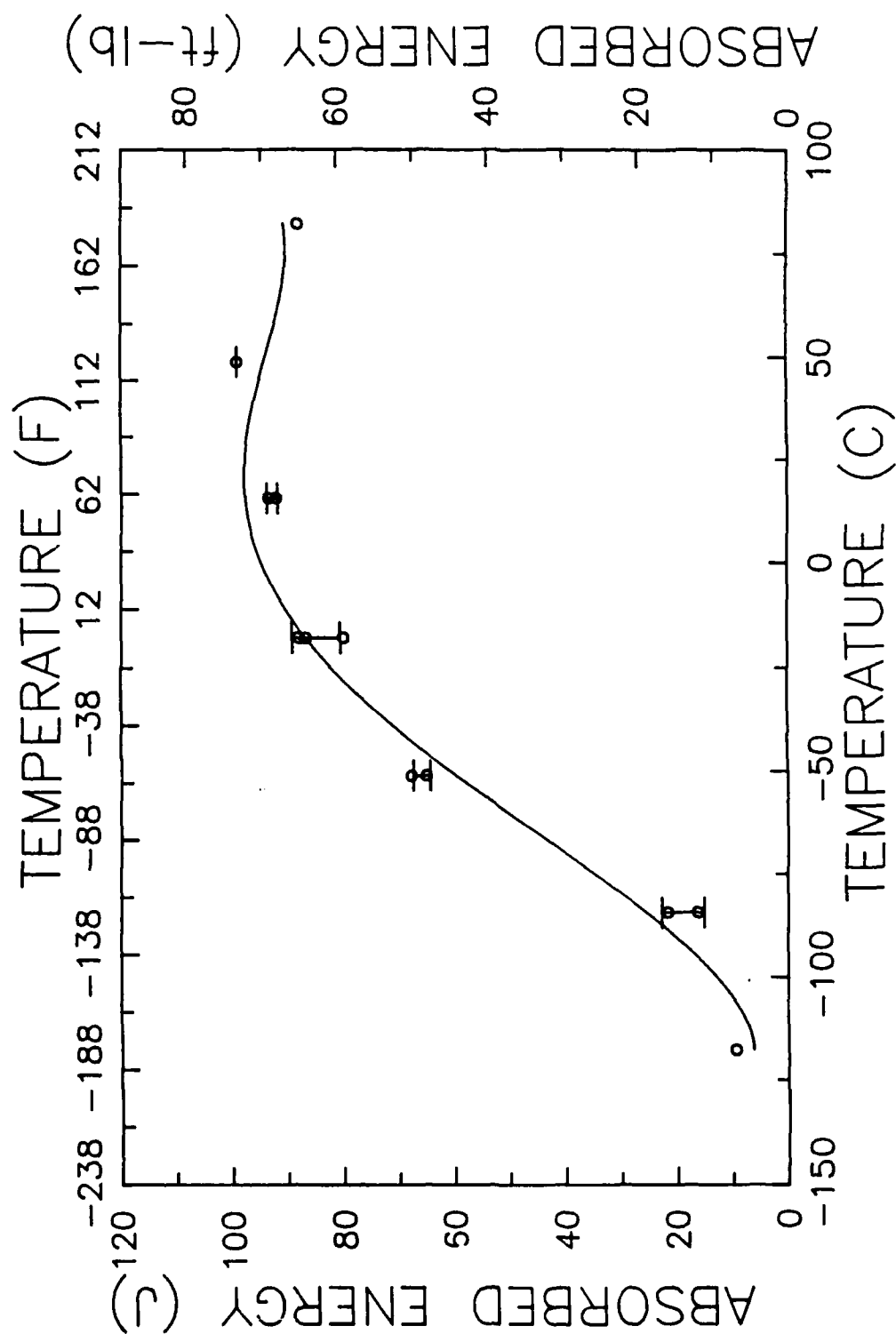


Figure 61. Temperature versus Charpy energy for weld D.

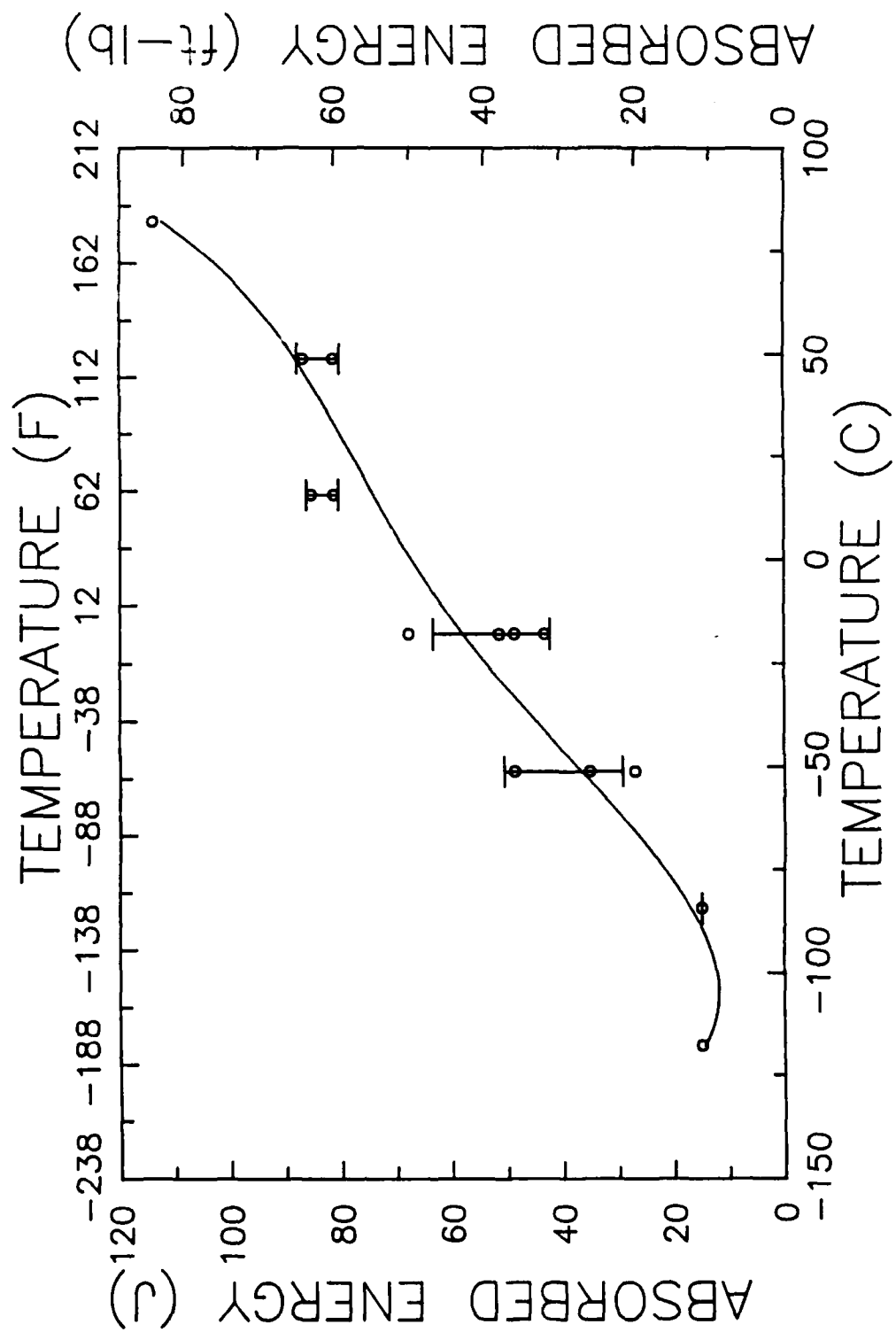


Figure 62. Temperature versus Charpy energy for weld E.

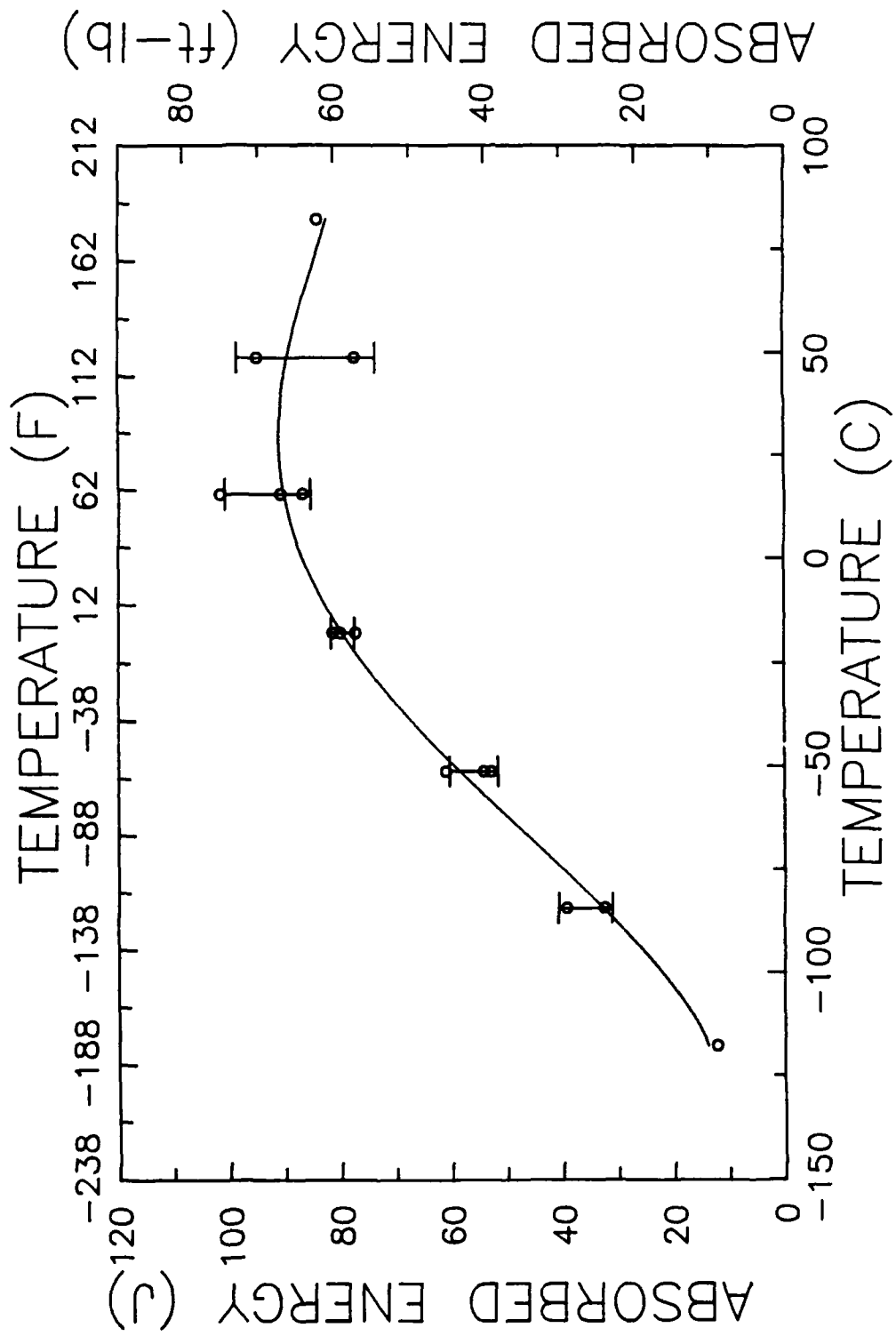


Figure 63. Temperature versus Charpy energy for weld F.

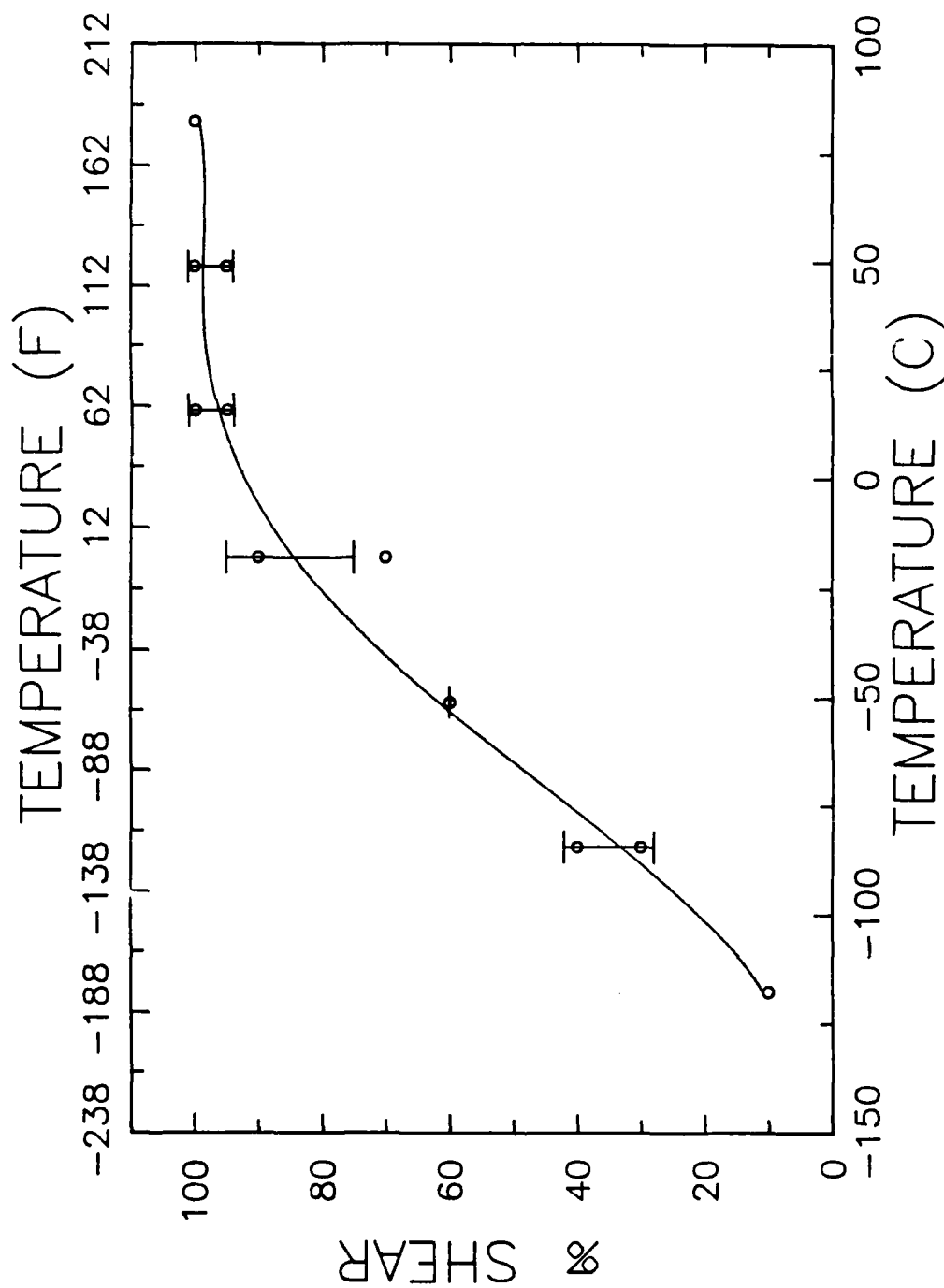


Figure 64. Temperature versus Charpy %shear for weld A.

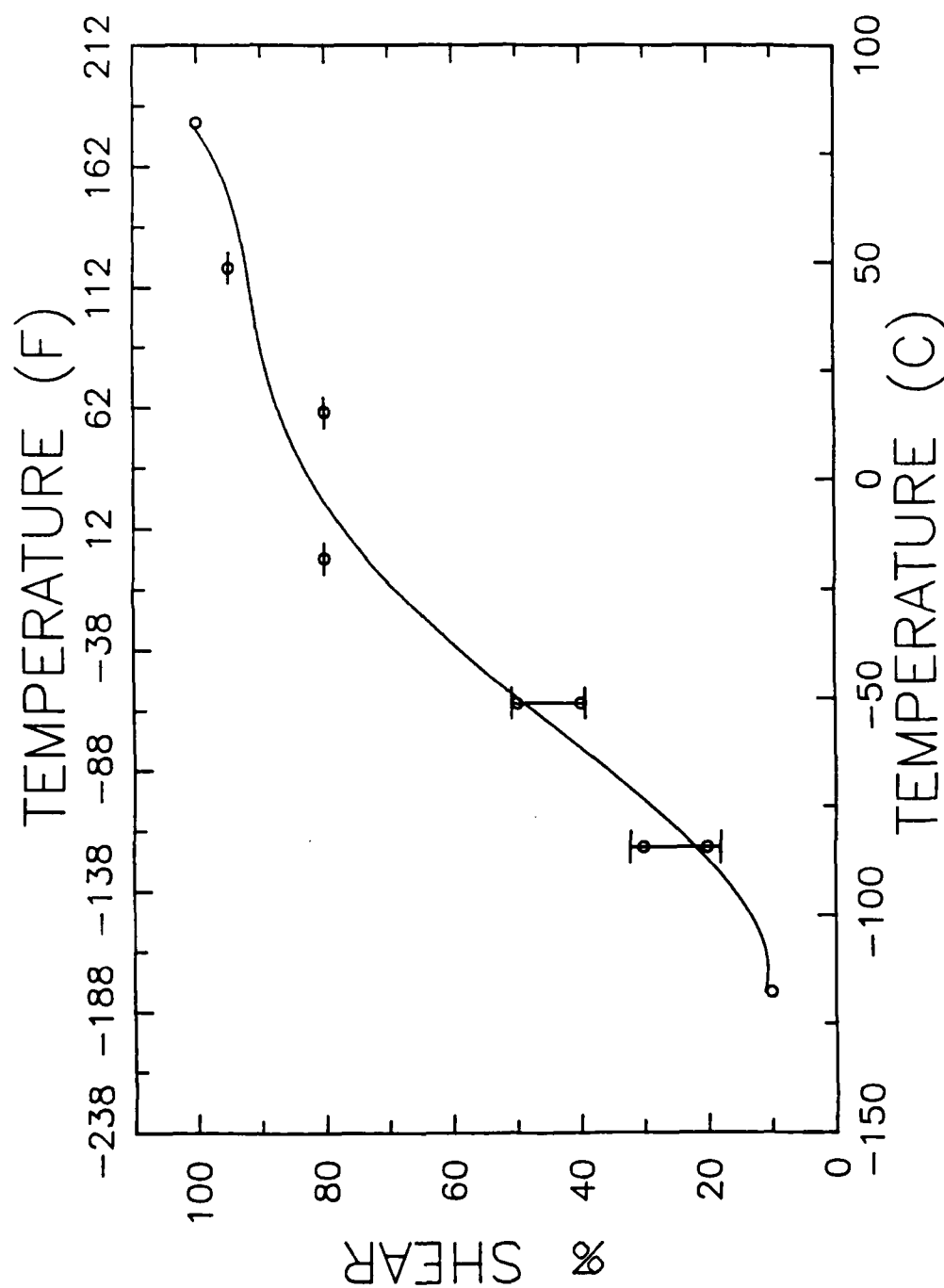


Figure 65. Temperature versus Charpy %shear for weld B.

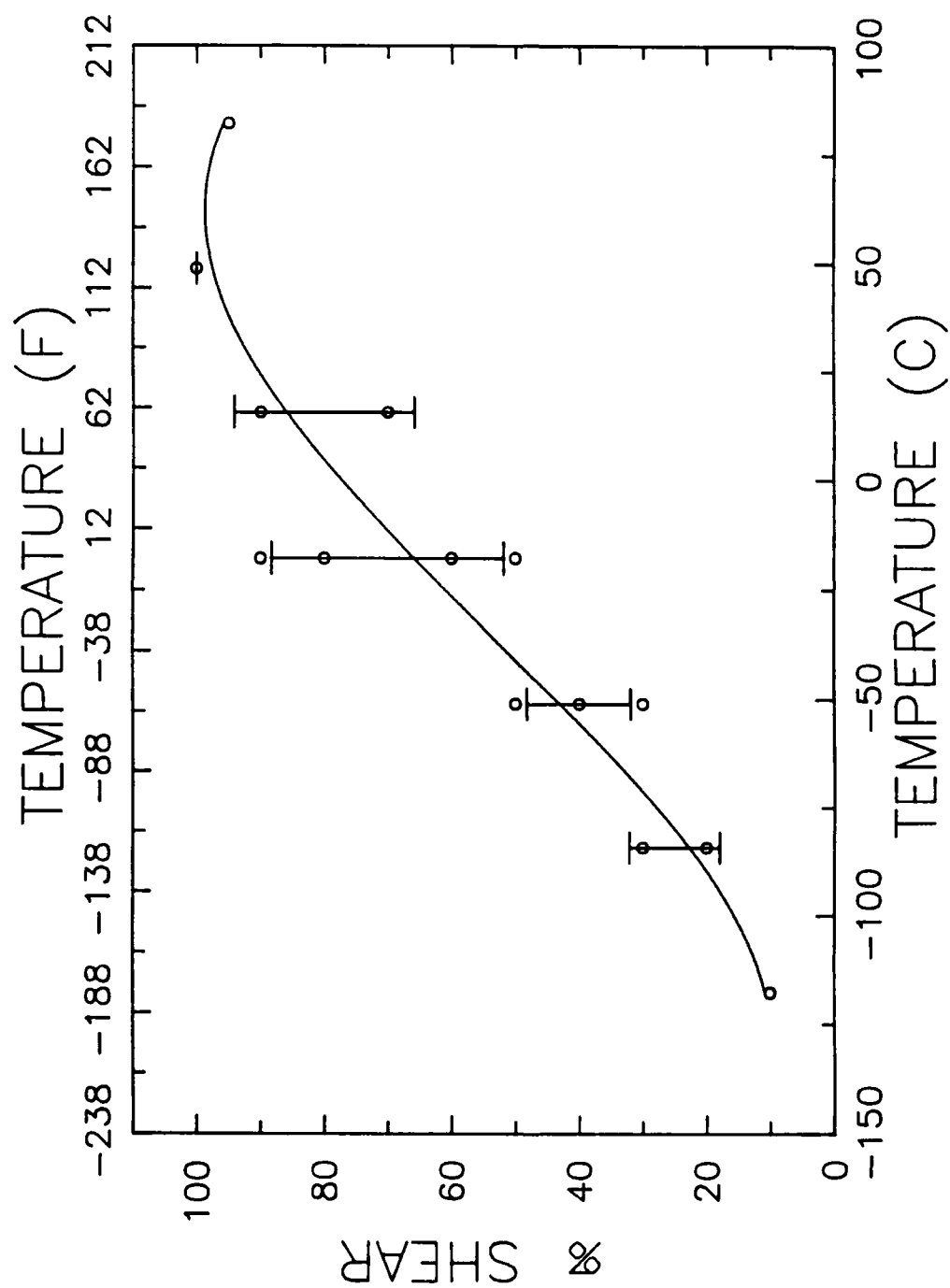


Figure 66. Temperature versus Charpy %shear for weld C.

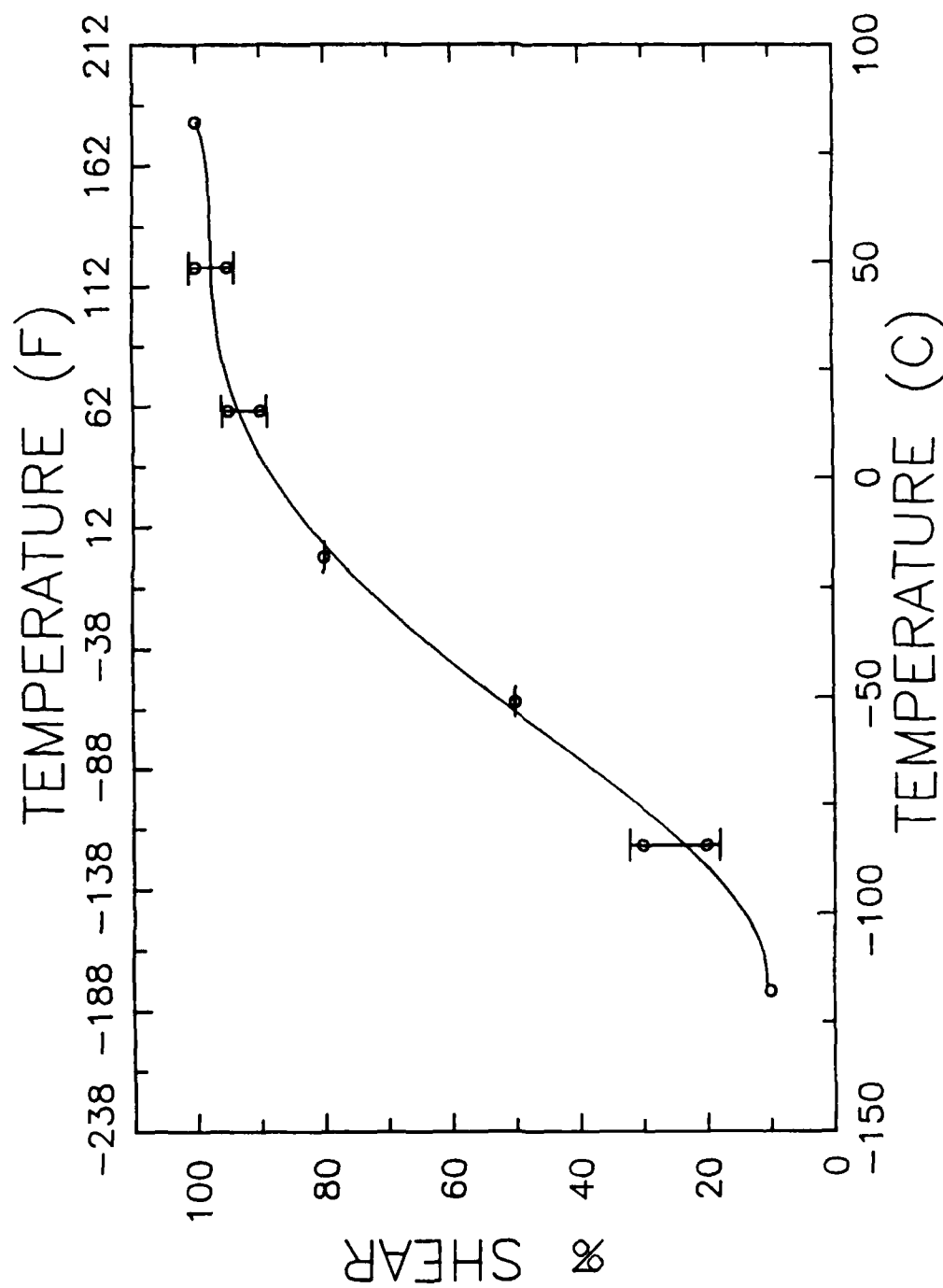


Figure 67. Temperature versus Charpy %shear for weld D.

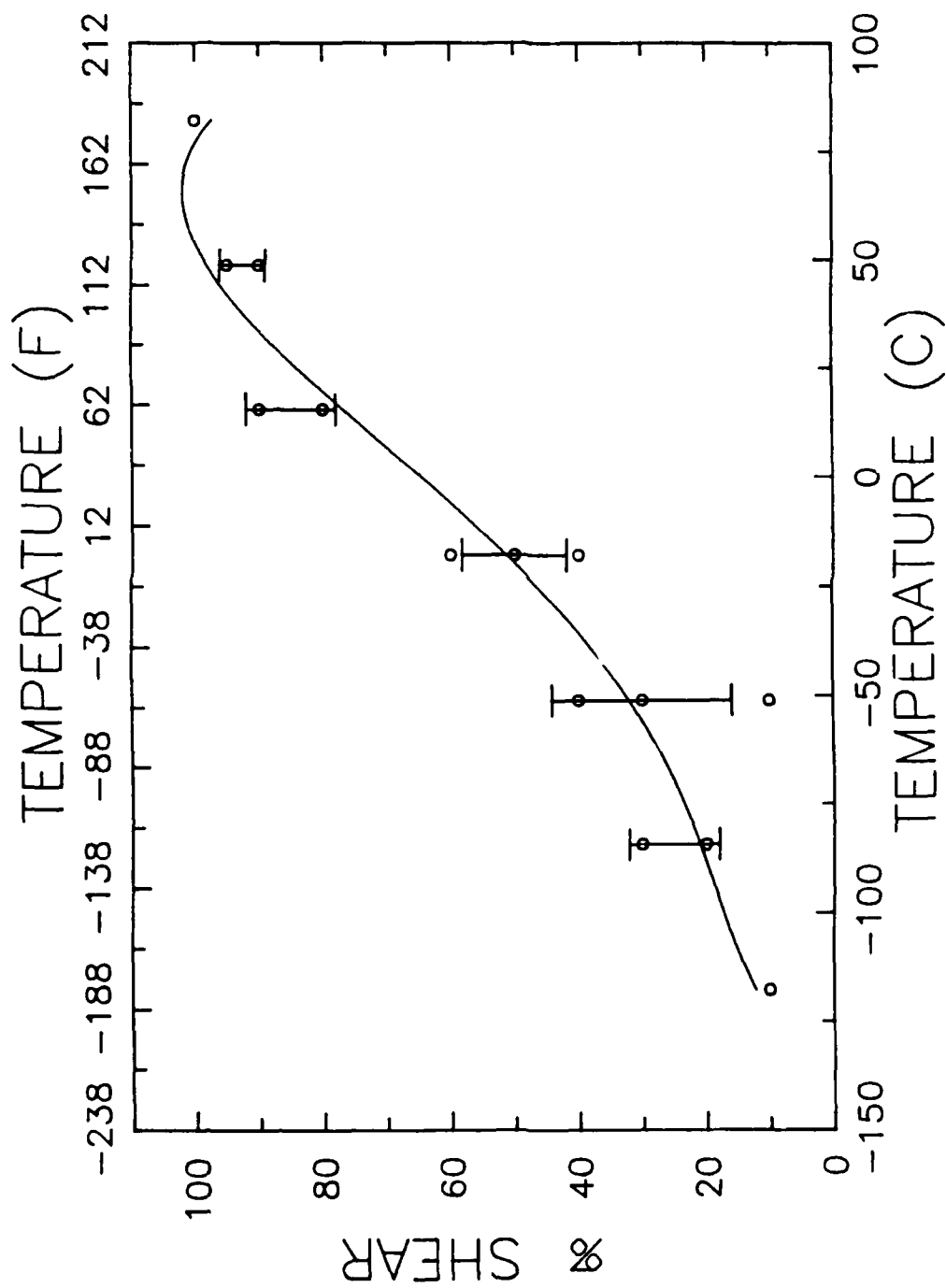


Figure 68. Temperature versus Charpy %shear for weld E.

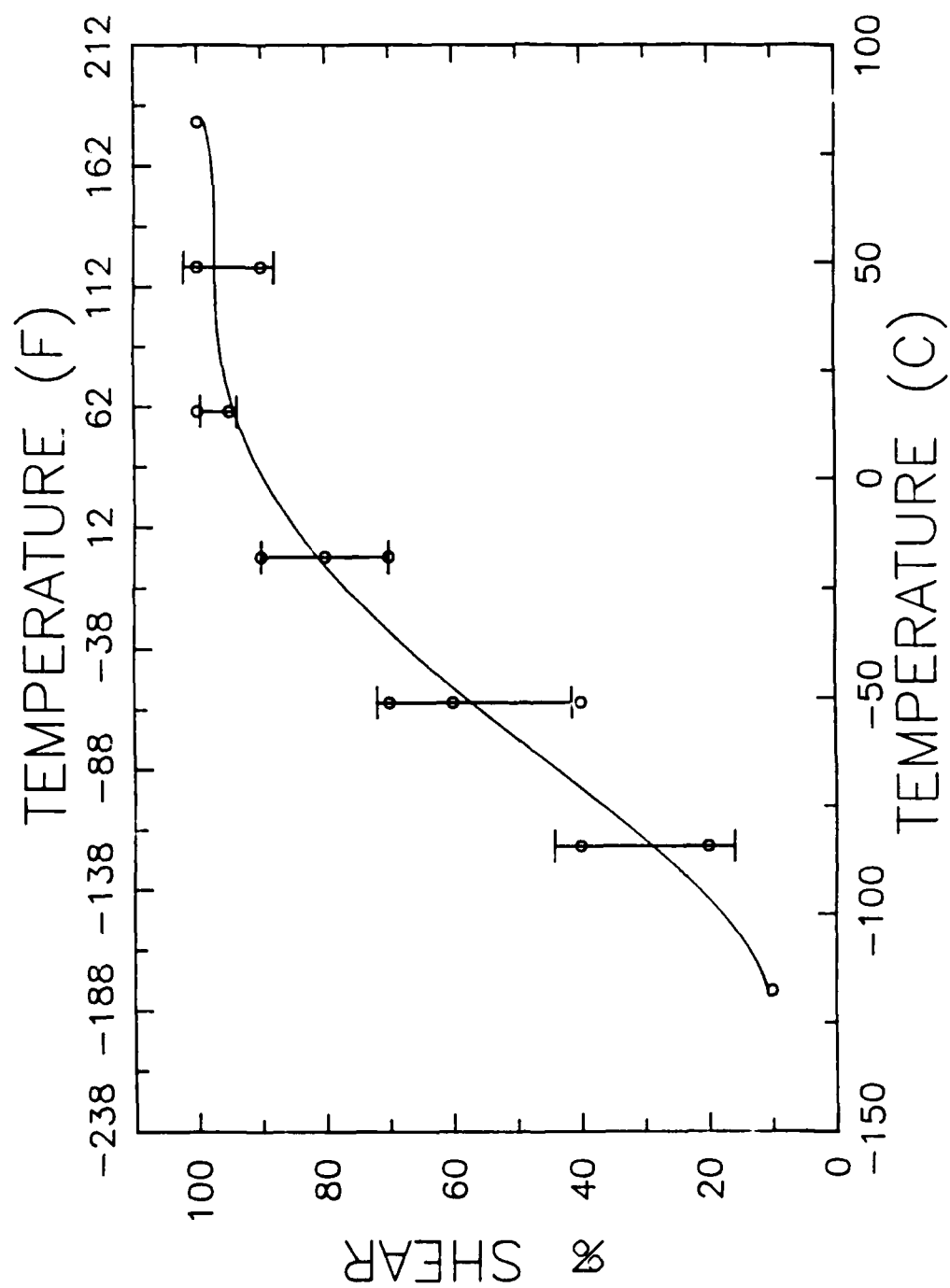


Figure 69. Temperature versus Charpy %shear for weld F.